33rd NOAA Climate Diagnostics and Prediction Workshop
Special Issue

Climate Prediction S&T Digest

https://doi.org/10.25923/vbn9-0514

December 2008

NWS Science & Technology Infusion Climate Bulletin Supplement

Inside this issue:

NOAA's National Weather Service

Office of Science and Technology
1325 East West Highway
Silver Spring, MD 20910

Climate Prediction Center
5830 University Research Court
College Park, MD 20740

Article Citation:

Author(s), 2008: Article title. Extended Summary, *Climate Prediction S&T Digest*, *33rd NOAA Climate Diagnostics and Prediction Workshop,* Lincoln, NE, DOC/NOAA, page range. DOI: 10.25923/vbn9-0514

Although the skill of current operational climate prediction is limited and the research on the topic presents many challenges, there are promises of improvement on the horizon. To accelerate advancement in climate services, an effective mechanism of S&T infusion from research to operation for application is much needed. This bulletin has been established to clarify science-related problems and relevant issues identified in operation, inviting our partners in the research community to work together on improvement of national climate prediction services.

Science and Technology Infusion Climate Bulletin
https://www.nws.noaa.gov/ost/STIClimateBulletin/index.htm

National Weather Service
National Oceanic and Atmospheric Administration
U.S. Department of Commerce

CONTENTS

1. DIAGNOSTICS

Science and Technology Infusion Climate Bulletin
NOAA's National Weather Service
33rd NOAA Annual Climate Diagnostics and Prediction Workshop
Lincoln, NE, 20-24 October 2008

An Overview of the 2007- 08 La Niña and Boreal Wintertime Variability

Michelle L'Heureux
Climate Prediction Center, NOAA/NWS/NCEP

1. The 2007-08 La Niña: A Strong Episode

The NOAA operational definition for La Niña is met when the Oceanic Niño Index (ONI) value is less than or equal to -0.5ºC. The ONI is based on the three month running-mean sea surface temperature (SST) departures from average in the Niño-3.4 region of the equatorial Pacific Ocean (5°N-5°S, 170°W-120°W). According to the ONI, the 2007-08 La Niña episode began in July-August-September 2007 and ended during April-May-June 2008. While the La Niña episode did not begin until the late summer, below-average SSTs were evident in the eastern equatorial Pacific as early as March 2007. The below-average SSTs slowly extended westward across the equatorial Pacific Ocean throughout 2007 (Figure 1).

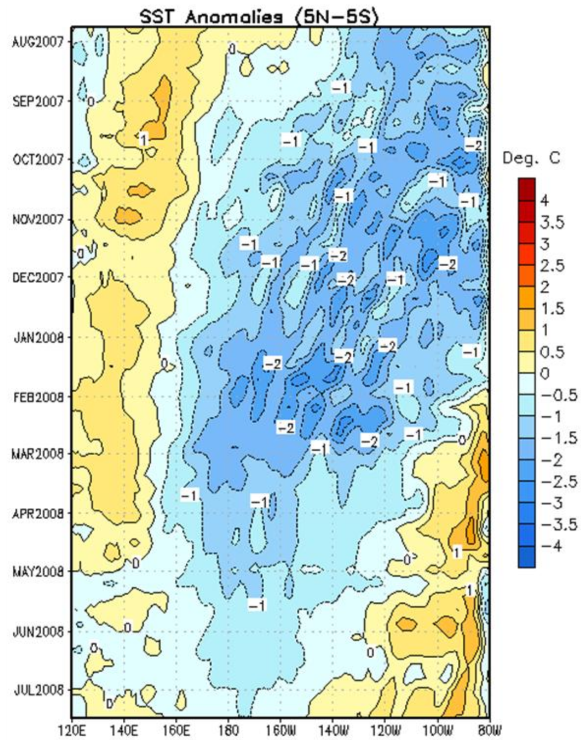

Fig. 1 Time-longitude sea surface temperature anomalies averaged from 5°N to 5°S. Anomalies are computed with respect to the 1971-2000 base period weekly means.

During the boreal winter of 2007-08, the coldest weekly SSTs in the Niño-3.4 region were reached during late January (Figure 2b), with the ONI reaching its minimum value of -1.5ºC during the three-month period of December-January-February (Figure 2a). Since December 1949, the minimum ONI value observed during this episode was only exceeded six times (1949/50, 1955/56, 1973/74, 1975/76, 1988/89, 1999/2000). Thus, the strong 2007-08 La Niña episode was roughly a 1 in 10-year event. By early February 2008, above-average SSTs had emerged in the eastern equatorial Pacific Ocean and gradually expanded westward bringing an end to La Niña conditions during June 2008 (Figure 1).

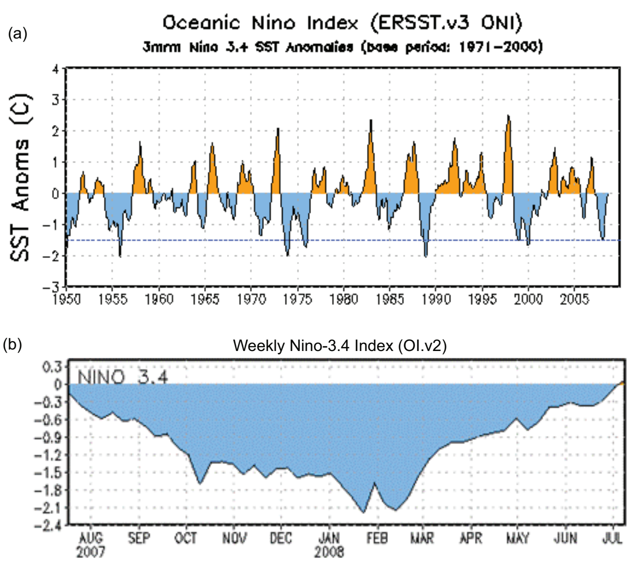

Fig. 2 (a) Time series of the Oceanic Niño Index (ONI) based on the three-month running-mean sea surface temperature departures in the Niño-3.4 region (5°N-5°S, 170°W-120°W) (b) Time series of sea surface temperature departures in the Niño-3.4 region. Anomalies are computed with respect to the 1971-2000 base period weekly means.

The seasonal mean anomalies for SSTs and precipitation during October-November-December (OND) and January-February-March (JFM) were fairly typical for a strong La Nina episode. Figure 3

Correspondence to: Michelle L'Heureux, Climate Prediction Center, NOAA/NWS/NCEP
E-mail: Michelle.L'Heureux@noaa.gov

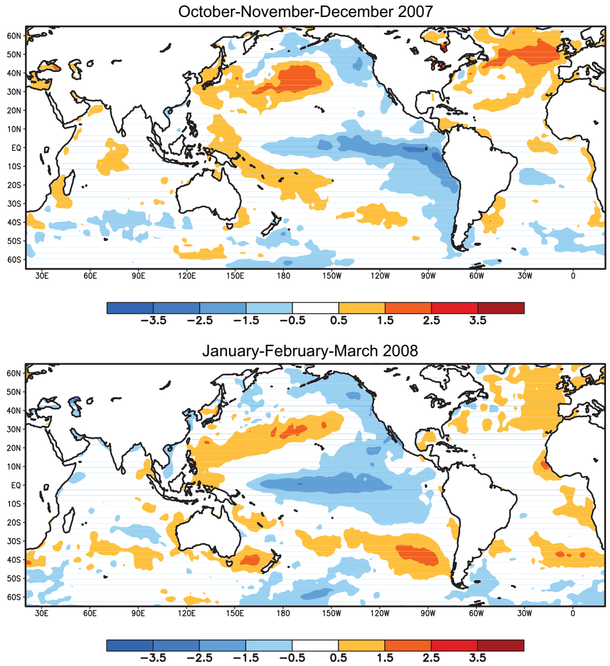

Fig. 3 (top panel) Sea surface temperature anomalies averaged for the October-November-December 2007 period (bottom panel) same as top except for the January-February-March 2008 period.

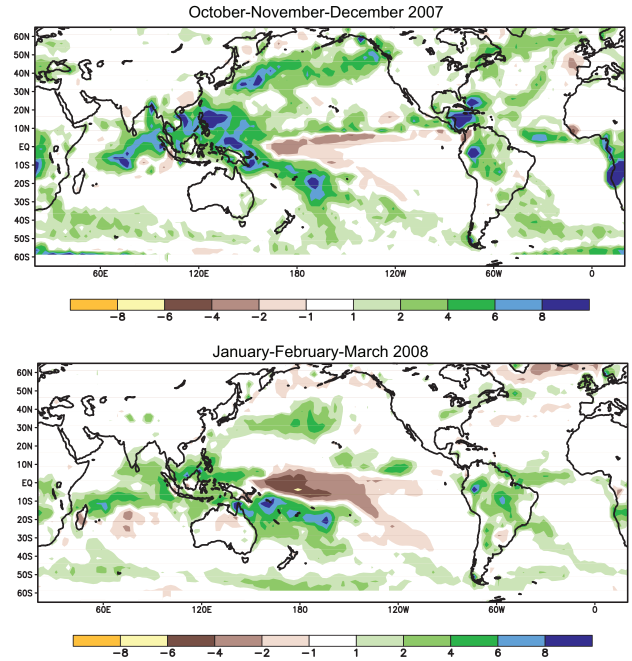

Fig. 4 (top panel) Precipitation anomalies averaged for the October-November-December 2007 period (bottom panel) same as top except for the January-February-March 2008 period.

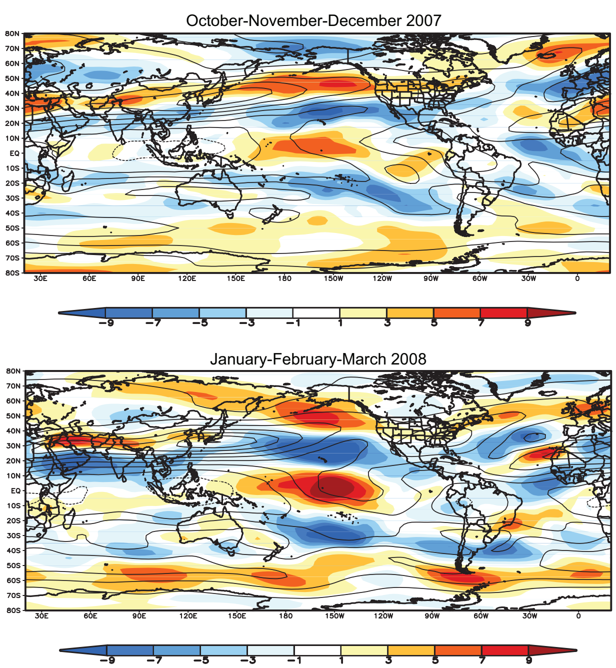

Fig. 5 (top panel) 200-hPa zonal wind (contours) and anomalies (shading) averaged for the October-November-December 2007 period (bottom panel) same as top except for the January-February-March 2008 period.

indicates below-average SSTs were evident across much of the equatorial Pacific Ocean, with above-average SSTs in the far western Pacific extending into the mid-latitudes of the North and South Pacific Oceans in a classical "horseshoe" configuration. The JFM below-average SSTs along the coast of western North America projected strongly onto the Pacific Decadal Oscillation (PDO) pattern, although it remains controversial as to whether this was a reflection of decadal variability or reflected variability on interannual timescales. Precipitation anomalies also featured a canonical La Niña pattern, which is associated with a westward retraction of deep tropical convection towards Indonesia, and suppressed precipitation focused on the Date Line in the central Pacific (Figure 4).

La Niña conditions also result in a westward retraction of deep tropospheric heating, and hence a westward retraction of the 200-hPa subtropical ridge toward Indonesia. The strength, structure, and position of the East Asian jet stream are strongly linked to conditions in the tropics and subtropics. During OND 2007 and JFM 2008, the core of the East Asian jet stream was retracted westward (Figure 5). The jet exit region coincides with the area of strong diffluence between the subtropical ridge and trough axes, resulting in anomalous ridging downstream of the jet exit. Figure 6 shows a prominent 500-hPa positive height anomaly in the central/eastern North Pacific Ocean indicating the westward shift of the meanridge from western North America. The mean Hudson Bay trough is also typically shifted westward during La Niña, although during JFM 2008, the southward extent of the anomalous trough was quite pronounced and covered much of the central and western United States (Figure 6).

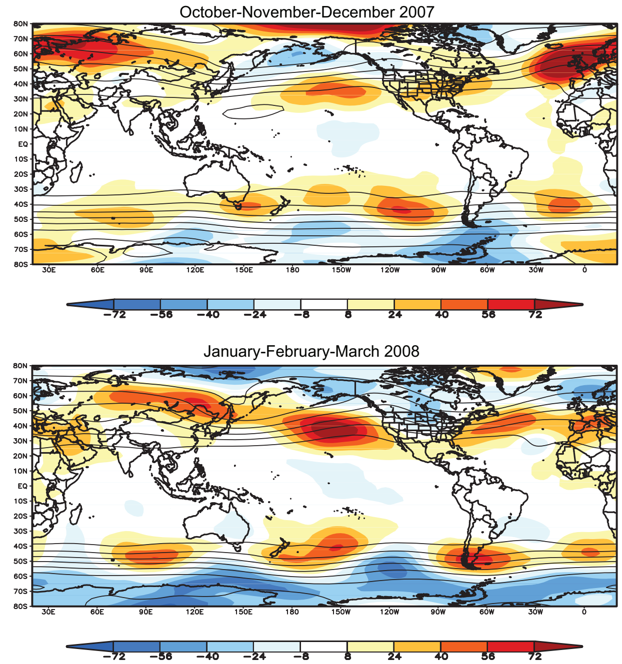

Fig. 6 (top panel) 500-hPa geopotential heights (contours) and anomalies (shading) averaged for the October-November-December 2007 period (bottom panel) same as top except for the January-February-March 2008 period.

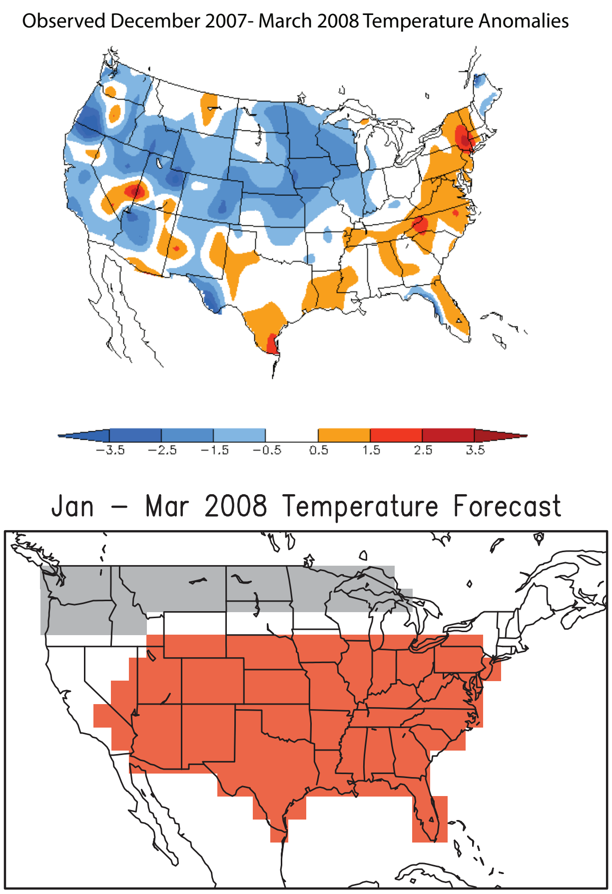

Fig. 7 (a) Average surface temperature departures for December 2007-March 2008. Calculated from daily gridded NCDC co-op station data. (b) 0.5-lead CPC forecast for temperature during January-March 2008. Red grid boxes represent an above-average forecast (upper-tercile), gray grid boxes reflect a near-average forecast (middle-tercile), and white boxes indicate an "Equal Chances" forecast.

During December 2007- March 2008, the anomalous trough helped to facilitate the influx of below-average temperatures into the upper Midwest and across the western United States (Figure 7- top panel). Average- to above-average temperatures were prevalent across most of the eastern United States. The observed temperature anomalies contrasted sharply with the CPC seasonal forecast, which were based on a combination of historical La Niña impacts and regional temperature trends. In the 0.5-month lead forecast for JFM, forecasters had predicted above-average temperatures over most of the United States with near-average temperatures expected over the northern tier of states (Figure 7- bottom panel).

The CPC forecast for precipitation was quite skillful compared to the seasonal temperature forecast. December 2007-March 2008 brought the expected La Niña-like increase in precipitation to the Pacific Northwest, northern Rockies, and Ohio and Tennessee Valleys, and also the precipitation decreases across much of the southern tier (Figure 8). However, CPC did not forecast the southward expansion of above-average precipitation across the central and southern Rockies extending into the desert Southwest, or the surplus precipitation that fell across New England.

2. Variability within the Boreal Winter Season

While the boreal winter mean was consistent with La Niña, the extent of variability within the season was dramatic. During the winter months, the East Asian jet stream affects the downstream flow over the North Pacific and United States. To further understand how the variability in the jet affected the December 2007- March 2008 season, a zonal wind index was created averaging the zonal wind in the area of the greatest variance in the 200-hPa zonal wind (gray shading in Figure 9a). The daily wind index was then standardized based on the mean and standard deviation of the December 2007-March 2008 period (Figure 9b). The zonal wind index was used to subdivide all 122 days within the December 2007- March 2008 period into three different regimes. A "retracted jet" regime is the composite of all days less than -0.6σ (33 days), while the "extended jet" regime is the composite of all days greater than 0.6σ (32 days). The third regime represents an average of the "remaining days" in the period between the 0.6σ thresholds (57 days).

Figure 10 shows composites for these three regimes of the full 200-hPa zonal wind field and the anomalous 500-hPa geopotential height. The "remaining days" regime features a jet core that is

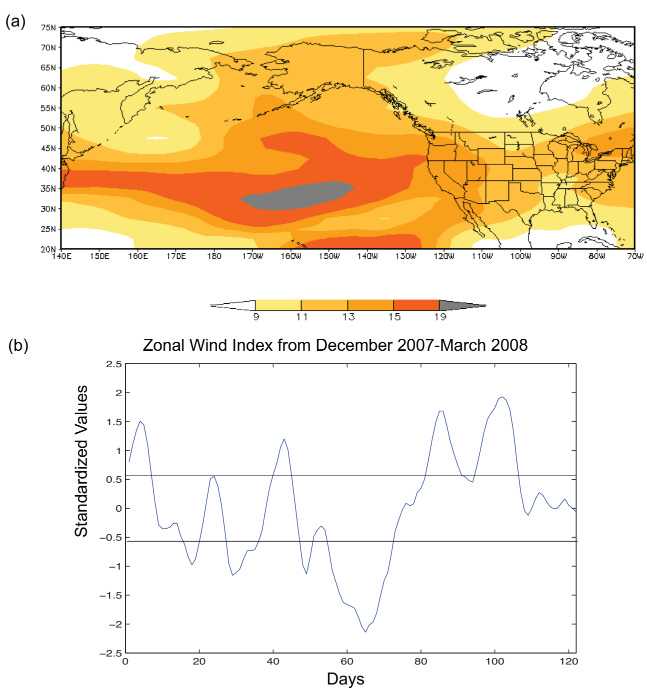

Fig. 9 (a) Variance in daily 200-hPa zonal wind during December 2007- March 2008. (b) Standardized "zonal wind index" based on the area-averaged 200-hPa zonal wind in the region shaded by grey in (a). Horizontal lines denote 0.6σ thresholds for "extended jet" days, "retracted jet" days, and the "remaining days" regimes.

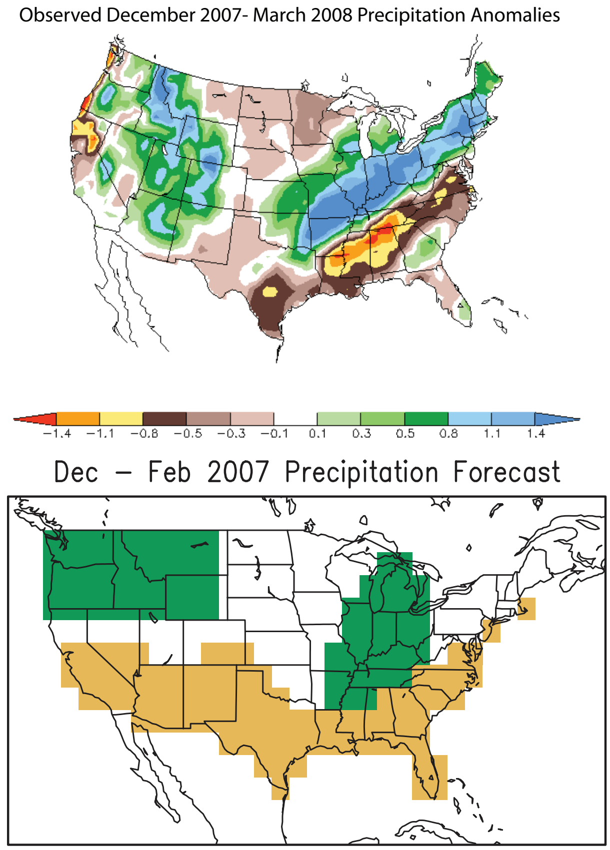

Fig. 8 (a) Average surface precipitation departures for December 2007-March 2008. Calculated from daily gridded Unified station data. (b) 0.5-lead CPC forecast for precipitation during December-February 2008. Green grid boxes represent an above-average forecast (upper-tercile), tan grid boxes reflect a below-average forecast (lower-tercile), and white boxes indicate an "Equal Chances" forecast.

west of the Date Line with the jet remaining amplified into the northwestern United States. Downstream of the jet core and east of the Date Line, an anomalous ridge is evident in the eastern Pacific Ocean, with a weak anomalous trough centered over the north-west United States, and an anomalous ridge over the eastern United States. This regime is consistent with a La Niña-like pattern.

The "retracted jet" regime shows a strong East Asian jet with its core shifted west of the Date Line in the North Pacific Ocean. Near the jet exit region, a very pronounced anomalous 500-hPa ridge is observed and a strong anomalous trough downstream of the ridge impacts much of the central and western United States. This regime includes a retracted jet and an anomalous North Pacific ridge that is consistent with La Niña, but the flow is anomalously amplified as evidenced by the deep, southward extension of the trough over the United States.

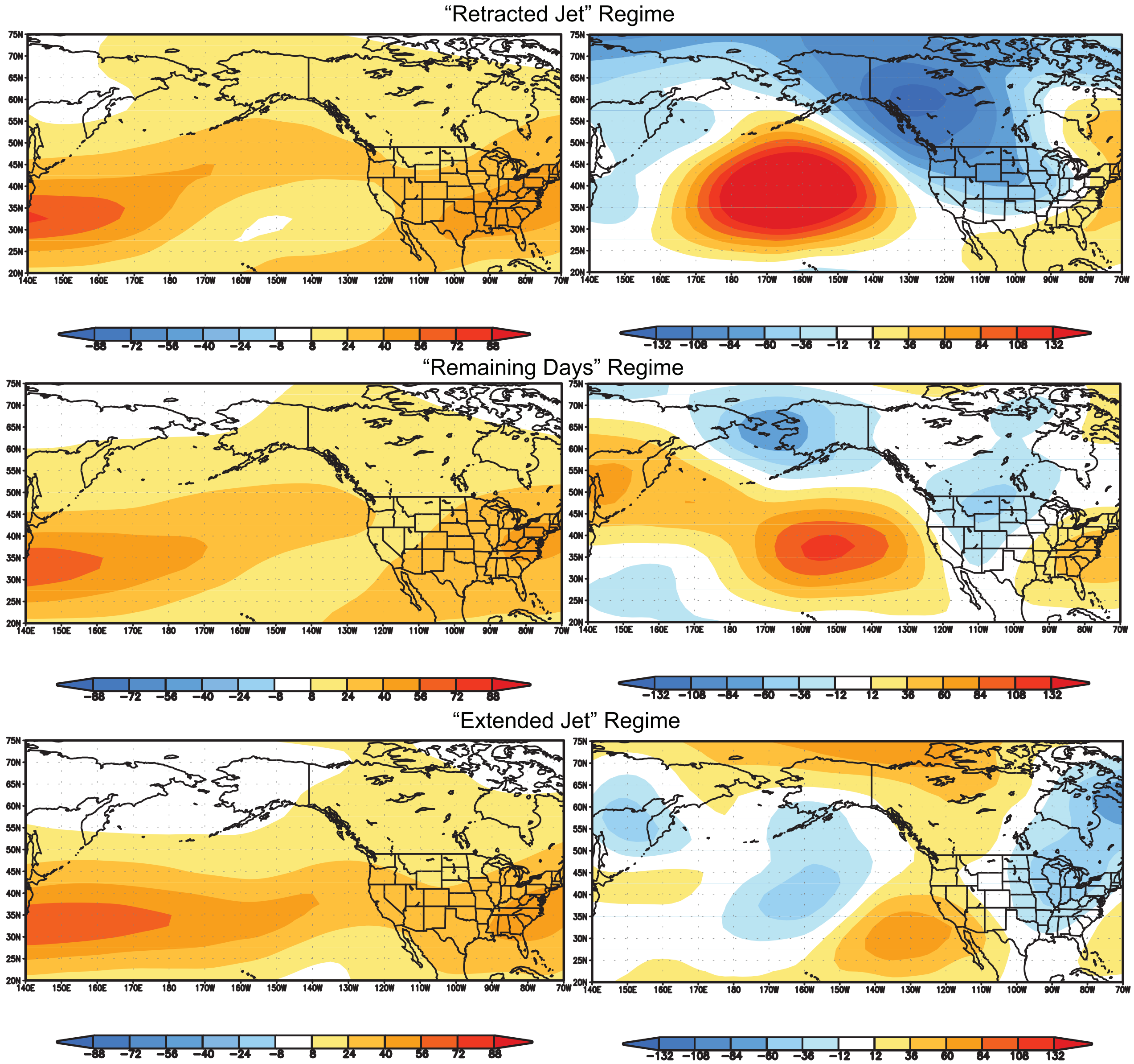

Fig. 10 200-hPa zonal wind composite (left panels) and 500-hPa geopotential height anomaly composite (right panels) based on the three regimes identified with the zonal wind index during December 2007- March 2008.

The "extended jet" regime reveals a very different pattern relative to other two regimes, with the East Asian jet core extending east of the Date Line with nearly zonal flow continuing into the southern United States. Instead of a dominant anomalous ridge, a weak anomalous trough is evident east of the Date Line with an anomalous ridge centered just off the southern West Coast of the United States. Over eastern North America, an anomalous trough is centered near the Hudson Bay extending south over much of the central and eastern United States. Aspects of the circulation are reminiscent of El Niño, such as the extended jet into the southern United States and an anomalous trough in the North Pacific Ocean.

These dramatic differences between the two regimes led to varying temperature and precipitation anomalies over the United States (Figure 11). The seasonal mean (Figures 7 and 8- top panels) was subtracted from each composite in order to isolate the distinct influence that each regime had on changes in

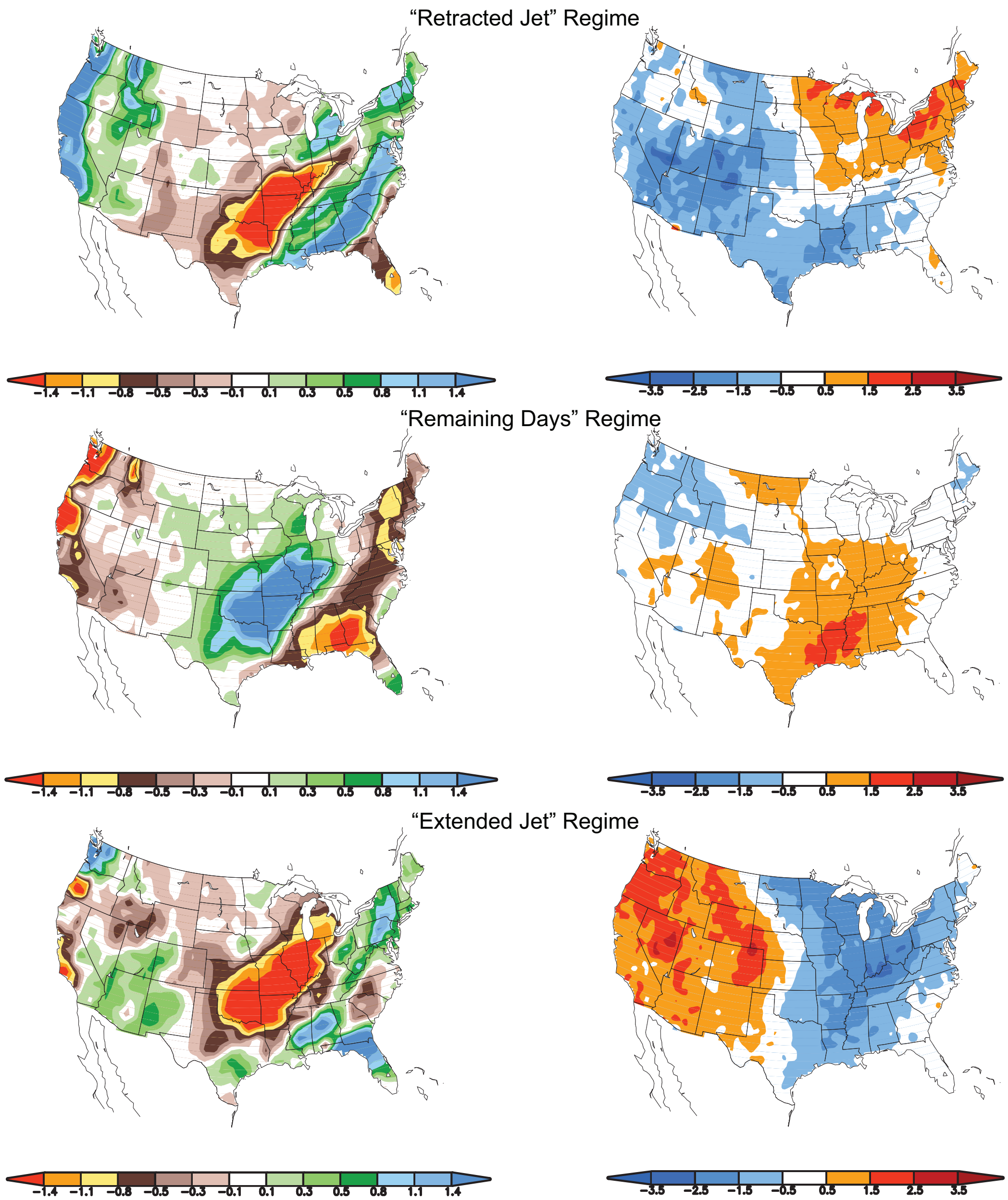

Fig. 11 For the three regimes, the temperature anomaly composites (right panels) and precipitation anomaly composites (left panels) with the December 2007- March 2008 mean removed.

temperature and precipitation relative to the December 2007- March 2008 period. During the "retracted jet" regime, the far-reaching anomalous trough helped to decrease temperatures over the southern and western United States. Also apparent was an increase in precipitation over much of the far western United States in association with the enhanced transport of moist maritime air linked to the anomalous trough. The pronounced trough also contributed to a southeastern shift in the storm track into the southeastern United States.

In contrast, during the "extended jet" regime, the cooling shifted to the eastern United States, associated with an eastward shift in the anomalous trough. An extended jet helped to enhance rainfall over much of the southern tier of states, particularly over the Southwest and along the Gulf Coast and Florida. Over the Ohio and Tennessee valleys, precipitation decreased with a precipitation pattern that is more reminiscent of El Niño than La Niña.

The "remaining days" regime led to a change in the temperature anomalies that reflects La Niña, with increases in temperature over the southeast and temperature decreases over the Pacific Northwest. Similarly, an increase in precipitation was observed over the Ohio and Tennessee Valleys with below-average precipitation observed over many of the southern tier states (excluding Texas). However, relative to the other two regimes, this regime led to a relative decrease of precipitation over the Pacific Northwest, which is not consistent with La Niña.

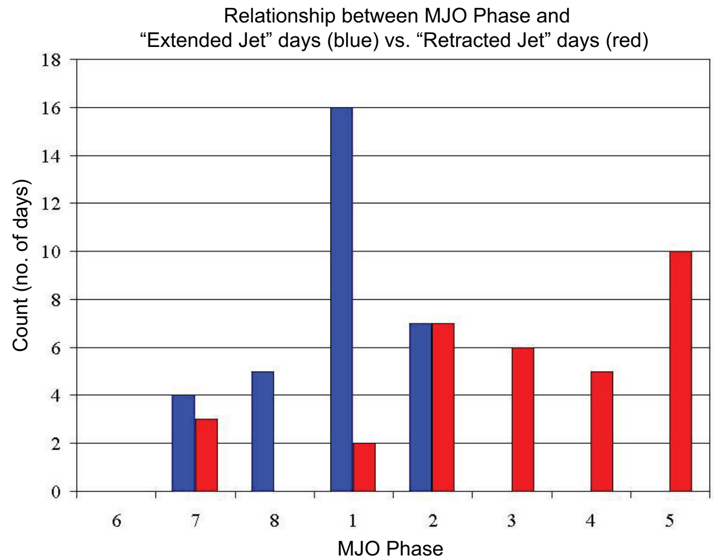

Fig. 12 "Extended jet" days (blue) versus "retracted jet" days (red) binned according to the Wheeler and Hendon MJO index phase (Phases 1-8) during December 2007-March 2008.

Although not yet established, the contrasting regimes (extracted vs. extended jet) may have contributed to the relatively low skill score of the seasonal temperature forecast. These two regimes accounted for about half of the days within the December 2007- March 2008 period. During both regimes, the flow pattern that developed resulted in below-average temperatures across much of the United States. If the winter had been more consistently like the "remaining days" pattern, a more La Niña-like temperature pattern may have resulted.

3. Potential Influence of the Madden-Julian Oscillation

In addition to the strong La Niña during the boreal winter of 2007-08, there was also a very active Madden-Julian Oscillation (MJO), one of the leading patterns of subseasonal variability in the equatorial global tropics. These eastward propagating disturbances strongly modulate tropical and subtropical patterns of atmospheric circulation and precipitation as they move around the globe with a period of ~30-60 days. In the Eastern Hemisphere, a distinctive convective signal slowly shifts eastward over the warm waters of the Indian and western Pacific Oceans. As the MJO progresses over the cooler waters of the Western Hemisphere, the deep convection dissipates, but coherent and faster eastward propagation remains. Strong-to-moderate MJO activity was observed almost continuously from mid-November 2007 through February 2008, making three cycles around the equator before fading. So, to what extent was the variability within the boreal winter 2007-08 also related to an active MJO?

Figure 12 shows the eight phases of the MJO (based on Wheeler and Hendon's real-time MJO index) as it relates to the two opposing jet regimes (extended vs. retracted) observed during December 2007- March 2008. MJO phases 6/7/8/1 represent the location of MJO-related convection over the tropics of the Western Pacific and Western Hemisphere. MJO phases 2/3/4/5 denote MJO-related convection over the Indian Ocean and the Maritime Continent. In order to examine potential relationships between the MJO and wintertime variability, the days in the retracted and extended jet regimes are binned according to the phase of the MJO index. Remarkably, there is a high degree of clustering based on the phase of the MJO. Nearly all extended jet days (32 days) cluster in Phases 6/7/8/1, indicating that the extended jet regime occurred when MJO-related convection was over the Western Hemisphere. Conversely, days associated with the retracted jet regime (33 days) were associated with MJO-related convection over the Eastern Hemisphere (Phases 2/3/4/5). Thus, half of the days in the December 2007- March 2008 period involved a circulation pattern that was linked to the phase of the MJO.

Therefore, the variable circulation observed during the boreal winter of 2007-08 was likely associated with the combined influence of the MJO and strong La Niña conditions. These climate patterns helped to collectively modify the East Asian jet (three regimes), and therefore set up circulation patterns that resulted in widely varying impacts on temperature and precipitation over the United States.

References

Matthew C. Wheeler and Harry H. Hendon, 2004: An All-Season Real-Time Multivariate MJO Index: Development of an Index for Monitoring and Prediction. *Mon. Wea. Rev.*, **132**, 1917-1932.

Science and Technology Infusion Climate Bulletin
NOAA's National Weather Service
33rd NOAA Annual Climate Diagnostics and Prediction Workshop
Lincoln, NE, 20-24 October 2008

The Impact of Mean Climate on ENSO: Simulation and Prediction

Xiaohua Pan[1] and Bohua Huang[1, 2]

[1]*Department of Atmospheric, Oceanic and Earth Sciences, College of Science, George Mason University, Fairfax, VA*

[2]*Center for Ocean-Land-Atmosphere Studies, Calverton, MD*

1. Introduction

The El Niño/Southern Oscillation (ENSO) variability simulated by fully coupled global ocean-atmosphere general circulation models (CGCMs) has been assessed in numerous multimodel intercomparison projects (e.g., Neelin *et al.* 1992; Mechoso, 1995; Latif *et al.*, 2001; AchutaRao and Sperber, 2002; Davey *et al.*, 2002). More recently, several studies (Joseph *et al.* 2006; Leloup *et al.* 2008) also examined CGCMs' ENSO simulations under the forcing of the 20th century greenhouse gas. In both cases, it is found that some major ENSO characteristics are not well captured by most of these models. Temporally, the simulated ENSO cycle is more regular than the observed one and anomalous events occur too frequently in the models. Spatially, the sea surface temperature (SST) anomalies in the tropical Pacific extend too far westward and are too narrowly confined to the equatorial zone.

The potential causes of these model deficiencies in the simulation of ENSO could be the coarse model resolution and inadequate parameterizations of the sub-scale physical processes. Both factors not only can affect the simulated ENSO characters directly, they also cause deficiencies in the model mean climate and indirectly affect the model ENSO. ENSO is now well understood as an oscillation superimposed on a mean climate over the tropical Pacific (Bjerknes 1969). The mean climate can be defined as the long-term averaged climatology of the system. Figure 1 shows the observed mean climate of SST and surface wind stress in the tropical Pacific. The mean SST features an east-west asymmetry near the equator, with cold water in the eastern and warm water in the western Pacific associated with easterly trade winds. A north-south asymmetry is also present in the eastern Pacific where warm water is located north of equator and cold water is present along the coast of Peru with cross-equatorial southerly trade winds straddling in between. The existence of these asymmetries is crucial for the formation of both the annual cycle (*e.g.*, Xie 1994) and ENSO (Cane and Zebiak 1987). However, the simulated mean climate has substantially weakened the asymmetric mean structure. For instance, cold SST bias in the central equatorial Pacific substantially reduces the temperature of the warm pool, while the warm bias near the coast of Peru weakens the meridional SST gradient. As a result, the mean SST field becomes more conducive for the occurrence of a robust "double ITCZ". These deficiencies in the

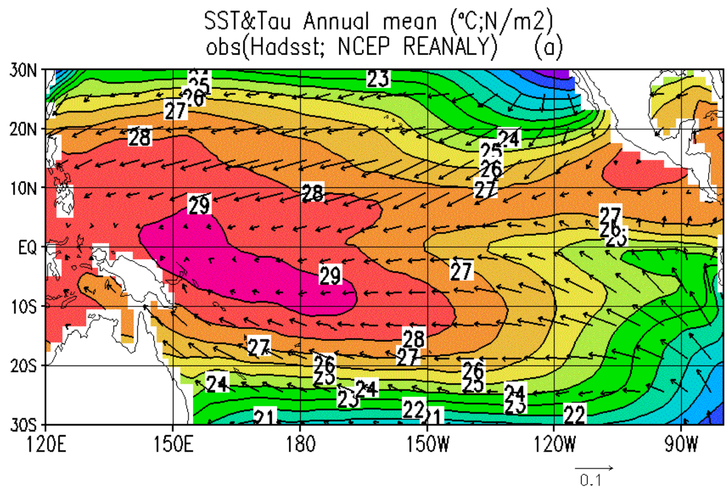

Fig. 1. The spatial distributions of the annual mean SSTs (°C) and wind stress vector (N/m^2) over the tropical Pacific for observation. The SST data is from Hadley center monthly mean SST for1900-1999; the wind stress vector is from NCEP reanalysis for1948-2003. The shading is SSTs, and the vector is wind stress with the magnitude of 0.1 N/m^2.

Correspondence to: Xiaohua Pan, Department of Atmospheric, Oceanic and Earth Sciences, College of Science, George Mason University, Fairfax, VA; E-mail: xpan@cola.iges.org

simulated mean climate are likely responsible for some of the unrealistic ENSO properties in the coupled model (Li and Hogen 1999; Manganello and Huang 2008).

This study examines the impact of mean climate on the simulation, predictability and prediction of ENSO. Moreover, we demonstrate that the mean state also can strongly influences the annual cycle in the eastern equatorial Pacific. To achieve a more realistic model mean SST field, we have applied a heat flux correction to a state-of-the-art coupled model, the Community Climate System Model version 3 (CCSM3). It has been widely used in tropical climate research and demonstrated to suffer from both the mean state bias and errors in ENSO simulation (e.g., Deser *et al.*, 2006) as we have described above. CCSM3 is considered as a member of the national multi-model ensemble for operational climate forecast. However, besides the work done by Kirtman and Min (2008), little is known about its ENSO prediction skill. This study provides more information on it.

2. Models

Community Climate System Model (CCSM) has been developed at NCAR and made available to the scientific community. Its third version (CCSM3) is released in June 2004 (Collins *et al.* 2006). It is comprised of four components: atmosphere, ocean, land and sea ice, which are coupled together through a flux coupler. This version also includes new updates of all component models. The atmosphere is Community Atmosphere Model Version 3 (CAM3), the land surface model is Land Surface Model version 3.0 (CLM3), the sea ice model is Sea Ice version 5.0 (CSIM5) and the ocean model is Parallel Ocean Program version 1.4.3 (POP). In this study, we use T85 resolution at CAM3, corresponding to a spatial resolution of 1.4°. It has 26 vertical levels. The spacing of the POP grids is 1.125° in the zonal direction and roughly 0.5° in the meridional direction with higher resolution near the equator. The vertical dimension is treated using a depth (z) coordinate with 40 levels extending to 5.37 km.

Air-sea coupling is accomplished through the periodic, conservative passing air-sea flux between the ocean and atmosphere components. At the end of each ocean coupling interval, the ocean sends its time averaged, upper level (10m) temperature and velocity to a flux coupler, which takes these to be SST and surface current. Following every radiation calculation, the atmosphere sends the net surface solar and long-wave radiation along with its averaged lowest level winds, potential temperature, humidity, density, and height. The standard CCSM3 is with a 1-day coupling interval for the ocean model, while using 1-hour coupling for the other components of the coupled system.

3. Experiment design

3.1. *Heat flux correction scheme*

The primary goal of the present research is to study the impact of the mean climate on the simulation, predictability and prediction of ENSO variability rather than to correct the model bias. For this purpose, a sensitivity simulation is performed in which a simplified empirical scheme is applied by adjusting the surface heat flux into the ocean and the model results are compared with a control simulation. This method has been used in another coupled CGCM with satisfying results (Manganello and Huang 2008). Specifically, a time independent surface heat flux correction term (ΔQ) is added to the atmospheric surface heat flux before passing to the ocean. ΔQ is defined as,

$$\Delta Q = -\Delta SST \times R$$

where ΔSST is the100-year (1900-1999) mean state SST bias of the control run in comparison with observations. The adjustable coefficient R with unit W/m2K converts the SST error to heat flux. ΔQ is constant in time and kept identical for both the simulation and all forecast experiments described in Sections 3b and 3c. The surface heat flux correction is applied at the air-sea interface by adding ΔQ into the surface trace flux terms (i.e., net surface heat flux excluding net solar radiation) in the ocean component model at the daily coupling frequency. Given SST changes of 1K, the heat flux changes approximately 15 W/m^2 in a fully coupled model (Doney *et al.* 1998). Considering the sharp warm biases along the coast of Peru (even beyond 4°K in some places), a moderate R with value of 10W/m^2 per K is chosen in the tropical region between

30°S-30°N, where the interaction of air and sea is responsible for a strong relationship among anomalous SST, surface wind stress, convection and ocean heat content, and ENSO is a dominant phenomenon. This coefficient descends linearly to zero from 30°S to 40°S and 30°N to 40°N. The meaning of the heat flux correction is straightforward. It takes heat away from regions with the warm bias (*e.g.* off the coast of Peru) and put heat into regions with the cold bias (e.g., the central equatorial Pacific).

3.2. Heat flux corrected simulation

The control and heat flux corrected simulations are hereafter referred to as the *contrl* and *flx10* simulations, respectively. The *flx10* simulation is integrated for 55 years from an initial state of the atmosphere and ocean derived from the *contrl* simulation. The model is spun up for five years and only the last 50 years of its output are used in our analysis. Since both the flx10 and *contrl* simulations are forced by observed 20th century greenhouse gases and volcanic forcing, the model years are labeled as calendar years with respect to its real-time greenhouse gas level.

3.3. Heat flux corrected prediction

In order to assess the impact of the mean climate on ENSO prediction and predictability, two sets of seasonal hindcast experiments are performed with and without the heat flux correction using CCSM3, denoted as the *flx10* and *contrl* forecasts, respectively. Since the ENSO predictability is seasonally dependent, hindcasts are initialized on January 1st and July 1st in each year from 1982 to 1998. Each hindcast is integrated for 12 months. The initialization strategy follows that of Kirtman and Min (2008), using ocean initial conditions from analyses of the GFDL ocean data assimilation. The initial conditions for the atmosphere-land, and sea ice are derived from an AMIP-type run with prescribed real-time SST. For each oceanic initial condition, a 3-member ensemble hindcast is generated with perturbed conditions of the atmosphere, land and sea ice.

4. Results

4.1. Mean climate

The simulated annual mean SST is remarkably improved in the *flx10* experiment relative to the *contrl* (Figure 2b and d), due to the surface heat flux correction. The simulated equatorial cold bias is reduced by about 0.5°C, which extends less towards the western Pacific. Meanwhile, the warm bias off the coast of South America is less pronounced with amplitude reduced by about 0.5 °C. Away from the equator, the cold bias also becomes less pronounced in *flx10*.

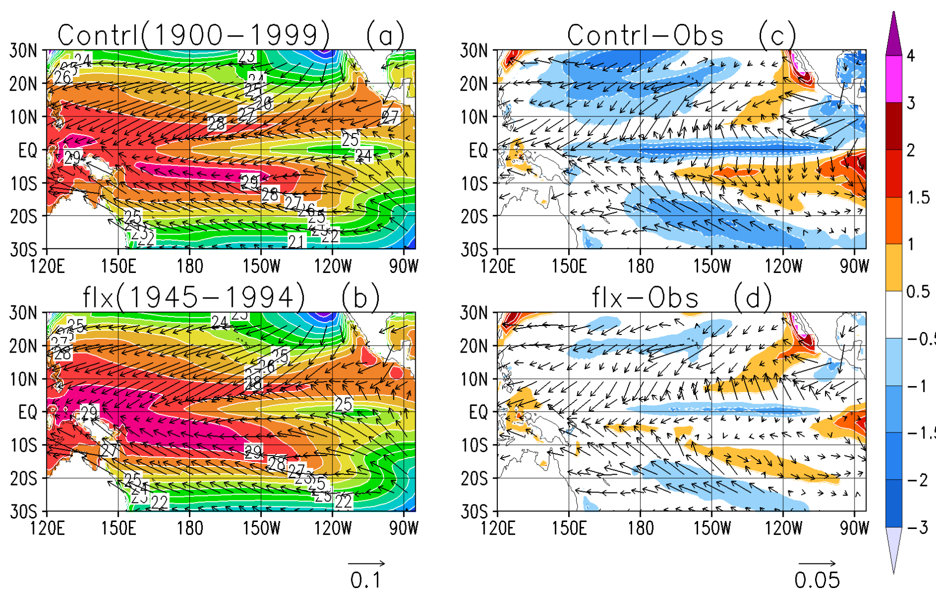

Fig. 2. *Left panel:* The spatial distributions of the annual mean SSTs (°C) and wind stress vector (N/m^2) over the tropical Pacific for *contrl* and *flx10***.** *Right panel:* biases in *contrl* and *flx10*. The observed SST data is from Hadley center monthly mean SST for 1900-1999; the observed wind stress vector is from NCEP reanalysis for1948-2003; *contrl* is for 1900-1999; and *flx10* is for 1945-1994. The shading is SSTs, and the vector is windstress with the magnitude of 0.1 N/m^2 in the left panel and 0.05 N/m^2 in the right panel.

The simulated annual mean wind stress is also improved in the *flx10* experiment relative to the *contrl* (Figure 2b and d), especially in the eastern Pacific where the SST warm bias occurs. The southerly off the coast of the South American in *flx10* is more similar to the observed both in amplitude and direction (Figure 2c). Even the cross-equatorial southerly wind, which is largely missing in *contrl*, is reproduced in *flx10*. It should be pointed out that the improvement in the surface wind stress is a dynamical response to the changes in the SST because no empirical adjustment is exerted upon the surface wind or wind stress.

4.2. Seasonal cycle

The seasonal cycle of equatorial SST from the observations and simulations is shown in Figure 3. The observed SST (left panel) exhibits a dominant annual cycle with the "cold tongue" weakest in March-April and peaking in August-October in the equatorial eastern Pacific. There is a pronounced westward propagation in the eastern and central equatorial Pacific. The *contrl* experiment (middle panel) produces an unrealistic strong semi-annual cycle in the eastern Pacific instead, with the "cold tongue" decaying in April-May (one month later than observed) and peaking in July-August (one month earlier than observed), as well as the unrealistic secondary cooling in February and warming in November-December. Additionally, there is no obvious tendency of westward propagation. In contrast, *flx10* (right panel) reproduces the observations reasonably well with a pronounced annual cycle and western propagation in the eastern Pacific. The artificial cold and warm centers in February and November-December in *contrl* is eliminated, although the coldest anomalies still appear too early, suggesting a too quick decay of the cold tongue. In *flx10*, the enhanced annual cycle is generated dynamically because the heat flux correction employed in the coupled model is time independent and does not contribute to the annual oscillation directly.

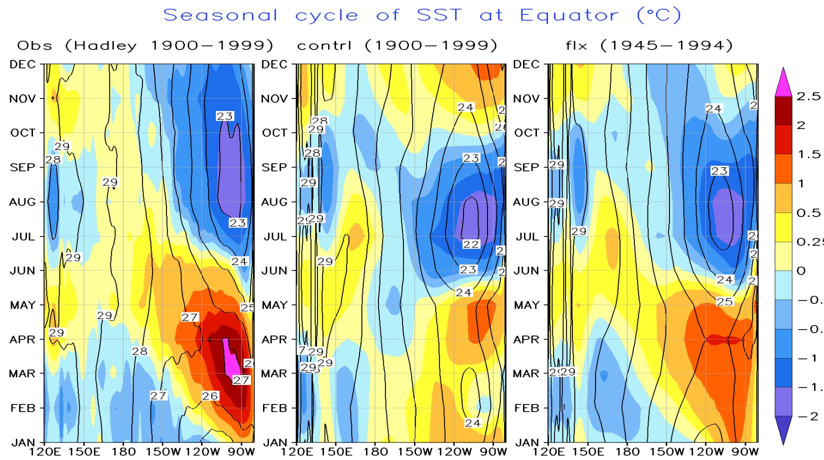

Fig. 3. The seasonal cycle along the equatorial Pacific region (5°S-5°N) for SSTs (°C). The shadings represent the seasonal anomalies relative to the annual mean, while the contours represent the total value. The vertical axis indicates the month-of-year, varying from the bottom to top.

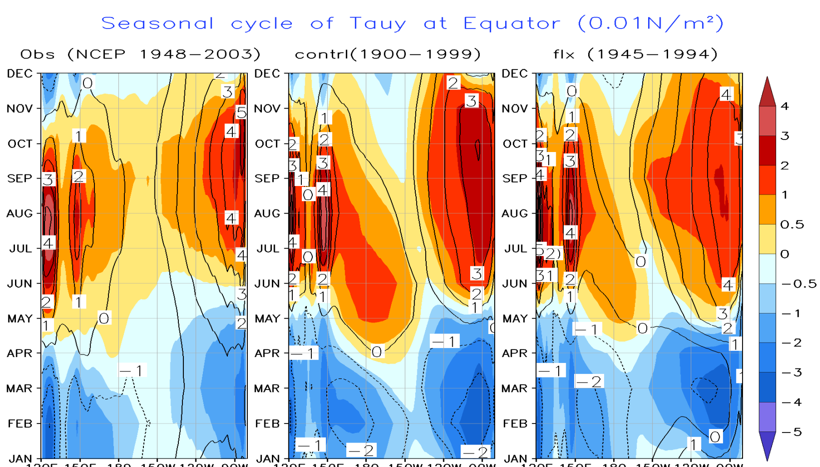

Fig. 4. The seasonal cycle along the equatorial Pacific region (5°S-5°N) for Meridional wind stress (0.01N/m^2). The shadings represent the seasonal anomalies relative to the annual mean, while the contours represent the total value. The vertical axis indicates the month-of-year, varying from the bottom to top.

The seasonal cycle of the equatorial meridional wind stress is shown in Figure 4. Unlike its strong semi-annual SST fluctuation, *contrl* produces a strong annual cycle in its meridional wind stress (middle panel). A major unrealistic feature is the quite strong northerly winds of 2 m/s persisting from January to March, which cools down the sea surface through excessive evaporation and causes the artificial cold center of SST in February (Middle panel, Figure 3). On the other hand, the *flx10* (right panel) reproduces a well persistent cross-equatorial southerly throughout a year in the equatorial eastern Pacific (indicated by contours) although weaker than observed. The seasonal variation of this southerly in *flx10* experiment is more similar to that in the observations (left panel) with weak southerly in the spring season, compared to the northerly in the *contrl* experiment.

This persistent cross-equatorial southerly meridional wind stress in the *flx10* experiment significantly contributes to the realistic SST annual cycle in the eastern Pacific. Xie (1994) and Li and Philander (1996) revealed that this south-north asymmetric structure is important in determining the annual cycle. By constantly removing a given amount of heat from the sea surface near the South American coast as designed in the flux correction scheme, a larger air mass contrast is produced between the north and south of equator due to the change of the density of air above. The larger pressure gradient across the equator forces a cross-equatorial southerly. Both the evaporation and upwelling are correspondingly strengthened off the coast of South American, where the thermocline is shallow. Consequently, the SST is reduced there, and the meridional SST gradient and thus the cross-equatorial southerly are reinforced. Although the heat flux correction is constantly applied at certain place, it can be balanced by the sensible, latent, and long-wave radiative surface heat fluxes, which are all responsive to the flux correction and induce changes of SST and surface wind. The ocean transport processes (*e.g.*, advection and diffusion) also can adjust the heat balance. When a new equilibrium is reached, the south-north asymmetry in mean state is established in the eastern Pacific. In addition, there is a seasonal variation in the persistent cross-equatorial southerly wind, intense during the northern summer while relaxed during the southern summer. Through the evaporation, the "cold tongue" below develops in the northern summer and decays during the southern summer. Thus, an annual cycle of SST is present in the equatorial eastern Pacific.

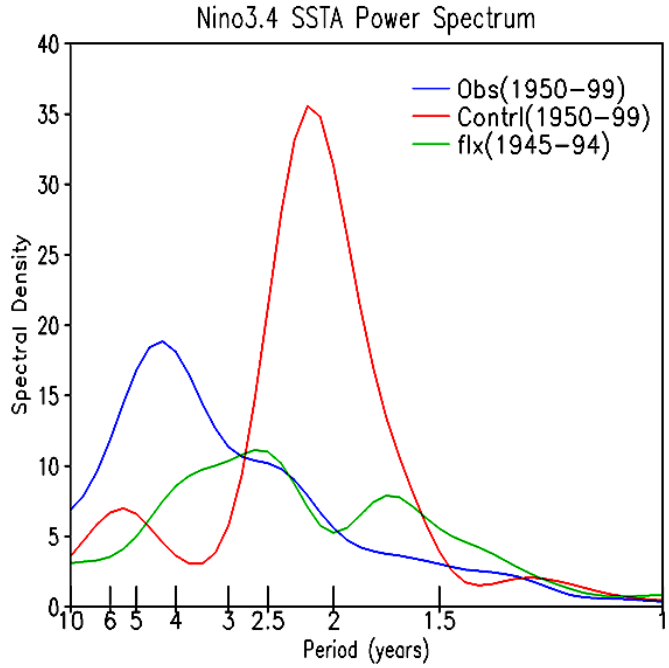

Fig. 5. Power spectrum of 50-year Nino3.4 SST anomaly index. The observed SST data is from Hadley center monthly mean SST for1950-1999; *contrl* is for 1950-1999; and *flx10* is for 1945-1994.

4.3. ENSO simulation

The power spectrum analysis on the Nino3.4 SST anomaly index reveals the dominant frequencies among the interannual variability and their corresponding amplitudes. The spectral density calculation is based on the Fourier method. Figure 5 presents the power spectrum of the 50-year Nino3.4 SST anomaly index with seasonal cycle removed for the observations and the two experiments. In the observations, a dominant 4-years period and a secondary dominant quasi-biennial period are indicated by the peaks of the spectral density. However, the *contrl* experiment exhibits a distinct and robust quasi-biennial oscillation, which is a major deficiency of CCSM3 (Deser *et. al.* 2006). In contrast, the biennial oscillation is absent in *flx10* and replaced by a dominant period of 3 years and a secondary dominant period of 1.5 years in a broader spectral band, which is closer to the observations. The overall area under the spectral density curve in the *flx10* experiment is much less than those from the observations and in *contrl*, indicating that the surface flux correction weakens the amplitude of the model interannual variability.

The modification of the ENSO period is also reflected in the evolution of the composite ENSO event represented by the Nino3.4 SST anomalies in Figure 6. The thin curves with various colors refer to the individual events, chosen with the criteria that the averaged Nino3.4 SST anomaly indexes for five consecutive months from October to the February in the following year is greater than or equal to (less than)

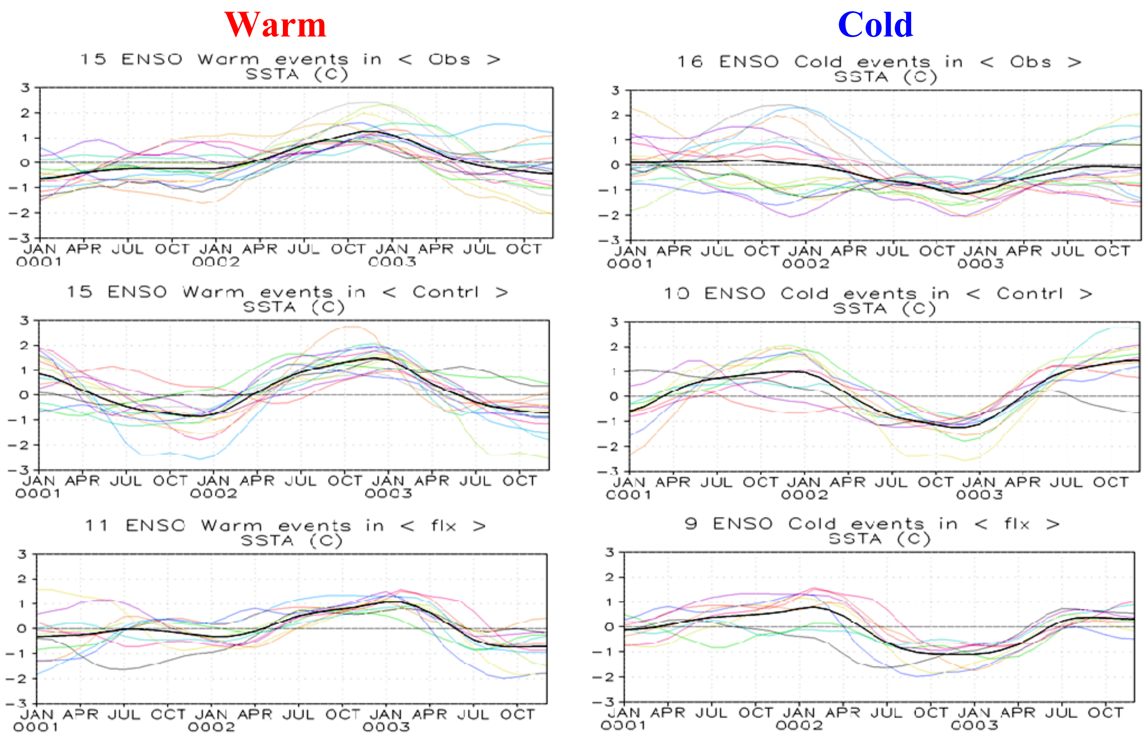

Fig. 6. The evolution of composite ENSO events represented by the Nino3.4 SSTA. The colorful curves are individual cases and the black curves are the average of those individual cases.

3/4 (-3/4) standard deviation. The thick black curve is the average of all events or a composite ENSO cycle. It is clear that, taking the warm event for example, a warm event is immediately preceded by a cold event as a demonstration of the feature of biennial oscillation in the *contrl* experiment. In contrast, the evolution of the warm event in the heat flux corrected experiment more resembles the observed one, which is usually developed from a more neutral state in stead. Similar results are displayed in the composite cold events as shown in the right panel of Figure 6. As mentioned in section 4b, a stronger annual cycle is reproduced in the eastern Pacific due to the realistic south-north asymmetric structure. The irregularity of ENSO is likely the result of the nonlinear interaction of this annual cycle with the interannual variability (Tziperman *et al.* 1994; Jin *et al.* 1994).

4.4. ENSO prediction

The skill of forecasts is accessed by the anomaly correlation coefficient (ACC) and the root mean square error (RMSE) against the corresponding observations as shown in Figure 7. The ACC measures similarities in phase of the forecasts and observations and the RMSE measures the average magnitude of the error. Note that both forecast and the observations are anomalies deviated from their corresponding monthly climatology. It has been found empirically that the level ACC=60% corresponds to the limit where the forecast does not exhibit any significant synoptic skill, thus it is used for the minimum score of a useful prediction skill in this study.

Figure 7 gives the skill score for the January forecast as a function of the lead month. The skill score of a persistence forecast is taken as a reference for baseline skill. In general, skill scores of both the control and flux corrected forecasts drop steadily with respect to the leading month. During the first 4 months, the hindcasts may be influenced by the "spring barrier". They become more skillful than the persistence forecast beyond the first 3 months. At the first 6 months lead time, the skill scores for both the forecast *contrl* and *flx10* are relative high (> 0.7) but largely indistinguishable from each other. At longer lead times of 7-9 months, the forecast *flx10* has higher skill (around 0.7) than the forecast *contrl*. Its RMSE shows slower error growth during this period, consistent with the ACC. The forecast *contrl* and *flx10* have comparable error in the first 6 months. The forecast *contrl* has larger errors of up to 0.3 °C at lead times of 7-9 months. However, their difference is not statistically significant at the 90% level as denoted by the green dots in ACC plot. Therefore, the robustness of improved prediction skill in the heat flux corrected hindcasts needs to be tested with more cases (17 years in the current study).

The skill scores for the July forecasts are shown in Figure 8. The forecast *flx10* has a skillful forecast up to 11 months, whereas the control forecasts are skillful for only the first 9 months. Both have similar skill in the first 8 months. After that time, the forecast skill drops rapidly in the forecast *contr*l, which might be related to the “spring barrier”. At lead times of 9-11 months, the forecast *flx10* has higher prediction skill than the forecast *contrl* with the higher ACC and lower RMSE, up to 0.2 and 0.2 °C respectively. However, their differences are again not statistically significant at 90% levels.

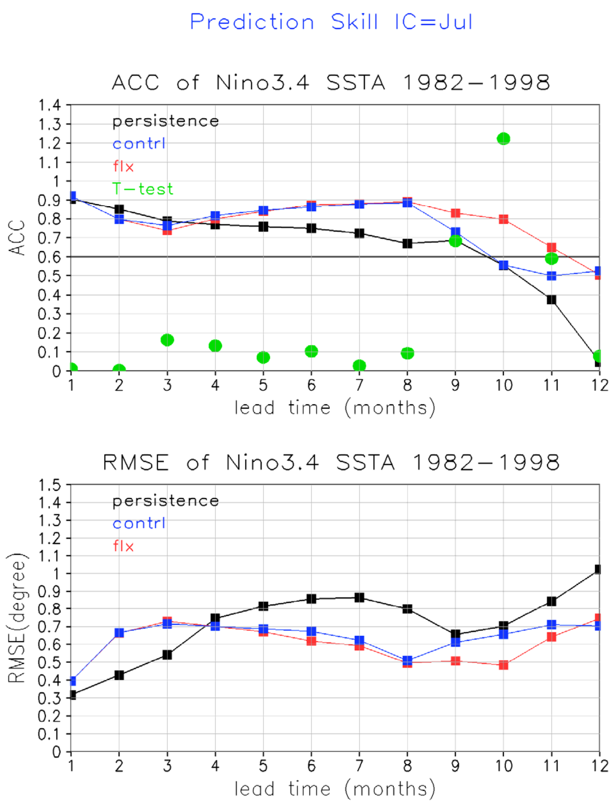

Fig. 8. Same as Figure 7 but for July forecast.

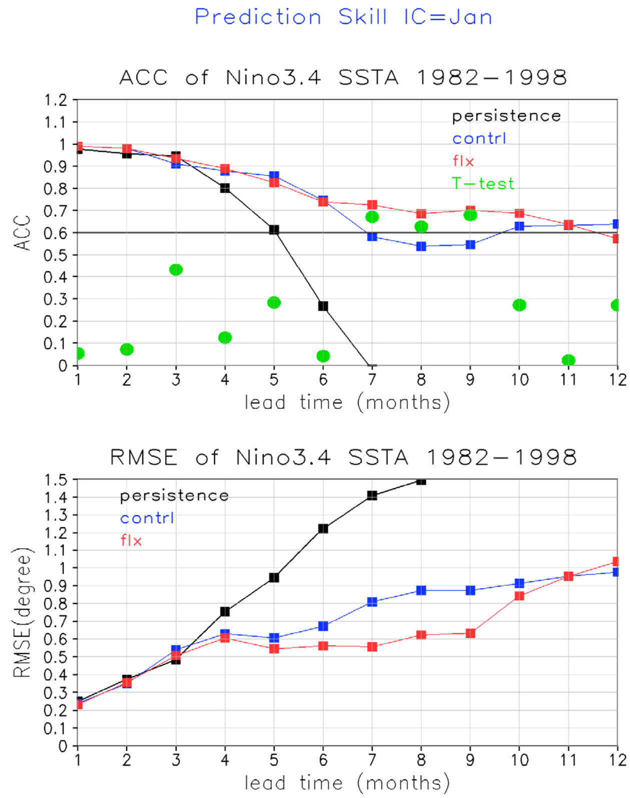

Fig. 7. Prediction skill measured by anomaly correlation coefficient (ACC) and root mean square error (RMSE) for January forecast using the Nino3.4 SSTA from 1982 to 1998. The skill of the persistence forecast is denoted by black curve, and the ensemble mean forecast *flx10* is denoted by red curve and *contrl* by blue curve. In the panel of ACC, the green dot represents the standardized difference (Ref. *http://davidmlane.com/hyperstat/B8712.html*) of the skill between forecast flx10 and contrl at each lead month. Its value refers to the scale on the right side. If the value is beyond 1.64, their difference is significant at the level 90% using student T test. The line ACC=0.6 denotes the criteria of a useful prediction skill.

5. Summary

In this study we have investigated the impact of mean climate on the simulation, prediction and predictability of ENSO. A time-independent surface heat flux correction scheme is designed to modify the mean climate by correcting the mean climate biases in CCSM3. The main results are summarized below.

(1) The mean climate is improved in the heat flux corrected simulation with reduced warm biases off the coast of Peru and reproducing a persistent southerly in the eastern equatorial Pacific.

(2) A realistic annual cycle of SST in the eastern Pacific is generated in the heat flux corrected simulation because of the more realistic asymmetry in the mean climate there. Like CCSM3, many GCMs

have a difficulty to simulate a realistic annual cycle. Therefore, this study indicates that this problem might be resolved by improving the mean climate structure there.

(3) The ENSO behavior appears sensitive to the improvement of mean climate. An irregular cycle with longer period is simulated in the heat flux corrected run.

(4) This study indicates a slightly higher prediction skill of ENSO by improving the mean climate in the heat flux corrected hindcasts, although its robustness needs verification.

References

AchutaRao, K. and K. Sperber, 2002: Simulation of the El Niño Southern Oscillation: results from the coupled model intercomparison project. *Clim. Dyn.*, **19**, 191-209.

Bjerknes, J., 1969: Atmospheric teleconnections from the equatorial Pacific. *Mon. Wea. Rev.*, **97**, 163–172.

Cane MA, Zebiak SE, Dolan SC. 1986: Experimental forecasts of El Niño. *Nature*, **321**, 827–832.

Collins, W.D., C.M. Bitz, M.L. Blackmon, G.B. Bonan, C.S. Bretherton, J.A. Carton, P. Chang, S.C. Doney, J.J. Hack, T.B. Henderson, J.T. Kiehl, W.G. Large, D.S. McKenna, B.D. Santer, and R.D. Smith, 2006: The Community Climate System Model Version 3 (CCSM3). *J. Climate*, **19**, 2122–2143.

Davey, M., M. Huddleston, K.R. Sperber et al., 2002: STOIC: A study of coupled model climatology and variability in tropical ocean regions, *Clim. Dyn.*, **18**, 403-420.

Deser, C., A. Capotondi, R. Saravanan, and A. Phillips, 2006: Tropical Pacific and Atlantic climate variability in CCSM3. *J. Climate*, **19**, 2451–2481.

Doney, S.C., W.G. Large, and F.O. Bryan, 1998: Surface ocean fluxes and water-mass transformation rates in the coupled NCAR Climate System Model. *J. Climate*, **11**, 1420–1441.

Kirtman, B. P. and D. Min, 2008: Multi-model ensemble prediction with CCSM and CFS. *Mon. Wea. Rev.* (in press).

Jin, F.-f., J. D. Neelin and M. Ghil, 1994: El Niño on the Devil's Staircase: Annual subharmonic steps to chaos, *Science*, **264**, 70-72.

Joseph, R., and S. Nigam, 2006: ENSO evolution and teleconnections in IPCC's twentieth-century climate simulations: Realistic representation? *J. Climate*, **19**, 4360–4377.

Latif, M., K. Sperber, and co-authors, 2001: ENSIP: intercomparison project. *Clim. Dyn.*, **18**, 255-276.

Li, T., and S.G.H. Philander, 1996: On the annual cycle of the eastern equatorial Pacific. *J. Climate*, **9**, 2986-2998.

Li, Tianming, Hogan, Timothy F, 1999: The role of the annual-mean climate on seasonal and interannual variability of the tropical Pacific in a coupled GCM. *J. Climate*, **12**, 780-792.

Manganello, Julia V.; Huang, Bohua, 2008: The influence of systematic errors in the Southeast Pacific on ENSO variability and prediction in a coupled GCM. *Climate Dynamics*, DOI:10.1007/s00382-008-0407-5.

Mechoso, CR, AW Robertson, and Co-authors 1995: The seasonal cycle over the tropical Pacific in general circulation models. *Mon. Wea. Rev.*, **123**, 2825-2838.

Neelin, J. D.; Latif, M.; Allaart, M. A. F.; Cane, M. A.; Cubasch, U.; Gates, W. L.; Gent, P. R.; Ghil, M.; Gordon, C.; Lau, N. C.; Mechoso, C. R.; Meehl, G. A.; Oberhuber, J. M.; Philander, S. G. H.; Schopf, P. S.; Sperber, K. R.; Sterl, K. R.; Tokioka, T.; Tribbia, J.; Zebiak, S. E., 1992: Tropical air-sea interaction in general circulation models. *Clim. Dyn.*, **7**, 73-104.

Tziperman, E., L. Stone, M. A. Cane and H. Jarosh, 1994: El Niño Chaos: Overlapping of resonances between the seasonal cycle and the Pacific Ocean-Atmosphere oscillator. *Science*, **264**, 72-74.

Weaver, A.J. and T.M.C Hughes, 1996: On the incompatibility of ocean and atmosphere models and the need for flux adjustments. *Clim. Dyn.*, **12**, 141-170.

Xie, S.P., 1994: On the genesis of the equatorial annual cycle. *J. Climate*, **7**, 2008–2013.

Science and Technology Infusion Climate Bulletin
NOAA's National Weather Service
33rd NOAA Annual Climate Diagnostics and Prediction Workshop
Lincoln, NE, 20-24 October 2008

Synoptic-Scale Convective Environment Climatology by ENSO Phase in the North Central United States

Barbara E. Mayes[1], Joshua M. Boustead[2], Craig Cogil[3], Glenn R. Lussky[4]
Jeffrey S. Boyne[4] and Richard S. Ryrholm[5]

[1]*NOAA/NWS WFO Omaha/Valley, NE;* [2]*NOAA/NWS WFO Topeka, KS*
[3]*NOAA/NWS WFO Des Moines, Iowa;* [4]*NOAA/NWS WFO La Crosse, Wisconsin*
[5]*NOAA/NWS WFO Sioux Falls, South Dakota*

1. Introduction

The El Niño-Southern Oscillation (ENSO) is known to affect synoptic patterns across the continental United States, particularly by its impact on the upper tropospheric jet stream position. Global circulation patterns influence synoptic weather patterns by impacting the location of mid-tropospheric ridge and trough locations and thus areas favorable for temperature and precipitation anomalies, which in turn influence regional severe weather activity. Though it is one of several factors associated with the potential for severe weather, the synoptic environment plays a key role in severe weather potential by providing favorable ingredients for the development of severe convection (e.g. Miller 1967). While ENSO is one of many factors that influence global circulations, and by distillation may have a less distinguishable influence on the synoptic pattern, coherent signals can be uncovered in the synoptic environment, based on ENSO phase, that would influence the potential for severe convection in the north central United States. Seasonal predictions of severe weather potential are not much aid for daily operations, but they can be used by emergency managers, the media, and forecasters to increase preparedness for seasons that have the potential for above normal convective activity.

Previous studies have investigated the relationship between ENSO and tornado climatology in the United States and Canada, with varying definitions of ENSO and methodologies (Bove and O'Brien, 1998; Browning 1998; Etkin et al., 2001; Wikle and Anderson, 2003). Agee and Zurn-Birkhimer (1998) determined that an axis of increased tornado activity during La Niña years extended from Iowa through Illinois and Indiana into Kentucky and Tennessee, while an axis of increased tornado activity during El Niño years extended from Colorado and New Mexico through the Texas panhandle into Oklahoma and Missouri. They concluded that their findings were a result of geographical shifts in tornado activity, rather than an overall increase or decrease in activity nationwide based on ENSO phase. Bove (1998) found a similar axis of increased activity in La Niña years. Additionally, Cook and Schaefer (2008) found significant relationships between ENSO phase and winter (January-March) tornado activity in the southern Plains, the Southeast, and the Ohio Valley areas.

Mayes et al (2007; hereafter M07) found statistically significant correlations across parts of the Plains and Mississippi River valley between ENSO phase and tornado activity. An elevated risk of an increased number of tornado days and significant tornadoes was noted in parts of the central Plains and mid-Mississippi River valley during a La Niña, while these areas experienced diminished potential for above average tornado activity (and an increased potential for below average activity) during an El Niño. The results of M07 prompted this study, investigating whether these spatially consistent statistical results had a foundation in the larger scale synoptic pattern influencing convective, and hence tornadic, activity.

The use of reanalysis data is an accepted means to investigate synoptic-scale convective parameters, even though the coarse horizontal and vertical resolution is likely to miss features important to convective development for any given day. Brooks et al. (2007) investigated convective parameters via reanalysis data with the purpose of creating a climatology of those relevant parameters. Schultz et al. (2007) also utilized

Correspondence to: Barbara E. Mayes, Barbara E. Mayes, National Weather Service, 6707 N. 288th St., Valley, NE.
E-mail: Barbara.Mayes@noaa.gov

reanalysis data in an examination of the influence of the synoptic environment on dryline intensity. While not able to resolve mesoscale and storm-scale features, global reanalysis data can provide insight into the synoptic environment, which certainly influences the potential for convection, including severe weather.

The National Weather Service (NWS) Climate Prediction Center (CPC) has defined typical upper-level jet stream and sensible weather anomalies during January-February-March (Fig. 1). During an El Niño, the subtropical upper-level jet is suppressed southward over the southwestern United States and toward the Gulf of Mexico, inducing anomalously wet conditions across its track. The nearly zonal flow across the northern and central U.S. is typically left drier than average, with warm conditions as the polar jet remains north of the continental United States (e.g., Ropelewski and Halpert, 1987). During a La Niña, the upper-level jet pattern is more amplified and often comes ashore near the Pacific Northwest, inducing wet anomalies there. A blocking high pressure in the Gulf of Alaska often aids a more meridional component to the upper-level flow across the central U.S. and allowing for colder weather to seep into the northern tier. The southern U.S. typically remains drier and warmer than average, with the storm track remaining further north. While individual El Niño and La Niña episodes do deviate to some extent from the typical patterns in Fig. 1, the tendencies are present throughout the varying episodes.

While this study investigates springtime conditions, it is useful to note CPC's ENSO impacts as the antecedent conditions to that season. Similar upper-level flow patterns can be expected in the spring, particularly early in the season as the transition to a summer pattern occurs. It is worth noting that it is beyond the scope of this study to investigate mesoscale and smaller scale features, such as frontal boundaries and locally enhanced low-level shear that do have an impact on tornadogenesis. Rather, this study focuses on features of the synoptic scale patterns that can be resolved on the coarse grid spacing found in reanalysis data, such as trough patterns and mid and upper level flow, that create an environment favorable for convective activity.

2. Data and method

Data used in this paper were selected to be consistent with M07, including the use of an operational definition for ENSO as well as a source of reanalysis data available for the entire study period of 1950-2005.

2.1 ENSO definition

The National Oceanic and Atmospheric Administration (NOAA) developed an operational definition for ENSO utilizing the Oceanic Niño Index (ONI). ONI is defined as the three-month running average sea surface temperature anomaly in the Niño 3.4 region. An El Niño occurs when ONI is at least 0.5 °C for at least five consecutive 3-monthly periods, or "seasons"; conversely, La Niña conditions occur when ONI reaches –0.5 °C or less for five consecutive seasons.

The ONI has been calculated by 3-month period and is available online via NOAA's Climate Prediction Center (CPC) back to 1950 (Smith and Reynolds, 2003). The NOAA definition of ENSO based on ONI is followed in this study.

2.2 Data source and methodology

With the intent of investigating synoptic patterns during the peak of the convective season in the north central United States, the focus was narrowed to the four-month period of March-April-May-June (MAMJ). Each year from 1950 to 2005 was classified based on the ENSO phase present during each three-month period, or "season", affecting MAMJ, ranging from January-February-March through June-July-August. MAMJ periods that began in a given ENSO phase during those seasons affecting MAMJ but ended as neutral were placed in a category for each, "La Niña Going Out" and "El Niño Going Out." MAMJ periods that began as neutral during those seasons affecting MAMJ but transitioned to a given ENSO phase were categorized alongside those MAMJ periods that remained within a given ENSO phase for their entire length, creating categories for "La Niña In or Going In" and "El Niño In or Going In." Finally, seasons remaining in the neutral phase throughout the duration were categorized as such. Four MAMJ periods saw a transition directly from one ENSO phase to the opposite and were left out of the phase-based composites. The years included in each category are depicted in Table 1.

Phase	Years
La Niña	
In or Going In	1950, 1954, 1955, 1956, 1964, 1970, 1971, 1974, 1975, 1999
Going Out	1951, 1962, 1968, 1976, 1985, 1989, 1996, 2000, 2001
Neutral	1952, 1953, 1959, 1960, 1961, 1967, 1978, 1979, 1980, 1981, 1984, 1986, 1990
El Niño	
In or Going In	1957, 1963, 1972, 1982, 1987, 1991, 1993, 1994, 1997, 2002, 2004
Going Out	1958, 1966, 1969, 1977, 1983, 1992, 1995, 2003, 2005
Not Included	1965, 1973, 1988, 1998

Table 1 Years included in each ENSO phase to create composite images. Years not included were those that switched from one ENSO phase to the opposite during the 3-month seasons overlapping the March-June study period.

Composite images of synoptic parameters were created using National Center for Atmospheric Research (NCAR)/National Centers for Environmental Prediction (NCEP) reanalysis data (Kalnay et al, 1996). The data were obtained via the NOAA Earth Systems Research Laboratory website (http://www.cdc.noaa.gov/cgi-bin/Composites/printpage.pl). Data were then converted for visualization in the General Meteorological Package software (GEMPAK; DesJardins et al. 1991). Synoptic parameters were investigated based on the five categories delineated in Table 1. Major parameters such as temperature, wind, and geopotential height were available directly, while others such as bulk shear and dewpoint temperature could be derived from the basic parameters available.

3. Results and discussion

The synoptic parameters indeed exhibited tendencies based on the five phases investigated. The features examined did resemble the expected synoptic patterns illustrated schematically in Fig. 1, which helps lend credibility to their representativeness of each ENSO phase. Notably, the "in or going in" phases for both El Niño and La Niña did not necessarily resemble the "going out" phase closely. The La Niña In or Going In phase was closest to a classic La Niña schematic, while the El Niño Going Out phase most closely resembled the El Niño schematic.

Standard synoptic fields were examined for each of the five phases, including fields such as 300 hPa winds, 500 hPa geopotential height, 700 hPa temperatures, 850 hPa dewpoint temperatures and winds, and mean sea level pressure. The anomaly fields for each parameter in each phase were examined in relation to the mean fields through the 1950-2005 study period. Features that are accepted as creating a

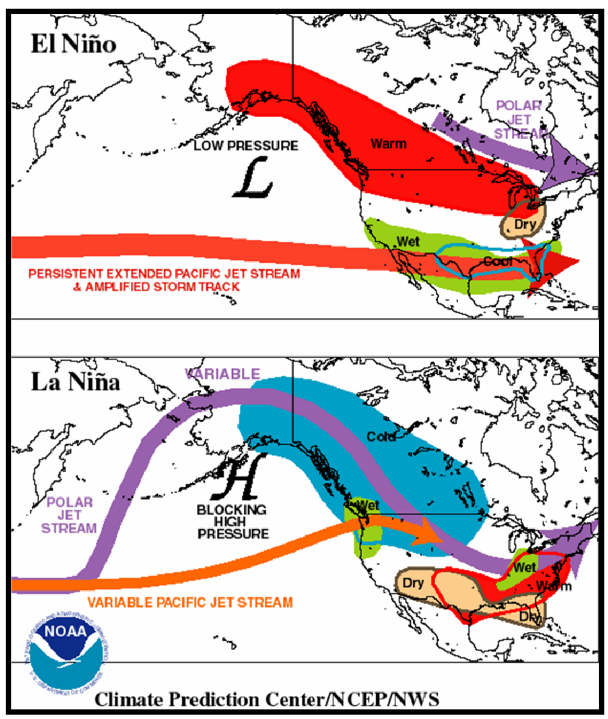

Fig. 1 Typical January-March weather anomalies and atmospheric circulation during moderate to strong El Nino and La Nina (from CPC).

favorable, or hostile, synoptic environment for the development and maintenance of convection were then possible to distinguish in each phase.

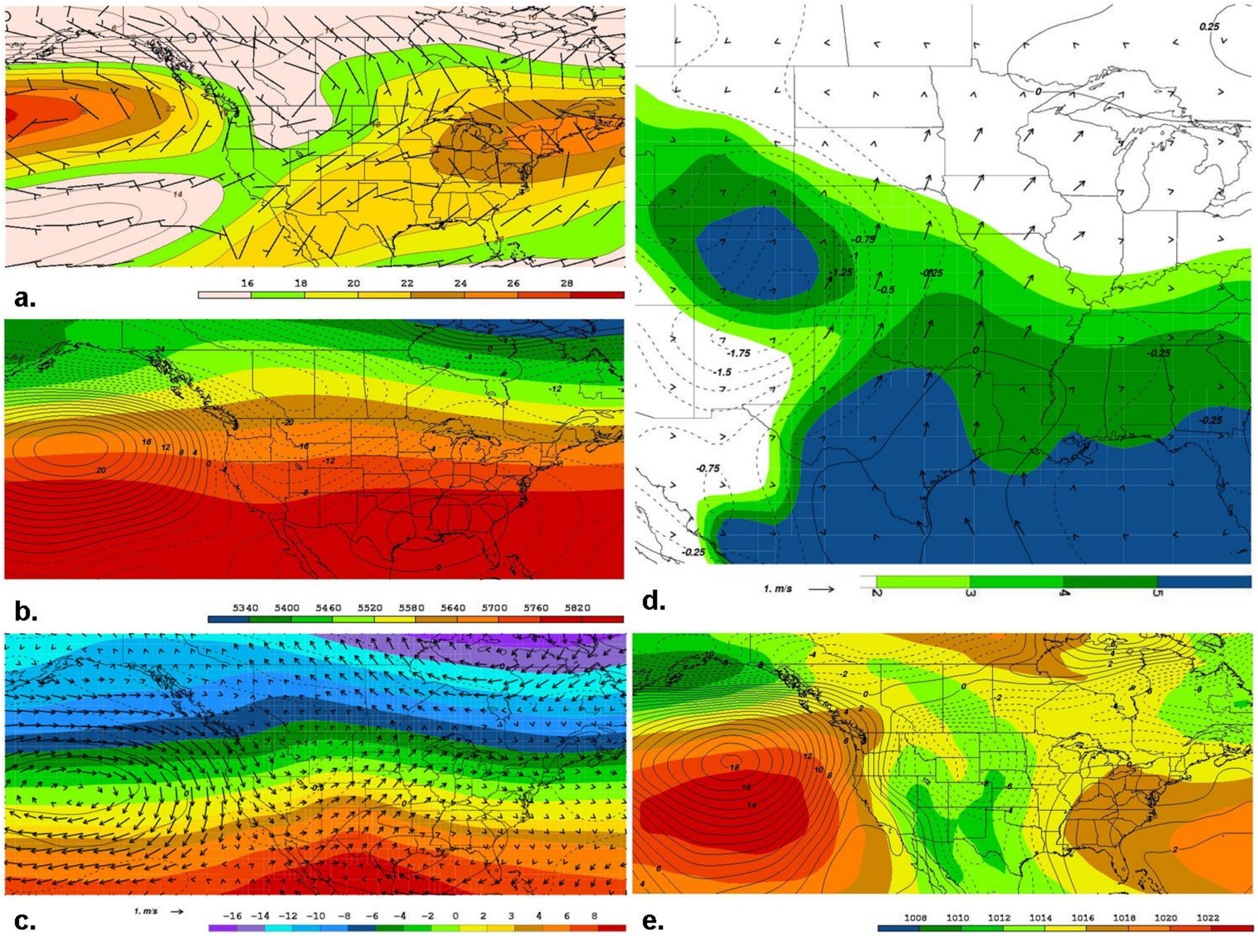

Fig. 2 March-June mean and anomalous synoptic fields during an ongoing or developing La Niña ("La Niña In or Going In"). a. 300 hPa mean 1950-2005 winds (shaded) and phase anomalies (barbs). b. 500 hPa mean 1950-2005 geopotential height (shaded) and phase anomalies (contours). c. 700 hPa mean 1950-2005 temperature (shaded), phase temperature anomalies (contours), and phase wind anomalies (vectors). d. 850 hPa mean 1950-2005 dewpoint temperature (shaded), phase dewpoint anomalies (contours), and phase wind anomalies (vectors). e. Mean 1950-2005 mean sea level pressure (shaded) and phase anomalies (contours).

3.1. La Niña In or Going In

Perhaps more than any other phase, features during an established or developing La Niña showed distinct trends that may help explain some of the statistical trends noted in M07. In this case, the features support the establishment of a favorable convective environment across much of the central and southern Plains into the mid to lower Mississippi River Valley. At 300 hPa (Fig. 2a), the subtropical upper-level jet is enhanced across the southern Plains, with increased southwesterly flow into the Plains and Midwest. An anomalous upper-level trough is present in the Rockies (Fig. 2b), with the anomalous high over the Gulf of Alaska noted at 500 hPa as well. Temperatures at 700 hPa are anomalously high in the South and cool across the north central and northwestern CONUS (Fig. 2c), indicating an enhancement of the baroclinicity across the central U.S., with anomalously strong southwesterly flow across the central CONUS. The low-level jet at 850 hPa (Fig. 2d) is notably enhanced across the Plains, with a distinct dry pocket extending from the Rockies onto the High Plains. The dry anomaly may indicate an eastward displacement of the mean dryline position, a feature known to aid convective development, and may also indicate an anomalously strong mean dryline. Mean sea level pressure anomalies reflect 500 hPa anomalies (Fig. 2e), with an anomalous surface low in the lee of the Rockies and high pressure off the Northwest Pacific coast.

Overall, anomalous features present during a La Niña are often associated with a favorable synoptic environment for convection, including the potential for tornadic activity. The pattern of a trough in the Rockies, strong southwesterly upper-level flow, an enhanced low-level jet, and the presence of baroclinicity are, as a group, a classic severe weather environment. It is no surprise, then, that large portions of the study area of the north central U.S., particularly the central Plains and the Mississippi River Valley, exhibit an enhanced potential for tornado activity in the highest tercile of the period.

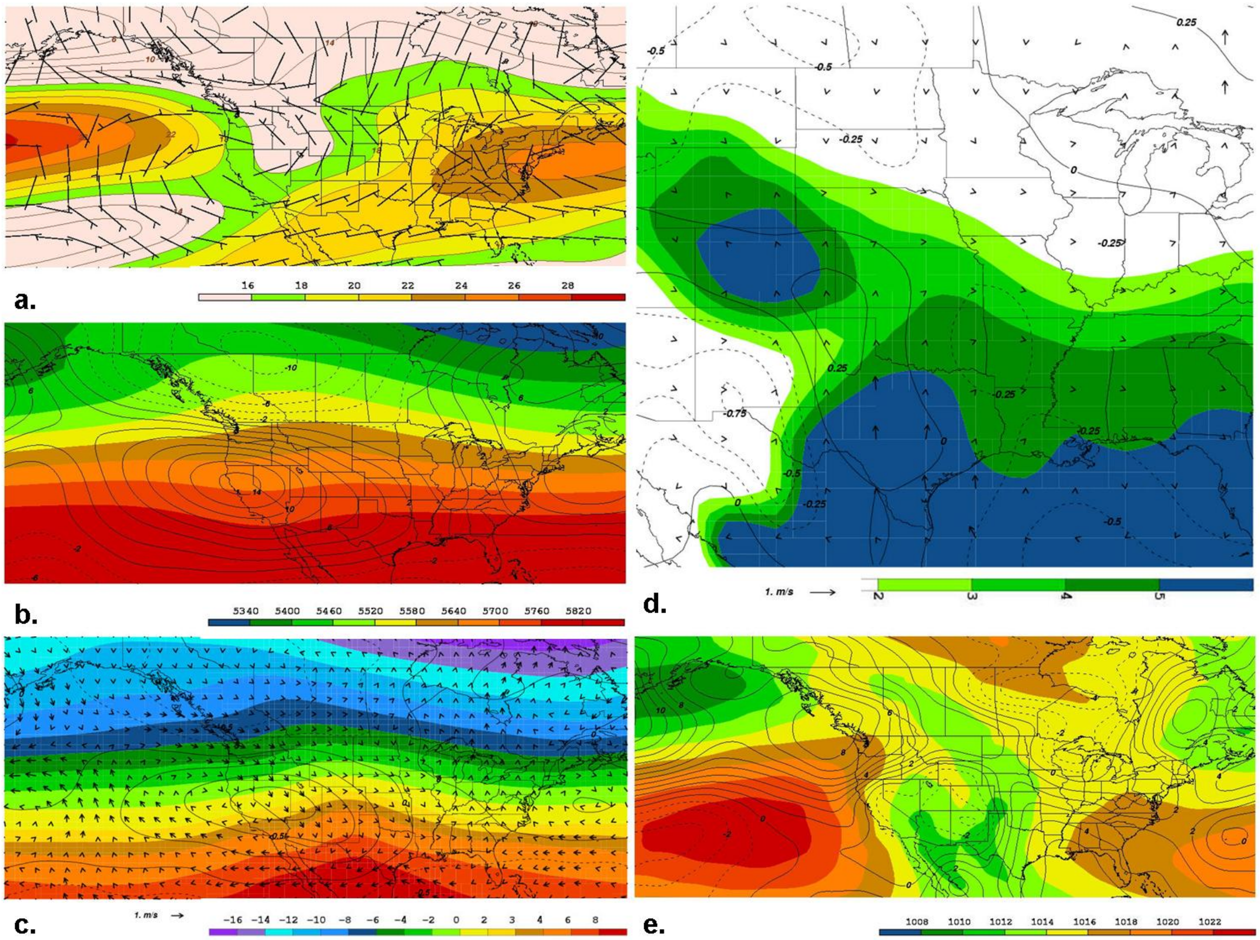

Fig. 3 As in Figure 2, but for a weakening La Niña ("La Niña Going Out").

3.2. La Niña Going Out

Features during a weakening La Niña episode do exhibit some of the characteristics of an ongoing or developing La Niña event, but also exhibit a trend toward the neutral conditions (not shown). At 300 hPa (Fig. 3a), the subtropical jet is clearly displaced southward and out of the CONUS, with easterly anomalies across the southern U.S. Northwesterly flow is present across the north central U.S., consistent with an unsettled weather pattern. An anomalously strong upper-level high is present in the western U.S. (Fig. 3b), again supporting northwesterly flow. Temperatures at 700 hPa are anomalously warm across much of the western two-thirds of the U.S. (Fig. 3c), with a cool anomaly further north in Canada creating an area of enhanced baroclinicity across the northern tier of the CONUS. Anomalously strong southerly flow is still evident into the Plains at 850 hPa (Fig. 3d), though not as strong as during an ongoing or developing La Niña.

A pool of anomalous moisture is present in the southern and central High Plains. The anomalous low pressure is displaced westward into the Rockies, with a weakening of the lower pressures apparent as a high pressure anomaly in the central Plains toward the Mississippi River valley (Fig. 3e).

Features during a dissipating La Nina do still support convective activity, particularly in the High Plains, where the moisture anomaly and low pressure anomaly best coincide. With northwesterly flow and enhanced baroclinicity in the northern Plains, that region would also be favorable for enhanced convective activity. Again, the convective environment supports the findings of M07.

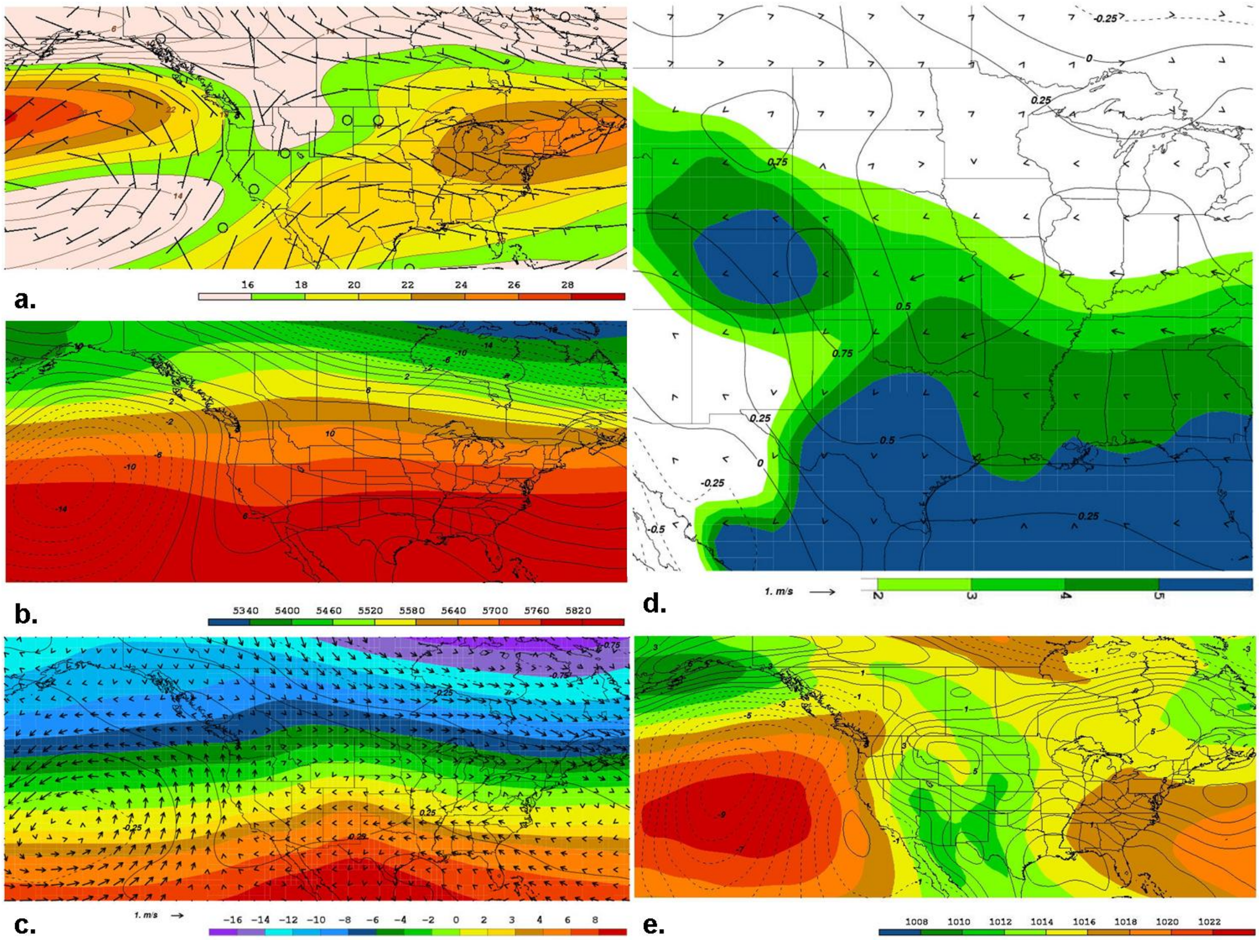

Fig. 4 As in Figure 2, but for an ongoing or developing El Niño (“El Niño In or Going In”).

3.3. El Niño In or Going In

Interestingly, much like a weakening La Niña, the pattern for an established or developing El Niño is something of a blend between the classic El Niño synoptic pattern (Fig. 1) and neutral conditions. Anomalies during this phase are, in general, weaker than the other phases, though still notable enough to deviate from the mean pattern. Winds at 300 hPa are weakened across the central U.S. (Fig. 4a), as during a dissipating La Nina. With an anomalous upper-level low off the coast of the Pacific Northwest (Fig. 4b), however, flow is also weakened in the northern CONUS. Weak anomalous upper-level ridging is induced across most of the CONUS. Little in the way of a temperature change at 700 hPa is present (Fig. 4c), and winds are anomalously weakened as depicted by northeasterly wind anomalies in the mid and lower Mississippi River valley. A weak 850 hPa moisture anomaly is again present in the southern and central High Plains (Fig. 4d), though 850 hPa winds are also suppressed by northeasterly anomalies in the southern Plains toward the mid

Mississippi River Valley. In a surface reflection of the upper-level anomalies, mean sea level pressure across the CONUS exhibits high pressure anomalies (Fig. 4e), centered on the northern Rockies and the Gulf states.

Statistical relationship between an ongoing or developing El Niño and tornado activity are weaker than those during a La Niña, and tend to indicate suppression across the southern and central Plains toward the mid Mississippi River Valley. With anomalous upper-level and surface ridging, as well as suppressed mid-level winds, it is not surprising that convection may tend to be suppressed in that environment. Weakened 850-700 hPa winds likely correspond to diminished 0-3 km shear, corresponding to a decreased threat of tornado-producing convection.

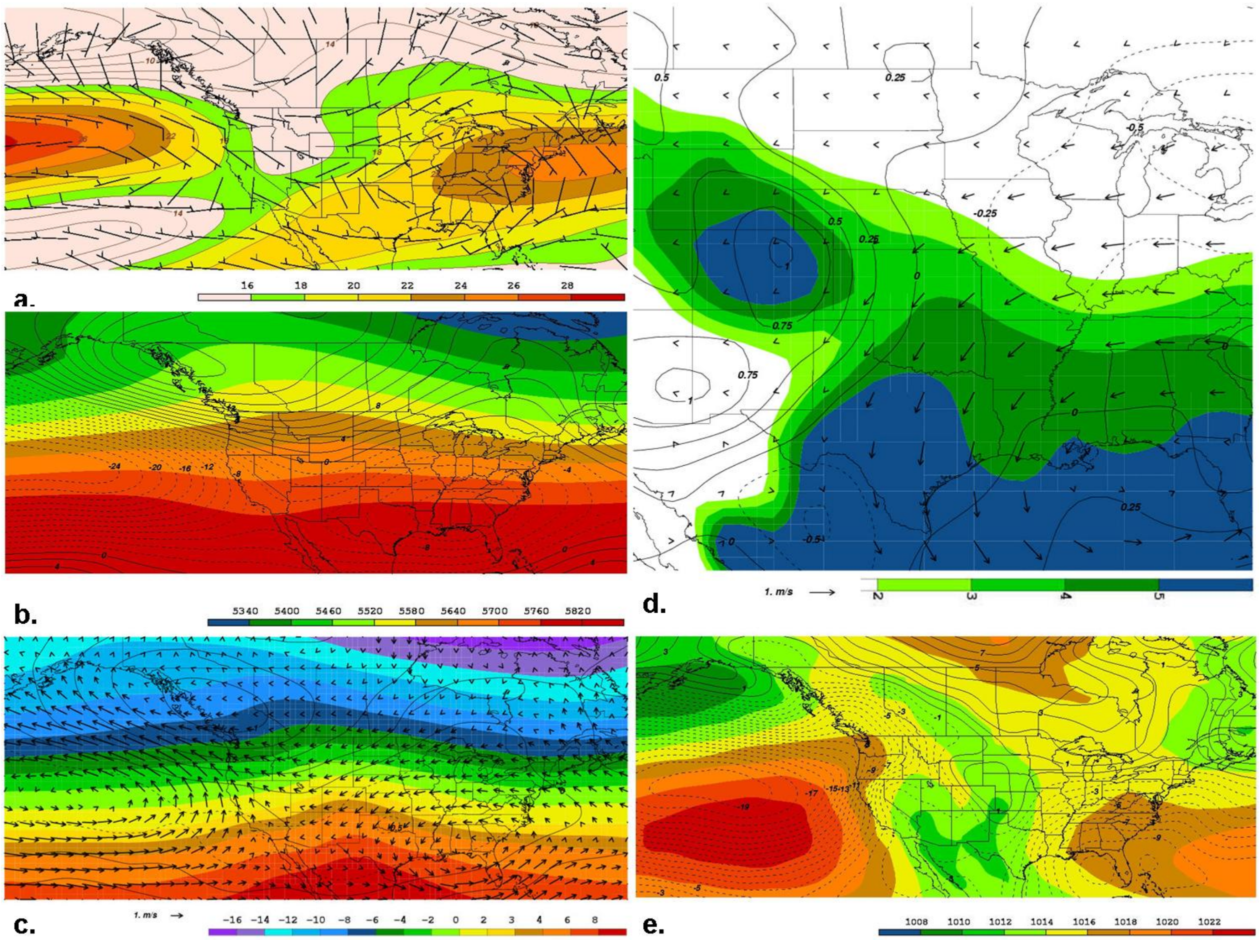

Fig. 5 As in Figure 2, but for a weakening El Niño ("El Niño Going Out").

3.4. El Niño Going Out

Features during an outgoing El Niño, or in the convective season following a wintertime El Niño, are close to a classic El Niño pattern (Fig. 1). Wind anomalies at 300 hPa indicate that the subtropical jet is displaced southward toward the Gulf of Mexico (Fig. 5a), with diminished flow across much of the CONUS. Anomalous upper-level lows are noted in both the Gulf of Alaska and the southeastern U.S. (Fig. 5b), with a positive height anomaly reaching into the north central and northwestern CONUS, inducing a blocking flow pattern in the north central U.S. Baroclinicity at 700 hPa is decreased, as noted by cool anomalies to the south and warm anomalies to the north, with stronger northeasterly wind anomalies indicating winds across the Plains and Mississippi River Valley are further suppressed (Fig. 5c). Suppressed winds are also noted at 850 hPa (Fig. 5d), with dry anomalies reaching the Midwest and moist anomalies lingering in the Rockies.

Mean sea level pressure is again a reflection of the upper-level flow, with anomalous ridging across much of the Plains between low pressure anomalies in the Gulf of Alaska and the southeastern U.S (Fig. 5e).

M07 indicated an increased potential for suppressed tornadic activity following a winter El Niño, a result that is supported by examining the synoptic environment during that phase. Weakened mid-level winds, as well as upper-level and surface anomalous ridging, create a mean environment during this phase that is hostile toward convective development.

4. Conclusions and future work

The results of this study indicate that the statistically significant changes to the climatology of tornadic activity noted in M07 can be linked to changes in the synoptic-scale pattern. During a La Niña, and particularly when a La Niña is ongoing throughout or begins during the peak convective season of MAMJ, an anomalous trough in the Rockies, as well as increased baroclinicity across the Plains, support the potential for enhanced tornadic activity. Similarly, during an El Niño, and particularly when an El Niño through the winter months is weakening to a neutral phase, an anomalous upper-level high exists over the central U.S., along with suppressed low-level flow off the Gulf of Mexico, a pattern which is typically not conducive to severe weather in southern portions of the study area. The finding again supports the statistical results from M07 that tornadic activity tends to be suppressed in those regions.

It is important to note that the ENSO cycle is one of many factors that influence weather across the north central U.S. Other less predictable climate signals, such as the North Atlantic Oscillation, and shorter term climate anomalies, such as the Madden-Julian Oscillation, likely also have an influence on large-scale weather patterns. In addition, because tornadoes are ultimately caused by mesoscale or smaller scale environments, the potential for tornado activity on any given day cannot be determined by the ENSO phase occurring. Active tornado seasons do occur in phases that are, on average, not considered as favorable for an active season. Despite these limitations, ENSO does provide at least one measure of predictability of the potential for activity during a season, and this knowledge can be utilized by forecasters and planners alike.

Future work on this study will include examining more parameters that are closely connected with convection, such as instability and shear parameters, as well as investigating point soundings constructed from reanalysis data for any relevant features. It would also be beneficial to look at convective seasons from 2006-2008 in comparison to the findings of both this study and M07 to determine how well the results from individual years compare to the multi-year composites and statistical analyses.

Acknowledgments. This work was supported and aided by Ray Wolf (NWS Quad Cities IA/IL) and Daniel Nietfeld (NWS Omaha/Valley NE).

References

Agee, E., and S. Zurn-Birkhimer, 1998: Variations in USA tornado occurrences during El Niño and La Niña. Preprints, *19th Conf. on Severe Local Storms*, Amer. Meteor. Soc., 287-290.

Bove, M. C., 1998: Impacts of ENSO on United States tornadic activity. Preprints, *19th Conf. on Severe Local Storms,* Amer. Meteor. Soc., 313-316.

Bove, M. C., and J. J. O'Brien, 1998: Impacts of ENSO on United States tornadic activity. Preprints, *9th Symposium on Global Change Studies*, Amer. Meteor. Soc., 199-202.

Brooks, H. E., A. A. Anderson, K. Riemann, I. Ebbers, and H. Flachs, 2007: Climatological aspects of convective parameters from the NCAR/NCEP reanalysis. *Atmos. Research*, **83**, 294-305.

Browning, P., 1998: ENSO related severe thunderstorm climatology of northwest Missouri. Preprints, *19th Conf. on Severe Local Storms*, Amer. Meteor. Soc., 291-292.

Cook, A. R., and J. T. Schaefer, 2008: The relation of El Nino-Southern Oscillation (ENSO) to winter tornado outbreaks. *Mon. Wea. Rev*., **136**, 3121-3137.

DesJardins, M.L., K.F. Brill, and S.S. Schotz, 1991: GEMPAK User Guide. *NASA Tech. Memorandum*, 4260 pp. [Available from NASA, Code NTT-4, Washington, DC 20546-0001]

Etkin, D., S. E. Brun, A. Shabbar, and P. Joe, 2001: Tornado climatology of Canada revisited: tornado activity during different phases of ENSO. *Intl. J. Clim*. (Royal Meteorological Society), **21**, 915-938.

Kalnay, E., and Coauthors, 1996: The NCEP/NCAR Reanalysis 40-year project. *Bull. Amer. Meteor. Soc*., **77**, 437-471.

Mayes, B.E., C. Cogil, G.R. Lussky, J.S. Boyne, and R.S. Ryrholm, 2007: Tornado and severe weather climatology and predictability by ENSO phase in the north central U.S.: A compositing study. Preprints, *19th Conf. on Climate Variability and Change*, Amer. Meteor. Soc.

Miller, R.C., 1967: Notes on analysis and severe storm forecast procedures of the military weather warning center. *Tech. Rep. 200*, U.S. Air Force Air Weather Service, Scott AFB, 170 pp.

Ropelewski, C.F., and M.S. Halpert, 1987: Global and regional scale precipitation patterns associated with the El Nino/Southern Oscillation. *Mon. Wea. Rev.*, **115**, 1606-1626.

Schultz, D. M., C. C. Weiss, and P. M. Hoffman, 2007: The synoptic regulation of dryline intensity. *Mon. Wea. Rev*., **135**, 1699-1709.

Smith, T. M., and R. W. Reynolds, 2003: Extended reconstruction of global sea surface temperatures based on COADS data (1854-1997). *J. Climate*, **16**, 1495-1510.

Wikle, C. K., and C. J Anderson (2003): Climatological analysis of tornado report counts using a hierarchical Bayesian spatio-temporal model. University of Missouri, available online at http://www.stat.missouri.edu/~wikle/TORNADOpap_v3.pdf

Science and Technology Infusion Climate Bulletin
NOAA's National Weather Service
33rd NOAA Annual Climate Diagnostics and Prediction Workshop
Lincoln, NE, 20-24 October 2008

Madden-Julian Oscillation and Convectively Coupled Equatorial Waves Simulated in the NCEP Global Forecast System and Climate Forecast System Models

Kyong-Hwan Seo[1] Wanqiu Wang[2] and Jae-Kyung E. Schemm[2]
[1]*Department of Atmospheric Sciences, Pusan National University, South Korea*
[2]*Climate Prediction Center, NOAA/National Weather Service*

1. Introduction

While some of the major MJO characteristics can indeed be simulated by atmospheric models with prescribed sea surface temperatures (SST), the results from many studies suggest the importance of air-sea interaction in the MJO dynamics. Observational and modeling diagnoses have shown coherent variations in surface heat fluxes, SST, and convection associated with the MJO, indicating that interactive air-sea coupling needs to be included in numerical models to obtain a reasonable representation of the MJO.

In reality, however, improvements in the general circulation model (GCM) for the MJO simulation and forecast by this inclusion are considerably limited and dependent upon a GCM (Waliser et al. 1999; Hendon 2000; Inness and Slingo 2003; Lin et al. 2006; Seo et al. 2007; Fu et al. 2008). The recent study of Lin et al. (2006) demonstrates that only two models out of 14 coupled GCMs participating in the Intergovernmental Panel on Climate Change (IPCC) Fourth Assessment Report (AR4) are able to simulate the MJO variance and pronounced 30-60-ay period spectral peak comparable to the observations.

The deficiencies apparent in MJO simulation can be attributed to many factors not limited to the above mentioned air-sea coupling. The applied deep convection scheme is seemingly one of the most sensitive elements. Another factor is model resolutions. Time mean basic-state circulation and wind shear over the tropics are also believed to be important controlling elements for the correct MJO simulation (e.g., Inness et al. 2003). Furthermore, the appropriate representation of mean state sea surface temperature (SST) is considered a prerequisite for the improved MJO simulation since a cold SST bias adversely affects convective activity (e.g., Inness and Slingo 2003). As noted above, moisture convergence plays a crucial role in developing and sustaining the MJO. The ultimate key to the MJO simulation is dependent upon whether models accurately simulate the persistent interaction of lower-level circulation waves and deep convection, as revealed by many previous observational and modeling studies (e.g., Maloney and Hartmann 1998; Waliser et al. 1999; Seo and Kim 2003).

Recently, an atmosphere-ocean coupled Climate Forecast System (CFS) model with the horizontal resolution of T62 was developed by NCEP. Several coupled CMIP simulations using this version have been performed along with an atmosphere-alone AMIP simulation. Additionally, the higher resolution CFS model adopting a T126 grid system was run to produce long-term integrated data. Furthermore, the CFS T126 model run that employs a different deep convection scheme has been also conducted to test the impact of the cumulus scheme on various climate oscillations and teleconnections. All these simulations have made it possible to evaluate the effects of air-sea interaction, model resolution and deep convection scheme on the MJO. In addition, comparison of these runs provides an opportunity to investigate key factors for the proper MJO simulation.

In addition to the MJO evaluation, other dominant convectively coupled equatorial waves (e.g., Kelvin, equatorial Rossby (ER), mixed Rossby-gravity (MRG), inertio-gravity waves) identified theoretically by Matsuno (1966) and observationally by Wheeler and Kiladis (1999) are diagnosed in the NCEP climate model runs.

Correspondence to: Kyong-Hwan Seo, Department of Atmospheric Sciences, Pusan National University, South Korea; E-mail: khseo@pusan.ac.kr

2. The simulations and data

The AMIP simulation is performed using the GFS model with T62 resolution (referred to hereafter as GFS T62) that is forced with the observed monthly mean SST from 1982-2002. Among several CMIP long-term simulations that are conducted with the CFS model, two CMIP runs with a resolution of T62 and T126 are executed to test the sensitivity to the horizontal resolution (referred to hereafter as CFS T62 and CFS T126, respectively). This simulation is initialized from the observed analyses of 1 January 2002 and run for 21 years. The above AMIP and CMIP simulations are based on the simplified Arakawa-Schubert (SAS) cumulus parameterization scheme. Therefore an additional coupled T126 run is performed with the relaxed Arakawa-Schubert (RAS) scheme to examine the impact of the deep convection scheme. This simulation is called CFS T126RAS and is run from 2002 to 2016.

The observational data used in this study comprise NCEP/DOE Reanalysis-2 (R2), CMAP, and daily AVHRR OLR from 1982 to 2002. Calculations for the MJO are based on 20-100-day bandpass filtered anomalies using a Lanczos filter.

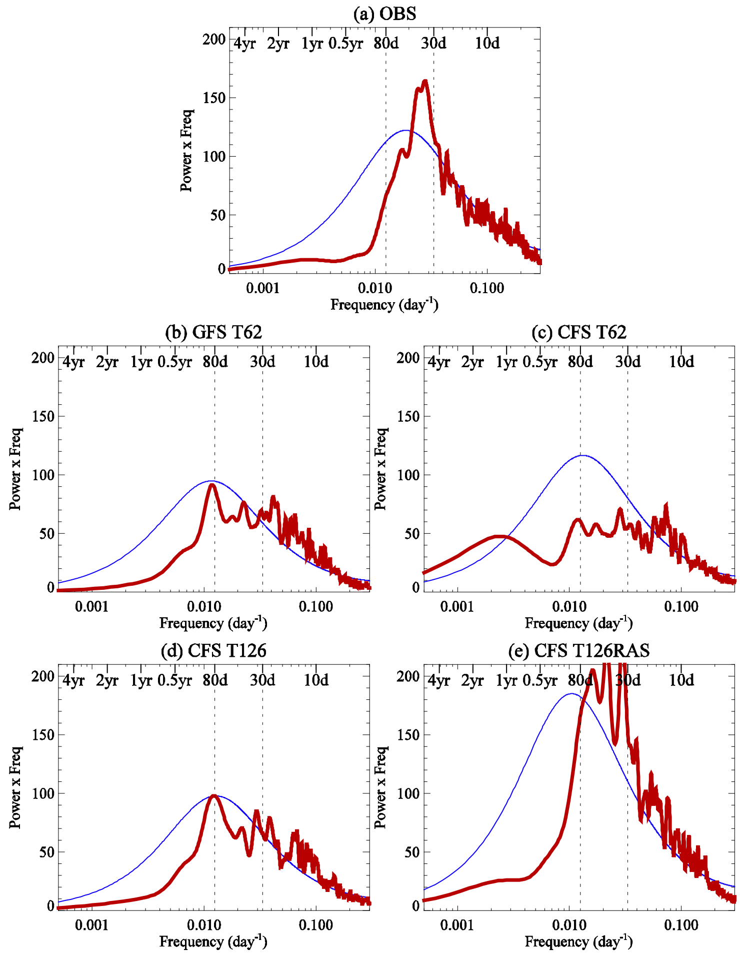

Fig. 1 Power spectra of OLR anomalies averaged over the tropical Indian Ocean area [75°-95°E and 10°S-10°N] for (a) observation, (b) GFS T62, (c) CFS T62, (d) CFS T126, and (e) CFS T126RAS. The thick lines represent the smoothed power. The dashed curve is the upper 95% confidence limit of the red-noise spectrum calculated from a lag 1 autocorrelation. The smoothed spectra are calculated from the Parzen window having an effective bandwidth of 2.5×10^{-3} cpd (cycles per day). For clarity, 30- and 80-day period lines are denoted as dotted vertical lines.

3. Results

3.1. The MJO

Fig. 1 shows the power spectra of the OLR anomalies averaged over the tropical Indian Ocean area [75°-95°E and 10°S-10°N], where the MJO convection is developed and strengthened. The observed spectrum (Fig. 1a) measured by the smoothed periodogram (thick line) illustrates that a higher power exists in the intraseasonal band of 30-80-day periods with a center around 40-55 days. However, GFS T62, CFS T62 and CFS T126RAS (Figs. 1b, 1c, and 1d) do not show any significant spectral peaks associated with the MJO. In contrast to the model simulations using the SAS cumulus scheme, CFS T126RAS (Fig. 1e) produces statistically significant spectral peaks in the MJO band. Several peaks exist in the 30-80-day band.

Fig. 2 shows the two leading EOF modes of tropical convection-circulation fields. In these simulations (i.e., GFS T62, CFS T62, and CFS T126), the explained variance is more than 35% weaker than the observation. However, the CFS T126RAS run (Figs. 2i and 2j) shows some improved results. In particular, the strength of the MJO convection and circulation is greatly enhanced for both EOF1 and EOF2.

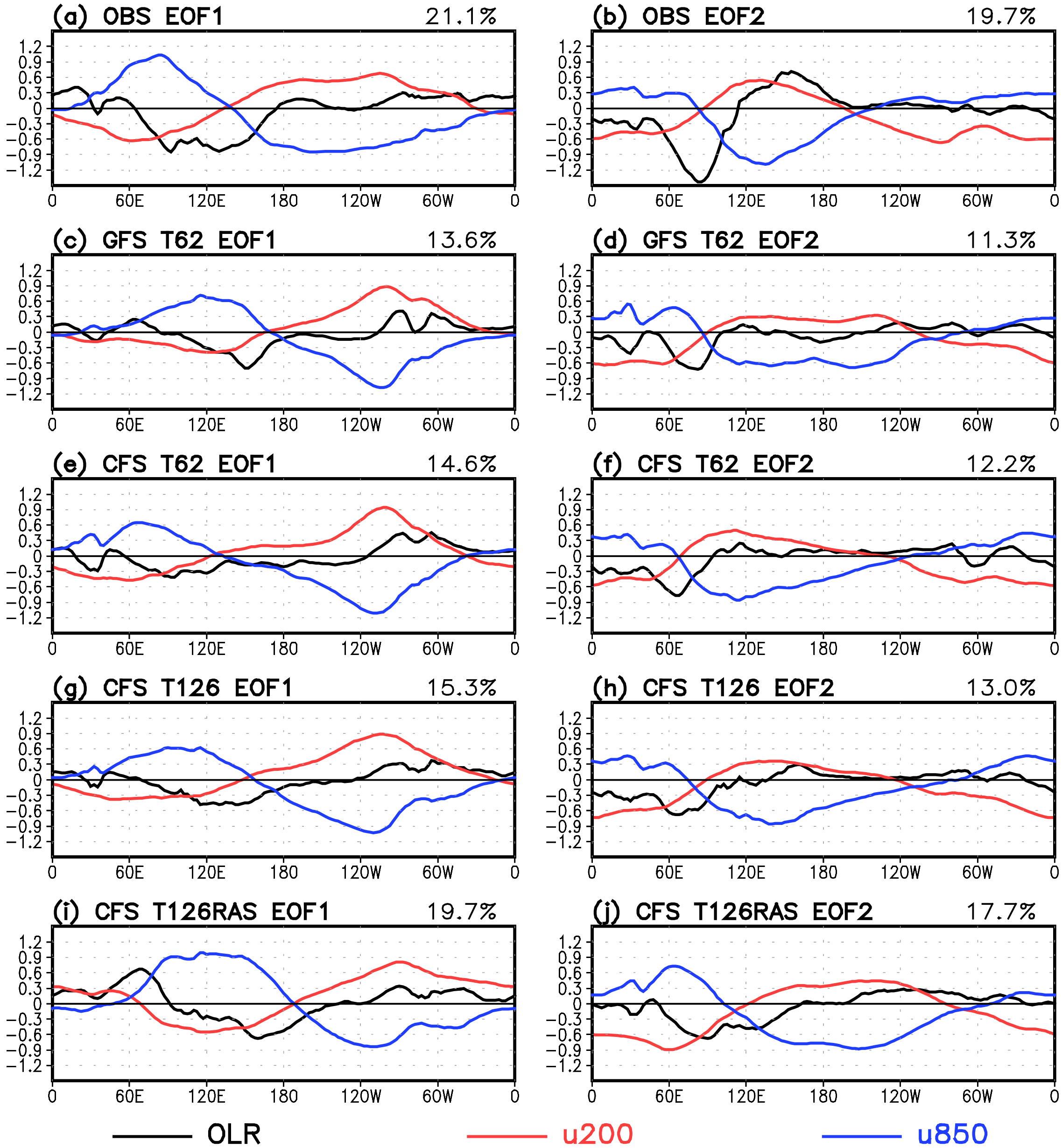

Fig. 2 Spatial structures of combined empirical orthogonal functions (EOFs) of 20-100-day filtered OLR, u850, and u200. EOF1 & EOF2 from (a) and (b) observations, (c) and (d) GFS T62, (e) and (f) CFS T62, (g) and (h) CFS T126 and (i) and (j) CFS T126RAS, respectively. OLR, u850, and u200 are plotted in solid, dashed, and dotted lines, respectively. The percentage value above each panel is the variance explained by each mode and scaled against the observations. All variables are normalized by the averaged value of global variance (9.06 Wm^{-2} for OLR, 1.25 ms^{-1} for u850, and 3.51 ms^{-1} for u200).

Fig. 3 shows the lag correlations between the PC time series of EOF2 (or PC2) and the individual fields (u850, precipitation rate, OLR, surface latent heat flux, downward solar radiation flux, surface temperature, 1000-hP moisture convergence). GFS T62 produces less pronounced precipitation and OLR anomalies (Fig. 3b). Meanwhile, CFS T62 (Fig. 3c) shows a much stronger convection signal and greater spatial coherence between the convection and surface fluxes, and SST over the Indian Ocean. The CFS T126 run (Fig. 3d) exhibits basically the same features as CFS T62 with the strong "propagation barrier" appearing over the Maritime Continent and western Pacific. This propagation barrier has also been noticed in forecast data (Seo et al. 2005) and even a CFS T62 simulation with flux adjustment (Seo et al. 2007). By contrast, CFS T126RAS exhibits much improved propagation characteristics (Fig. 3e). The MJO convection signal (shown as precipitation and OLR anomalies) is very vigorous and this tends to penetrate into the Maritime Continent and western Pacific.

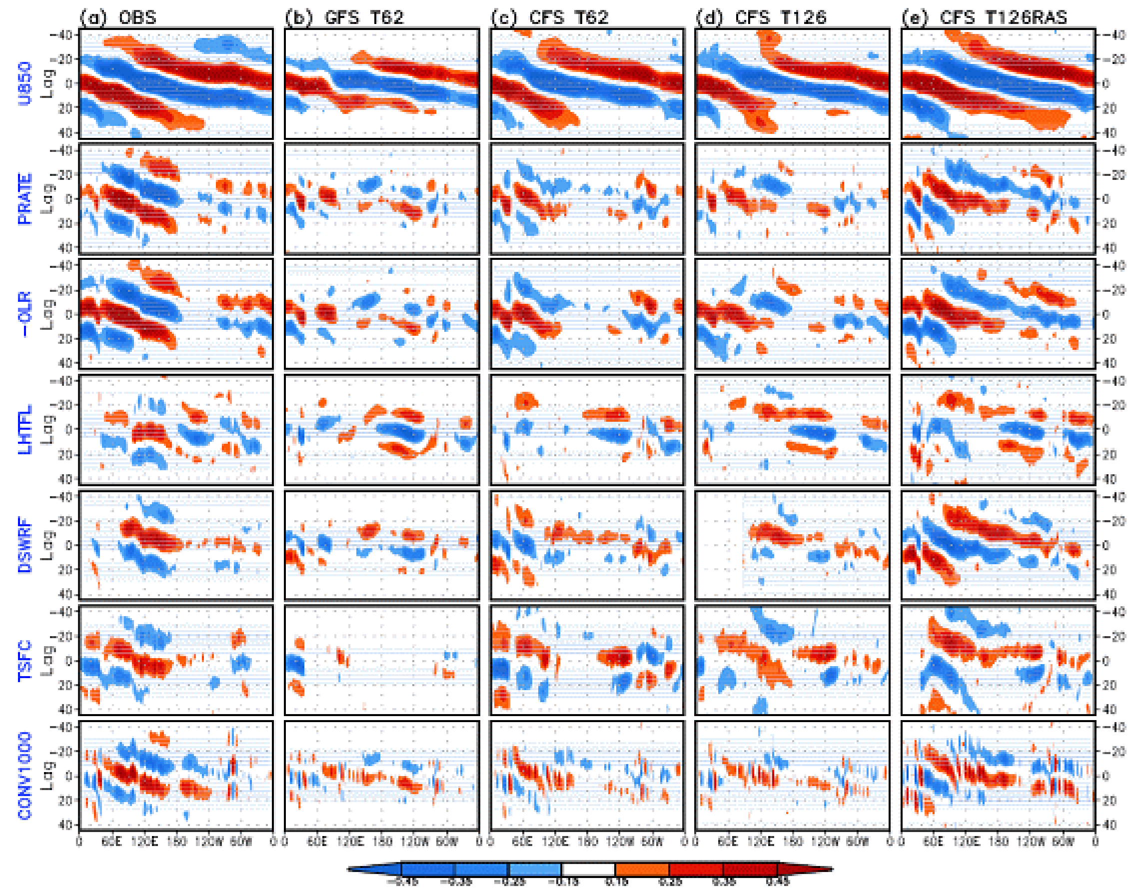

Fig. 3 Lag correlation coefficient between PC2 and u850, precipitation rate, OLR, surface downward solar radiation flux, downward latent heat flux, surface temperature, and 1000-hPa moisture convergence for (a) observations, (b) GFS T62, (c) CFS T62, (d) CFS T126, and (e) CFS T126RAS. The moisture convergence is defined as $-\nabla \cdot (\boldsymbol{V}q)$, where $\boldsymbol{V}$ is the velocity vector and q is the specific humidity. Only statistically significant regions at the 95% level are shaded.

3.2. Factors for the MJO simulation

Only CFS T126RAS has demonstrated a capability to simulate the correct MJO. This section presents the important factors for successfully simulating the MJO.

(a) Air-sea interaction: The air-sea coupling improves the coherence between convection and circulation and other surface fields (Fig. 3).

(b) Model horizontal resolution: The current CFS model runs demonstrate that an increase in the resolution from T62 (which corresponds to ~209 km) to T126 (~105 km) does not help improve the MJO simulation; however, a higher model resolution than T126 remains to be tested.

(c) Basic-state vertical easterly wind shear: Zhang and Geller (1994) showed that vertical easterly shear favors eastward propagating waves. Fig. 4 shows the annual mean vertical easterly shear (u200-u850) over the Maritime Continent and the western Pacific (120°-170°E, 7.5°S-7.5°N) for the observation and model simulations. The vertical wind shear in CFS T126RAS is less than one third that of the observation. These results imply that the background vertical easterly wind shear does not play a major role in the MJO simulation.

(d) Basic-state easterly low-level zonal wind along the tropics: Fig. 5 shows the annual mean zonal wind at 850 hPa in the observation and simulations. Westerlies or weak easterlies are observed over the tropical Indian Ocean, Maritime Continent and western Pacific (Fig. 5a), where the major development and propagation occur. Although the easterly bias in CFS T125RAS (Fig. 5d) is slightly decreased over the Maritime Continent and far western Pacific Ocean compared to the other CFS simulations, the westerlies remain weak over the central-eastern Indian Ocean and the easterly wind prevails over the Maritime Continent. These suggest that the basic-state easterly bias along the tropics may not be a major factor for the MJO simulation.

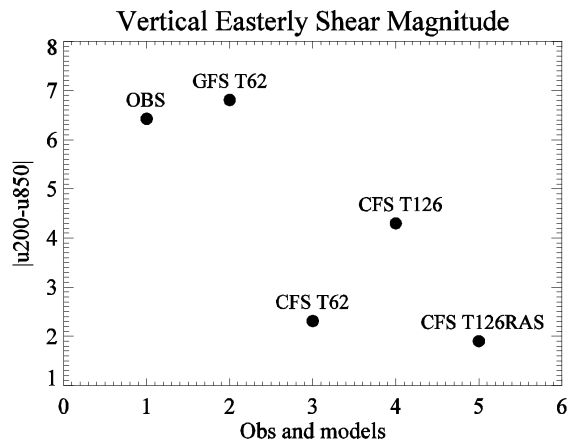

Fig. 4 Annual mean vertical zonal wind shear (u200-u850) for observations and model runs. All values represent easterly shear but these are converted to positive values.

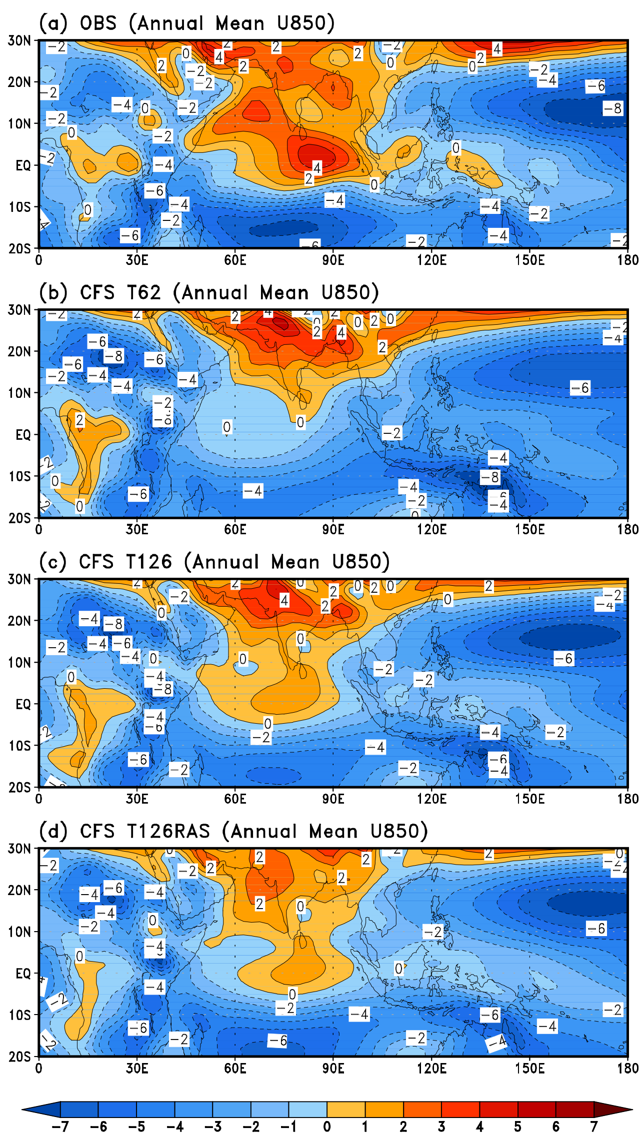

Fig. 5 Annual mean zonal wind at 850 hPa for (a) observation, (b) CFS T62, (c) CFS T126, and (d) CFS T126RAS. The westerly regions are shaded.

(e) SST: The SST bias, defined as model SST minus observed SST, is presented in Fig. 6 for the coupled simulations. A warm bias of ~0.5-1.0 °C appears over the western Indian Ocean, while a cold bias prevails over the eastern Indian Ocean and the western Pacific. CFS T126RAS shows that even if a cold bias exists over the tropical western Pacific, the MJO eastward propagation is greatly enhanced (Fig. 6c). In combination, these results suggest that in the absence of a huge SST bias, other factors may be more effective.

(f) Deep convection parameterization: The current analysis demonstrates that an apparent improvement when the NCEP coupled model utilizes the RAS scheme for cumulus parameterization. The active convective activity along the tropics over the warm pools in this model enhances the lower-level circulation, which in turn helps maintain the MJO convection. The positive feedback between the convection and circulation induces the continued eastward propagation across the Maritime Continent.

(g) Lower-level moisture convergence: To explicitly display the relationship between the MJO convection and lower-level moisture convergence in the CMIP runs, the correlation coefficients presented in Fig. 3 are averaged over the Indian Ocean and the western Pacific regions (Fig. 7). In both regions, enhanced convection follows the moisture convergence with a ~2-5-day lag (Fig. 7a). CFS T126 shows a weak moisture convergence signal, which is about half of the observed convergence (Fig. 7b). However, the CFS T126RAS run (Fig. 7c) has a stronger moisture convergence that leads the enhanced convection by ~2-5 days, which is similar to the observations. The phasing and magnitude of the lower-level moisture convergence is a key factor for the development and propagation of the MJO and only the persistent interaction between the MJO convection and circulation waves ensures the MJO maintenance.

3.3. *Global response to tropical heating of the MJO*

To examine the global circulation patterns induced by MJO convective forcing, OLR and 200-hPa streamfunction anomalies are regressed onto PC1 and PC2. To represent the circulation response to the strong enhanced or suppressed MJO convection events, the regression is performed with respect to a deviation of

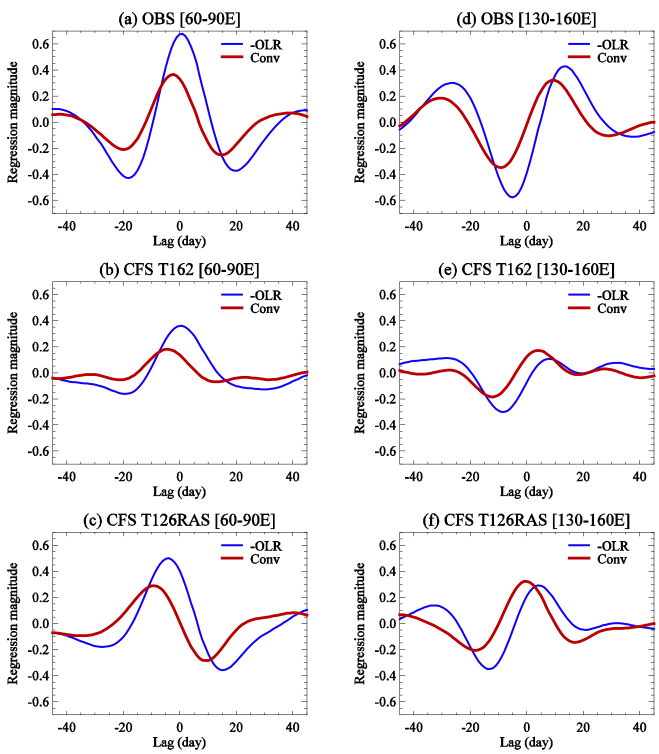

Fig. 7 Relationship between OLR and surface moisture convergence averaged over [60-90°E, 10°S-10°N] for (a) observations, (b) CFS T126, and (c) CFS T126RAS, and averaged over [130-160°E, 10°S-10°N] for (d) observations, (e) CFS T126, and (f) CFS T126RAS.

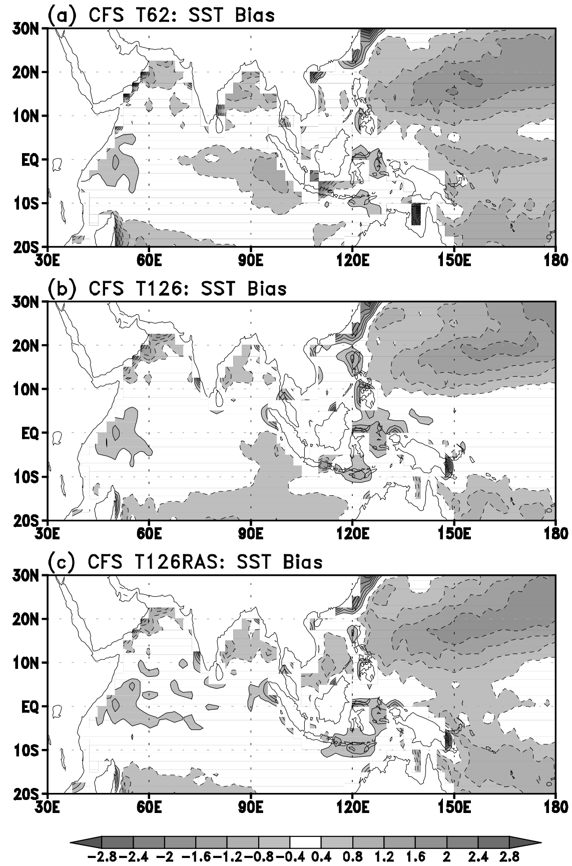

Fig. 6 Annual mean SST bias for (a) CFS T62, (b) CFS T126, and (c) CFS T126RAS.

PC1=2 and PC2=2, as in Matthews et al. (2004). Fig. 8 shows the regression maps of the observed wintertime (November through March) OLR and streamfunction anomalies at 6-day intervals. An anticyclonic (cyclonic) flow couplet off the equator is located to the west of or collocated with the enhanced (suppressed, respectively) convection anomalies, and the westerly (easterly) anomalies along the equator appear to the east of the enhanced (suppressed) convection. This is indicative of a Rossby-Kelvin wave response to the MJO heating (e.g., Matthews 2000; Seo and Kim 2003). At t=0 and t=6, a westward retraction of the east Asian jet appears along ~30°N and the Pacific-North American (PNA)-like wave pattern is formed. Over the eastern Pacific, the Rossby wave propagation to the southern hemisphere through the westerly duct (Hoskins and Ambrizzi 1993) is seen from t=0 to t=12. A weak wave train in the southern hemisphere emanates from the Indian Ocean through the east of the date line, as shown at t=0 (Fig. 8a) and more clearly at t=6 (Fig. 8b).

Figs. 9 and 10 represent the corresponding circulation response to the intraseasonal tropical heating in CFS T126 and CFS T126RAS. The convective anomalies in the CFS T126 simulation are much weaker than those in the observations, and thus the streamfunction anomalies are also weak. Meanwhile, CFS T126RAS (Fig. 10) successfully simulates the eastward propagation of the MJO convection. The actual pattern correlation between the regressed streamfunction in CFS T126RAS and the observation ranges from 0.84 to 0.91, which is much higher than the correlation of 0.47-0.78 between CFS T126 and observation. If the MJO convection over the Pacific is better simulated, the simulation of circulation and precipitation variations in the downstream region, including the Americas, will be much improved.

3.4. *Intraseasonal convectively coupled equatorial waves*

Fig. 11 shows the space-time spectra for the observation, and the NCEP CMIP runs. Also plotted are the theoretical dispersion curves corresponding to three equivalent depths of 12, 25 and 50 m. In the spectra of the antisymmetric component (Fig. 11), MRG and EIG modes are dominant and are connected to each other in the wavenumber-frequency space. For the symmetric component of the equatorial waves, the westward moving ER and WIG waves exist while much stronger eastward MJO and Kelvin waves are identified. All these waves are aligned along the equivalent depths in the range of ~25 m (middle phase lines in Fig. 11).

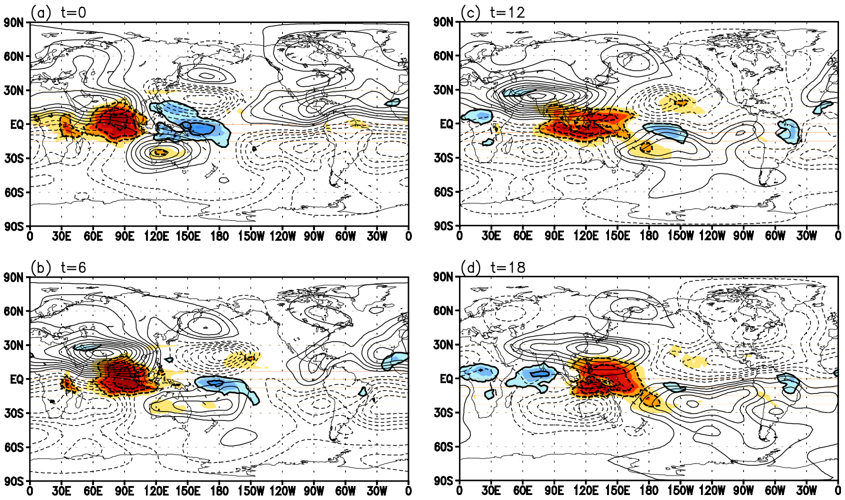

Fig. 8 Regression maps of observed wintertime OLR (shading) and 200-hPa streamfunction (contour) anomalies at 6-day intervals during the first half of the MJO cycle. The regressed magnitude is scaled to a deviation of PC1=2 and PC2=2. OLR is shaded heavily below -10 Wm^{-2} and lightly above 10 Wm^{-2}, with contour intervals of 10 Wm^{-2}. The contour interval of the streamfunction is $1.4 \times 10^6\ m^2s^{-2}$. The zero contour line is suppressed. The contoured streamfunction anomalies are approximately significant at the 95% confidence level.

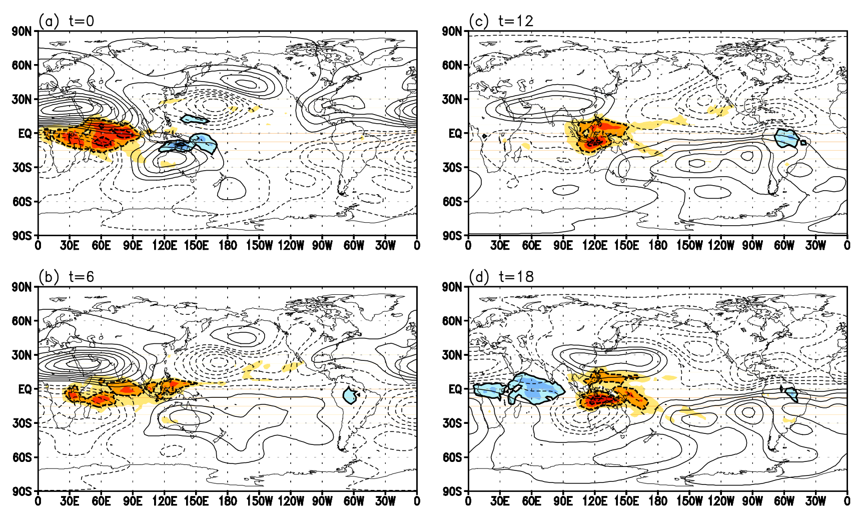

Fig. 9 As in Fig. 8 except for CFS T126.

Figs. 12 and 13 show the space-time spectra of CFS T126 and CFS T126RAS, respectively. In these model runs, statistically significant peaks associated with MRG and EIG waves are not generated. Moreover, all models tend to produce too excessive synoptic scale variability associated with the westward disturbances with periods less than 5 days in the symmetric component of the OLR spectra. CFS T126RAS reveals the strongest power for Kelvin waves among all models. The isolated spectral peaks appear only in CFS T126RAS.

4. Conclusions

This study shows that the interactive air-sea coupling greatly improves the coherence between convection, circulation and other surface fields. A higher horizontal resolution run (CFS T126) does not show any significant improvements in the intensity and structure. In fact, GFS T62, CFS T62, and CFS T126 all yield weaker 30-60-day variances that are not statistically distinguishable from the background red noise spectrum. Their eastward propagation is stalled at the "barrier" over the Maritime Continent and far western Pacific, which is similarly to that in many other climate models. In contrast to the model simulations using the SAS cumulus scheme, CFS T126RAS produces statistically significant spectral peaks in the MJO spectral band and the strength of MJO convection and circulation is greatly improved. Most of all, the ability of the MJO convection signal to penetrate into the Maritime Continent and western Pacific is demonstrated. Especially, the surface moisture convergence signal in this model is comparable to the observation and propagates across the Maritime Continent region. The moisture convergence is located persistently to the east of the enhanced convection and induces the frictional convergence mechanism. Furthermore, this study demonstrates that the improved MJO simulation in CFS T126RAS improves the simulation of extratropical circulation anomalies and hence can extend the predictability over Asia and North America.

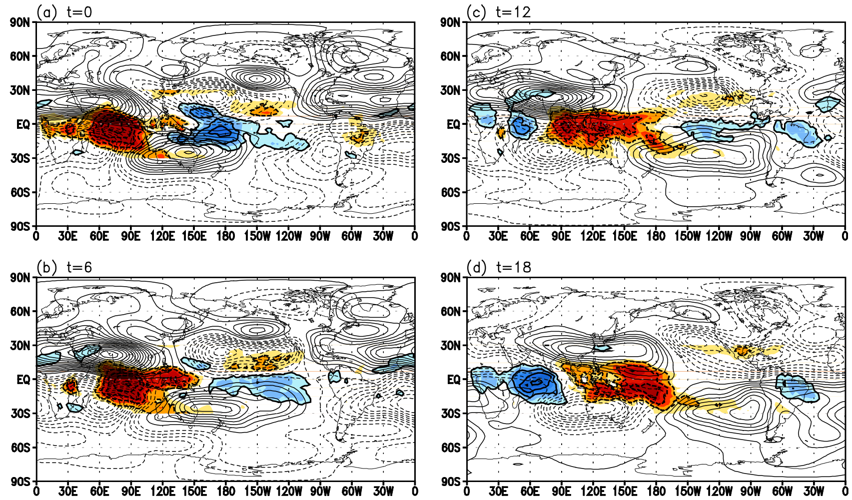

Fig.10 As in Fig. 8 except for CFS T126RAS.

At least in this study, the deep convection scheme, convection-circulation interaction, and frictional moisture convergence are found to be more important. More active convective activity along the tropics in the CFS T126RAS model enhances lower-level circulation and moisture convergence to the east of the enhanced convection, which in turn feeds back to the expansion of the MJO convective entities to the east. The persistence interaction between the convection and circulation gives rise to the continued eastward propagation across the Maritime Continent.

References

Fu, X., B. Yang, G. Bao., and B. Wang, 2008: Sea surface temperature feedback extends the predictability of tropical intraseasonal oscillation. *Mon. Wea. Rev.* **136**, 577-597.

Hendon, H. H., 2000: Impact of air-sea coupling on the Madden-Julian Oscillation in a general circulation model. *J. Atmos. Sci.*, **57**, 3939-3952.

Hoskins, B. J., and T. Ambrizzi, 1993: Rossby wave propagation on a realistic longitudinally varying flow. *J. Atmos. Sci.*, **50**, 1661-1671.

Inness, P. M., and J. M. Slingo, 2003; Simulation of the Madden-Julian Oscillation in a coupled general circulation model. Part II: The role of the basic state. *J. Climate*, **16**, 365-382.

Inness, P. M., J. M. Slingo, E. Guilyardi, and J. Cole, 2003: Simulation of the Madden-Julian Oscillation in a coupled general circulation model. Part I: Comparisons with observations and an atmosphere-only GCM. *J. Climate*, **16**, 345-364.

Lin, J.-L., and Coauthors, 2006: Tropical intraseasonal variability in 14 IPCC AR4 climate models. Part I: Convective signals. *J. Climate*, **16**, 2665-2690.

Maloney, E. D., and D. L. Hartmann, 1998: Frictional moisture convergence in a composite life cycle of the Madden-Julian Oscillation. *J. Climate*, **11**, 2387-2403.

Matsuno, T., 1966: Quasi-geostrophic motions in the equatorial area. *J. Meteor. Soc. Japan*, **44**, 25-43.

Matthews, A. J., 2000: Propagation mechanisms for Madden-Julian oscillation. *Quart. J. Roy. Meteor. Soc.*, **126**, 2637– 2651.

Matthews, A. J., B. J. Hoskins, and M. Masutani, 2004: The global response to tropical heating in the Madden-Julian oscillation during the northern winter. *Quart. J. Roy. Meteor. Soc.*, **130**, 1911-2011.

Seo, K.-H., and K.-Y. Kim, 2003: Propagation and initiation mechanisms of the Madden-Julian oscillation. *J. Geophys. Res.*, **108**, 4384-4405.

Seo, K.-H., J.-K. Schemm, C. Jones, and S. Moorthi, 2005: Forecast skill of the tropical intraseasonal oscillation in the NCEP GFS dynamical extended range forecasts. *Climate Dyn.*, **25**, 265-284.

Seo, K.-H., J.-K. E. Schemm, W. Wang, and A. Kumar, 2007: The boreal summer intraseasonal oscillation simulated in the NCEP Climate Forecast System (CFS): The effect of sea surface temperature. *Mon. Wea. Rev.*, **135**, 1807-1827.

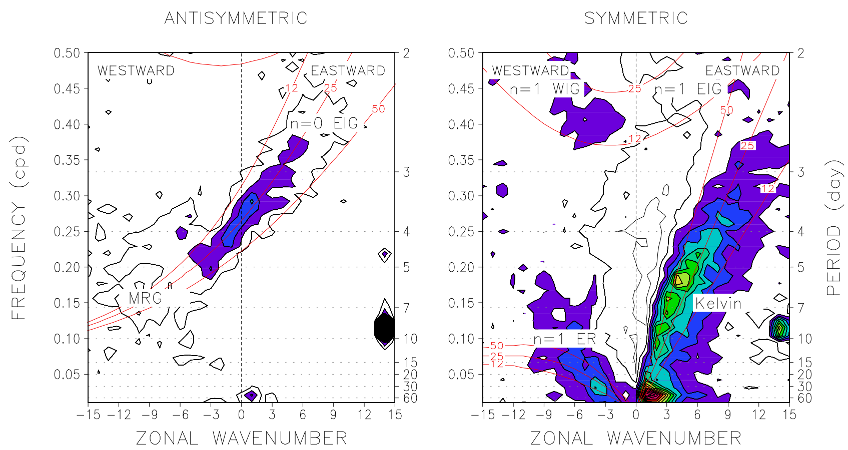

Fig. 11 Space-time spectra of tropically averaged OLR anomalies for observation. The dispersion curves of the equatorial waves are superimposed for the three equivalent depths of 12, 25, and 50 m.

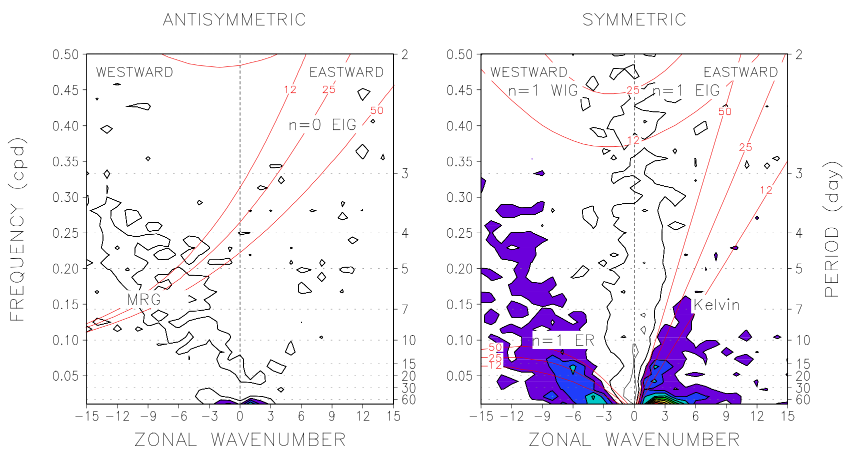

Fig. 12 As in Fig. 11 except for CFS T126.

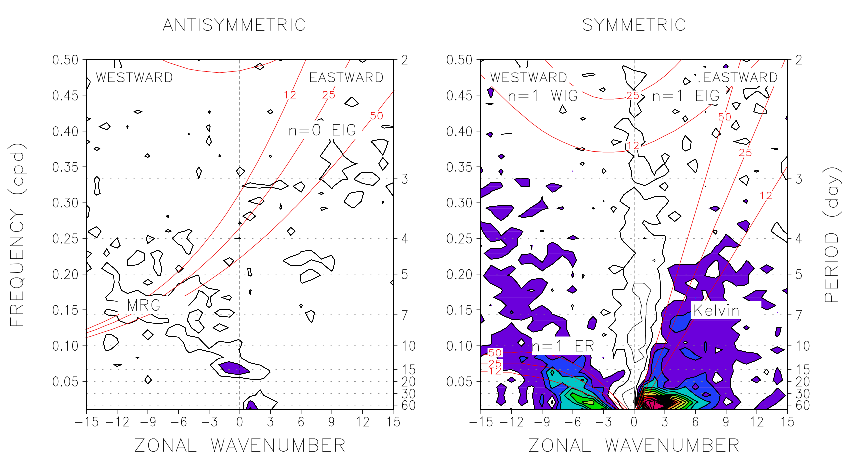

Fig. 13 As in Fig. 11 except for CFS T126RAS.

Waliser, D. E., K. E. Lau, and J. H. Kim, 1999: The influence of coupled sea surface temperatures on the Madden-Julian Oscillation: A model perturbation experiment. *J. Atmos. Sci*., **56**, 333-358.

Wheeler, M., and G. N. Kiladis, 1999: Convectively coupled equatorial waves: Analysis of clouds and temperature in the wavenumber-frequency domain. *J. Atmos. Sci.*, **56**, 374-399.

Science and Technology Infusion Climate Bulletin
NOAA's National Weather Service
33rd NOAA Annual Climate Diagnostics and Prediction Workshop
Lincoln, NE, 20-24 October 2008

Intensification of Summer Rainfall Variability in the Southeastern United States in Recent Decades

Hui Wang[1], Rong Fu[2] and Wenhong Li[3]

[1]NOAA Climate Prediction Center
[2]University of Texas at Austin
[3]Georgia Institute of Technology

1. Introduction

The Southeastern United States is one of the fastest growing regions in the nation. Water supplies in this area are increasingly stressed especially during summer. The year-to-year fluctuations in summer rainfall over the Southeast thus have vital influence on regional hydrology, agriculture, and related industries. In the past three decades, summer droughts repeatedly struck the Southeast and had a devastating impact on this region socially and economically. For example, the 1986 Southeast summer drought caused billions of dollars of damage in agriculture. The 2007 drought, the most recent one, ranked as the worst in 100 years and pushed water shortages to a crisis point.

The recurrence of these severe droughts raises a question as to whether the magnitudes of anomalous rainfall, especially droughts, in the Southeast have been intensified in recent decades. If so, what might have caused such intensification? This study aims to characterize the change in summer rainfall variability in the Southeast and to explore possible causes of the shift of rainfall variability. In this report, we will present observational evidence that the intensification of Southeast summer rainfall variability closely ties to the variation of tropical Atlantic sea surface temperature (SST). The strong co-variability between the rainfall and SST also suggests some predictability of Southeast summer precipitation based on the tropical SST.

2. Data and method

The data used in this study consist of precipitation, atmospheric wind field, and SST from 1948 to 2007. Summer seasonal mean precipitation is an average of June, July and August (JJA) monthly rainfall. The precipitation data are taken from the NOAA Climate Prediction Center (CPC) U.S. Unified Precipitation for 1948–98 and from the realtime U.S. Daily Precipitation Analysis for 1999–2007. The atmospheric winds are the NCEP–NACR Reanalysis product (Kalnay et al. 1996). The SSTs are the NOAA Extended Reconstructed SST (ERSST v3, Smith et al. 2008).

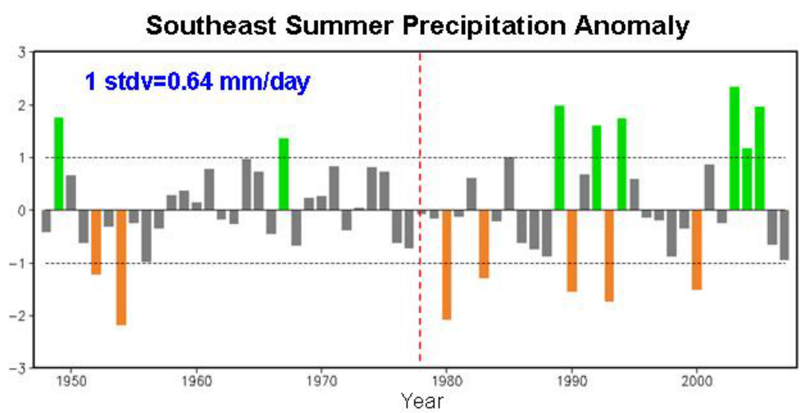

Fig. 1. Normalized time series of June–August mean precipitation anomalies averaged over the Southeastern United States (25N–36.5N, 76W–91W). Color bars indicate the summers with rainfall anomalies exceeding one standard deviation.

The relationship between the Southeast summer precipitation and tropical SST is examined by using the singular value decomposition (SVD; Bretherton et al. 1992). This statistical technique is able to objectively identify pairs of spatial patterns with the maximum temporal covariance between precipitation and SST (e.g., Ting and Wang 1997).

Correspondence to: Hui Wang, NOAA Climate Prediction Center;
E-mail: Hui.Wang@noaa.gov

3. Variability of Southeast summer rainfall

To examine rainfall variability in the Southeast, a precipitation index is constructed by averaging JJA seasonal mean precipitation anomalies in an area from 76oW to 91oW and from 25oN to 36.5oN. The area covers seven southeastern states, including Alabama, Florida, Georgia, Mississippi, North Carolina, South Carolina, and Tennessee. The normalized index time series for 1948–2007 is shown in Fig. 1, with one standard deviation corresponding to 0.64 mm day-1. The precipitation index displays higher interannual variability with more wet and dry extremes in the second half of the period (1978–2007). In the first 30 years (1948–77), there were four summers with rainfall anomalies exceeding one standard deviation while in the second 30 years, there were 11 summers. The summer precipitation in the second 30 years contributes to the total rainfall variance by 68%, in contrast to 32% in the first 30 years. The change in the rainfall variability is consistent with the shift of rainfall probability distribution in the second period. Composite analysis (not shown) indicates that there were coherent decreases (increases) of rainfall frequency and intensity in dry (wet) summers in the second 30 years. Evidently, the Southeast summer rainfall variability has been intensified in the recent three decades.

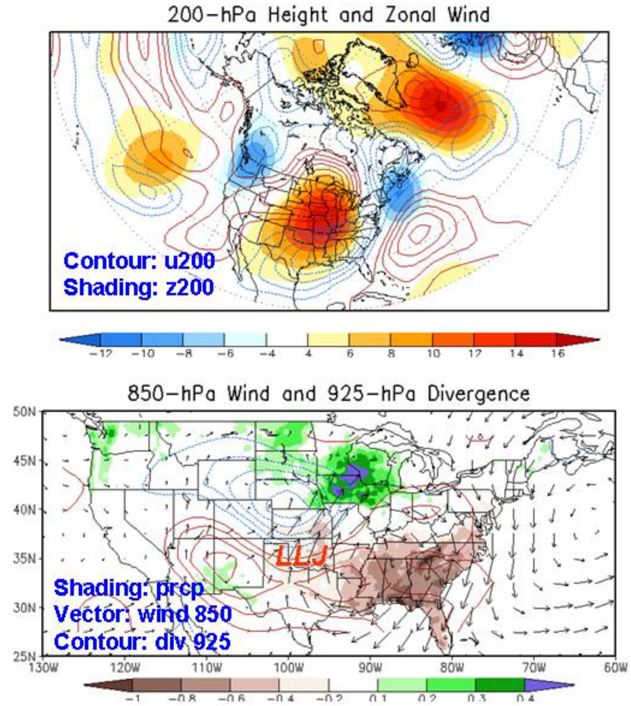

Fig. 2. Composite anomalies of 200-hPa height and zonal wind (upper panel) and 850-hPa wind, 925-hPa divergence and precipitation (low panel) associated with the Southeast summer droughts. The anomalies are obtained with linear regressions vs. the 60-year Southeast summer precipitation index.

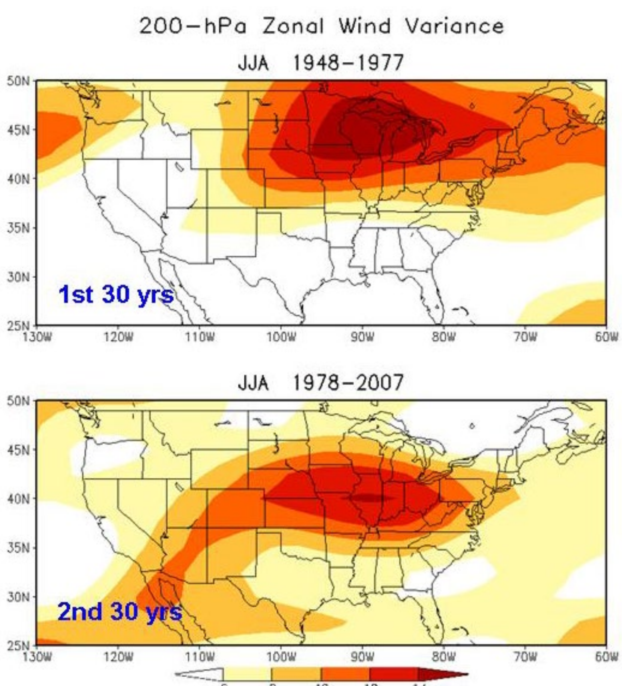

Fig. 3. 200-hPa zonal wind variance for the two 30-year periods.

The Southeast summer precipitation is an important part of the continental-scale warm season rainfall in the United States. As shown in Fig. 2, the drought-related circulation is dominated by positive height anomalies over the Central United States. The upper-level jet stream thus shifts towards the north. In the lower level, the anticyclonic circulation enhances the Great Plains' low-level jet and moisture transport from the Gulf of Mexico to the Midwest, and also causes deficit of moisture flux from the Gulf to the Southeast. The circulation pattern and associated lower-level divergence field are consistent with dry conditions in the Southeast and wet conditions in the Midwest.

The intensification of the summer rainfall variability in the Southeast is accompanied by a change of zonal wind variability at the jet-stream level. Figure 3 shows the 200-hPa zonal wind variance for the two 30-year periods. The center of maximum zonal wind variability experienced a significant southward shift from 45ºN in the early period to 40ºN in the late period.

4. Co-variability with SST

To explore possible links between the Southeast precipitation and Pacific and Atlantic SST, two SVD analyses were performed by analyzing the covariance matrices of summer season U.S. rainfall and SST from each ocean basin. The results are shown in Fig. 4 with homogeneous correlation maps (Wallace et al. 1992). For the Pacific SST, the first SVD mode is characterized by the El Niño SST pattern. The corresponding precipitation displays wet conditions in the Northern Plains and the Midwest and dry conditions in the Southeast. This is the canonical summer precipitation pattern associated with El Niño (e.g., Ting and Wang 1997). For the Atlantic SST, the first mode features warm SST anomalies across the tropical and North Atlantic. These warming anomalies are also correlated with warming anomalies in the Indo-Pacific warm pool. Associated with the Atlantic warming, precipitation in the Southeast and the Southern Plains, especially Texas, is above normal. The second SVD mode of the Atlantic SST closely resembles the Atlantic zonal mode (Zebiak, 1993), with warm SST anomalies along the equator. The associated precipitation pattern shows a large deficit of rainfall in the Southeast.

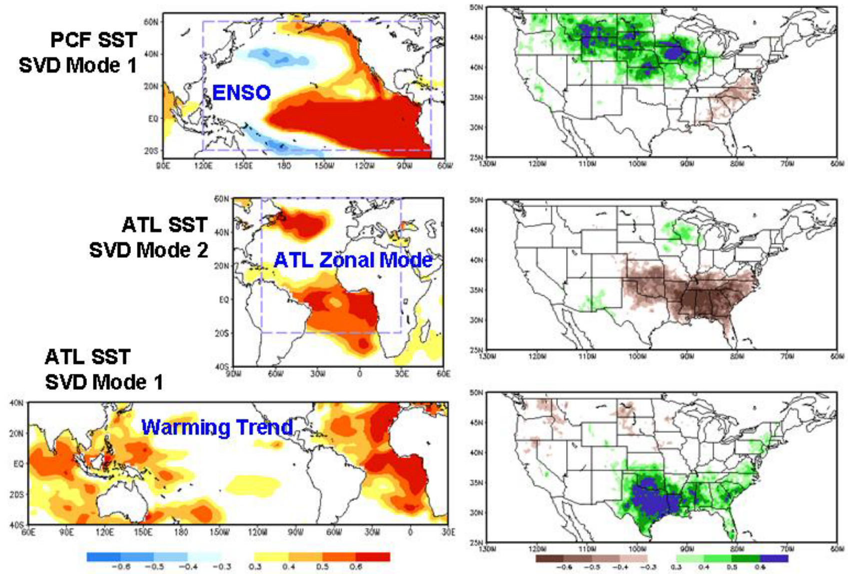

Fig. 4. Homogeneous correlation maps of the first SVD mode of the Pacific SST and U.S. precipitation (top), the first (bottom) and second (middle) SVD modes of the Atlantic SST and U.S. precipitation.

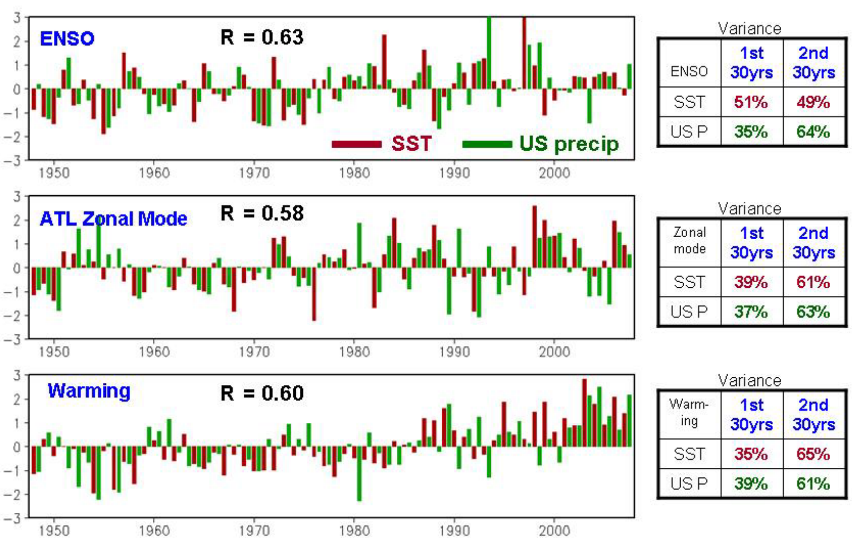

Fig. 5. Times series of the three SVD modes shown in Fig. 4, with the correlation coefficients (R) between each pair of SST and US precipitation time series. The tables on the right side list the percentages of SST and US precipitation variance over the two 30-year periods.

The corresponding time series of each pair of SVD modes are show in Fig. 5, together with the percentages of SST and precipitation variance explained by each mode over the two 30-year periods. The increase of the Atlantic SST variability in the recent 30 years in both the zonal mode and the warming trend is consistent with the increase of the precipitation variability in the same period. Both SVD modes have strong loadings over the Southeast in the precipitation field (Fig. 4). Therefore, the intensification of the Southeast summer rainfall variability is strongly coupled with the higher Atlantic SST variability in the last three decades. This is also supported by the evidence that the changes in the upper-level zonal wind variability associated with the two Atlantic SST modes (Fig. 6) contribute to the observed shift of the zonal wind variability between the two periods (Fig. 3).

The SVD analyses separate the relation of the U.S. precipitation to the Atlantic SST from that of the Pacific SST. How the SST-coupled precipitation contributes to the Southeast rainfall variability is assessed by reconstructing the Southeast precipitation index based on the three SVD precipitation time series. As shown in Fig. 7, the reconstructed total rainfall anomalies well reproduce the observed precipitation variation with a correlation of R=0.92. Among the three SVD modes, the Atlantic zonal mode-related precipitation contributes most to the Southeast rainfall variability (R=0.87). The warming trend also has a significant contribution (R=0.63), whereas the ENSO mode has contributed less (R=0.39). The threshold for the correlation coefficients at the 1% significance level is 0.29 based on the Monte Carol tests.

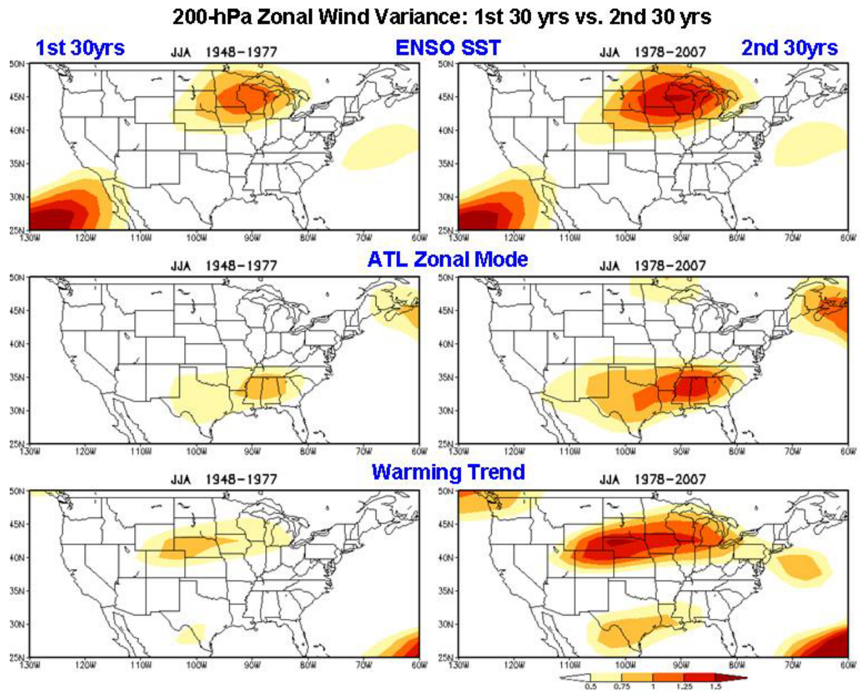

Fig. 6. 200-hPa zonal wind variance for the two 30-year periods reconstructed with each SVD SST time series.

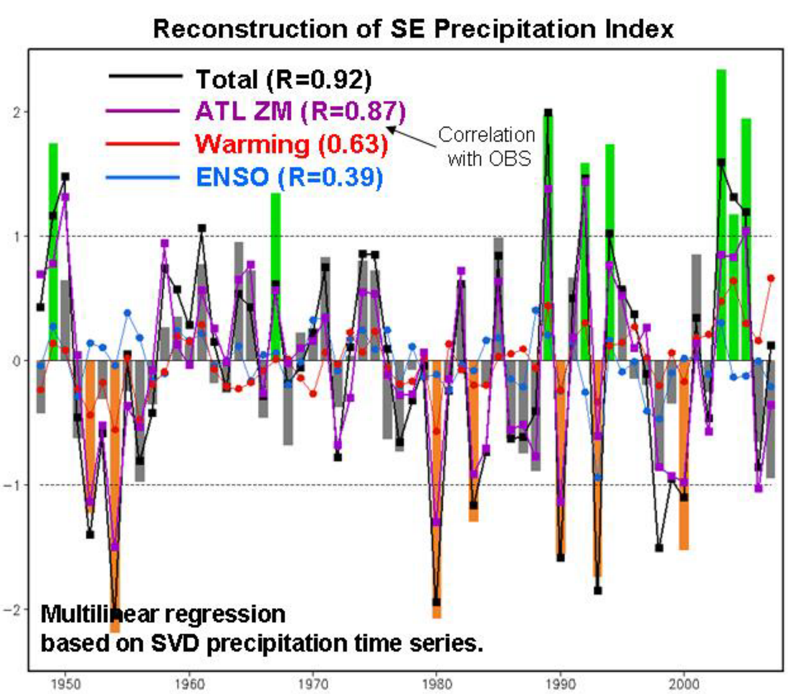

Fig. 7. Reconstructed Southeast summer precipitation index based on the time series of precipitation for the first three SVD modes and multiple linear regressions.

5. Predictability of the Southeast summer precipitation

The results presented in Figs. 4, 5, and 7 suggest that the variability of the Southeast summer precipitation is strongly linked to the Atlantic and Pacific SST. The SST thus possesses potential predictive value for the Southeast summer precipitation. Given Atlantic and Pacific SST patterns, the Southeast precipitation can be predicted based on the relationship depicted by the SVD analyses (Figs. 4 and 5). The empirical forecast system involves three steps. First, seasonal mean SSTs of a target summer, either from observations or from climate model forecasts, are projected onto the SVD SST patterns (Fig. 4) to obtain the SST projection coefficients. The corresponding precipitation projection coefficients are then obtained based on the SVD SST–precipitation relationship (Fig. 5) and a linear regression. Finally, precipitation anomalies are predicted with multiple linear regression coefficients of historical rainfall data vs. the three SVD precipitation time series, multiplied by the precipitation projection coefficients for the target summer. The proposed forecast method is similar to Wang et al. (1999), in which the Pacific SST is the only predictor for U.S. precipitation.

The predictability of the Southeast summer precipitation is evaluated by a cross validation of the hindcasts of summer rainfall for the past 60 years (JJA, 1948–2007) based on the observed SST. Figure 8 shows the anomaly correlation between the hindcasts and observations of JJA U.S. precipitation. Considerable forecast skill is found in the Northern Plains and the Southeast. The former is primarily contributed by the Pacific ENSO mode, whereas the latter is contributed by the Atlantic zonal mode and the warming trend.

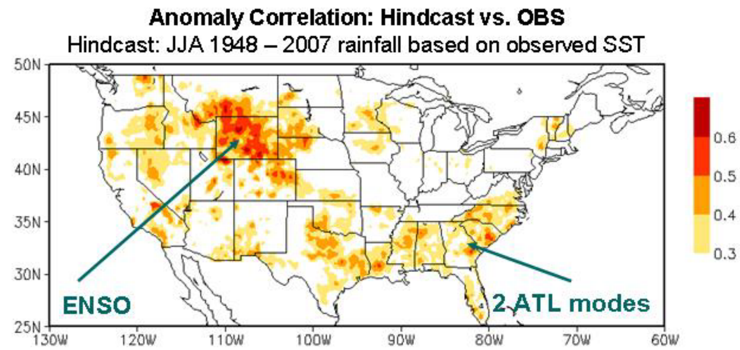

Fig. 8. Anomaly correlation between 60-year hindcasts and observations of summer U.S. precipitation.

6. Summary

Our analysis of 60-year rainfall data reveals that the interannual anomalies of summer precipitation in the Southeast United States have been intensified in recent three decades (1978–2007) compared to the earlier period (1948–77), leading to stronger summer droughts and anomalous wetness. Such intensification of summer rainfall variability is consistent with the shift of daily rainfall probability distribution. It is also accompanied by a southward shift of the region of maximum zonal wind variability at the jet stream level and coupled with higher Atlantic SST variability in the late period. An empirical model for predicting Southeast summer precipitation was developed based on the SVD analyses, which link the Southeast rainfall variability to the Atlantic zonal mode, the SST warming trend, and the Pacific ENSO mode. A cross validation of 60-year hindcasts suggests considerable predictability of the Southeast summer precipitation with tropical SST.

References

Bretherton, C. S., C. Smith, and J. M. Wallace, 1992: An intercomparison of methods for finding coupled pattern in climate data. *J. Climate*, **5,** 541–560.

Kalnay, E., and Coauthors, 1996: The NCEP–NCAR 40-Year Reanalysis Project. *Bull. Amer. Meteor. Soc.*, **77,** 437–471.

Smith, T. M., R. W. Reynolds, T. C. Peterson, and J. Lawrimore, 2008: Improvements to NOAA's historical merged land-ocean surface temperature analysis (1880–2006). *J. Climate*, in press.

Ting, M., and H. Wang, 1997: Summertime U.S. precipitation variability and its relation to Pacific sea surface temperature. *J. Climate*, **10,** 1853–1873.

Wallace, J. M., C. Smith, and C. S. Bretherton, 1992: Singular value decomposition of wintertime sea surface temperature and 500-mb height anomalies. *J. Climate*, **5,** 561–576.

Wang, H., M. Ting, and M. Ji, 1999: Prediction of seasonal mean United States precipitation based on El Nino sea surface temperatures. *Geophys. Res. Lett.*, **26,** 1341–1344.

Zebiak, S. E., 1993: Air-sea interaction in the equatorial Atlantic region. *J. Climate*, **6,** 1567–1586.

2. MONITORING AND PREDICTION

Science and Technology Infusion Climate Bulletin
NOAA's National Weather Service
33rd NOAA Annual Climate Diagnostics and Prediction Workshop
Lincoln, NE, 20-24 October 2008

Climate Prediction Center Global Monsoon Monitoring Activity

Wassila M. Thiaw, Muthuvel Chelliah, Vernon Kousky, Wei Shi, Viviane Silva, and Song Yang
Climate Prediction Center, NOAA/NWS/NCEP

1. Introduction

Global climate fluctuations and their impacts on economic development have been a worldwide concern during the past several decades. The problem is even more acute in emerging countries of Africa, Asia, and Latin America, where alternating severe droughts and floods have been persistent causes of severe economic hardships. To help mitigate the impacts of extreme weather and climate fluctuations requires routine timely and accurate monitoring of the global monsoon to better understand the mechanisms for monsoon variability and to improve forecasts of monsoon at all time scales.

The following are highlights of the NOAA Climate Prediction Center (CPC) global monsoon monitoring activity presented at the Climate Diagnostics and Prediction Workshop in Lincoln, NE, October 2008. In this extended summary, we present the motivation for starting the global monsoon monitoring activity in section 2. In section 3, we present the global monsoon monitoring web site. Applications in climate risk assessments and outreach are presented in sections 4 and 5, respectively. Finally, we discuss future development and challenges in section 6.

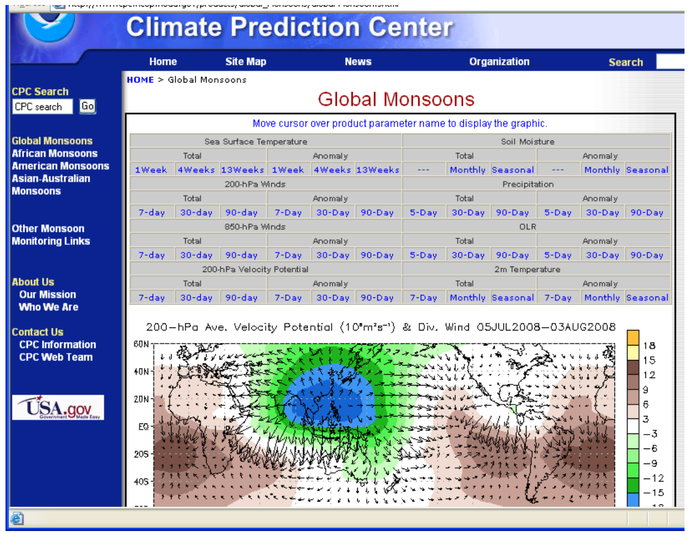

Fig. 1 Global monsoon website and link to regional monsoon websites.

2. Motivation

CPC's position as an international center with expertise in climate forecasting, monitoring, research, and diagnostic studies, along with product dissemination and cooperation with other agencies, makes it a unique source of a wide range of weather and climate products and services tailored to regional decision support systems worldwide. The objective of the global monsoon monitoring activity is to consolidate climate monitoring efforts at CPC to help advance our understanding of the global monsoon systems and to improve forecasts and early warning systems.

3. Global monsoon monitoring web portal

The global monsoon monitoring products are made available to the public through the CPC website: http://www.cpc.noaa.gov/products/Global_Monsoons/Global-Monsoon.shtml. The global monsoon monitoring website features recent anomalies of global scale climate information over the last 90 days, the last 30 days, and the last 7 days (Fig. 1). The parameters featured in the website include: sea surface temperatures, soil moisture, winds at 850 and 200 hPa, velocity potential, precipitation, outgoing longwave radiation, and 2-meter temperature. The global monsoon website is also parent to the regional monsoon websites.

The regional monsoons monitored include the African monsoon, the American monsoon (over North and South Americas), and the Asian-Australian monsoon. Each of the regional monsoon websites features the following:

Correspondence to: Wassila M. Thiaw, Climate Prediction Center, NOAA/NWS/NCEP;
E-mail: Wassila.Thiaw@noaa.gov

- Animation of weekly OLR, 200 hPa streamlines, and 850 hPa winds
- Recent evolutions (last 90, 30, and 7 days) of the following parameters:
    - Precipitation maps and time series (also for the past 180 days)
    - Temperature – 2 meter
    - SST and soil moisture
    - Winds and vertically-integrated water vapor flux
- Weekly monsoon updates in the form of PPT presentations are prepared and posted on the regional monsoon websites every Monday. The content of the regional monsoon presentations include: highlights of precipitation evolution over the last 7 days, spatial maps of total precipitation and anomalies over the last 180, 90, 30, and 7 days (Fig. 2). Also included are precipitation time series featuring the evolution of rainfall over the last 30 or 90 days for selected grid boxes, and 850 hPa and 200 hPa wind anomalies for the last 7 days. Additional information about the monsoon PPT presentations includes the NCEP global forecasts, week-1 and week-2 outlooks for the regional monsoons, and summary reports to describe the evolution of the monsoons. Seasonal monsoon summaries and annual reports have been or will be posted to the websites in the near future.

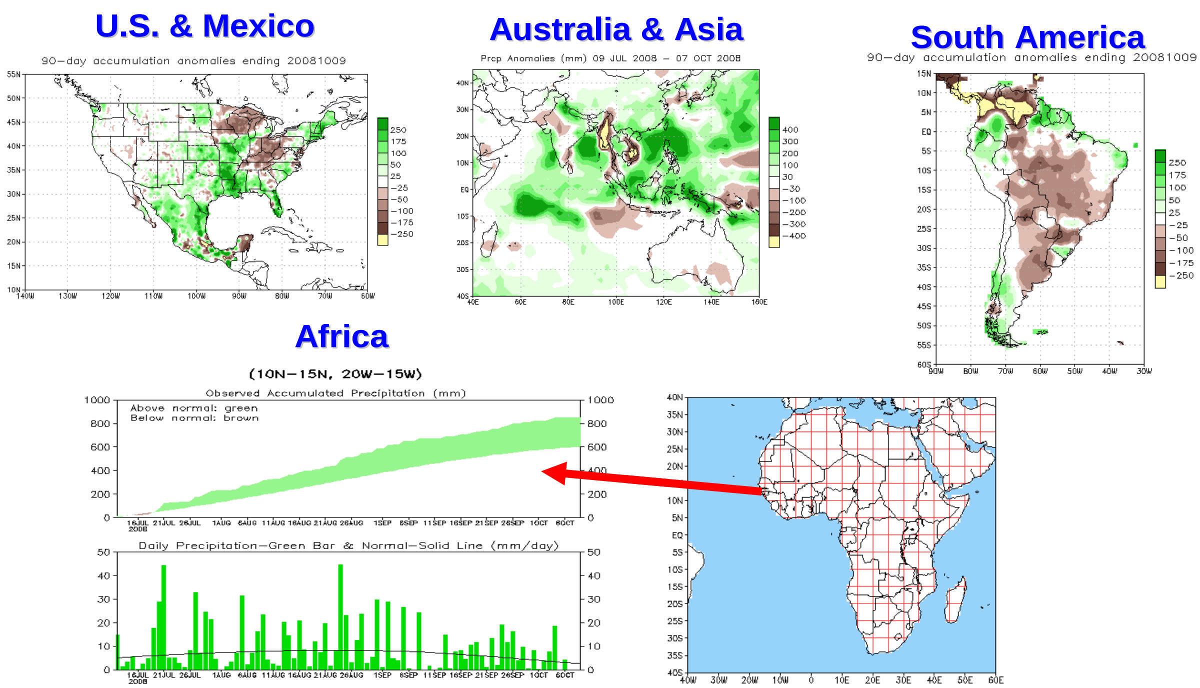

Fig. 2 Ninety-day precipitation anomalies for the period 11 Jul – 9 Oct 2008 and 9 Jul – 7 Oct for the North American and South American monsoons, and the Asian-Australian monsoon, respectively. Daily precipitation time series for a grid box in West Africa for the period 11 Jul – 9 Oct 2008.

4. Global and regional climate risk assessments

The global monsoon monitoring products are direct input into the CPC US and global hazard assessments and the African regional climate risk assessments. The purpose is to provide emergency managers, planners, and the public advanced notice of potential hazards related to climate, weather, and hydrological events. The global tropical benefits/hazards (GTH) assessments are produced in collaboration with other NOAA centers including the Earth System Research Laboratory, the National Hurricane Center, and selected National Weather Service Weather Forecast Offices. In addition to the use of global monsoon monitoring products, the GTH synthesizes information and expert analysis from other CPC operational and routine monitoring products. The African weather and climate risk assessments are produced weekly in collaboration with the US Agency for International Development (USAID) project, Famine Early Warning System (FEWSNET), including the USGS, NASA, and Chemonics. The objective is to assist USAID to develop mitigation strategies to help FEWSNET countries cope with food security vulnerability induced by extreme weather and climate events. The assessments are based on a wide range of products, including rain gauge data, satellite rainfall estimates (RFE), rainfall forecasts out to 7 and 14 days. Other inputs include river flow forecasts from the USGS, normalized difference vegetation index (NDVI), and field observations.

5. Domestic and international outreach

There is a strong demand for the global monsoon monitoring products. Weekly monsoon PPT updates are distributed to a list of 400 people. Potential users of the information in the US are: National Weather Forecasting Offices (WFOs), especially the southwestern region, NWS Climate Service Division, and the National Hurricane Center for early detection of Atlantic tropical storm activity operational meteorological services around the globe. Users also include National Meteorological and Hydrological Services around the world, government and academic institutions with interest on monsoons. Some of the global monsoon products are tailored to meet the US Agency for International Development (USAID) climate requirements to support Famine Early Warnings Systems Network (FEWSNET) activities for humanitarian assistance in Africa, Afghanistan, and Central America. The products can also be used in the Asian flood network project with USAID Office of Foreign Disaster Assistance (OFDA) focusing on the Mekong river Basin.

6. Future development

The global monsoon monitoring effort at CPC started in 2006 and it has provided a unique opportunity for advanced understanding of the global monsoon systems and how the information can be used to improve climate services. The CPC Global monsoon team is working towards improving the quality of the monitoring products and tailoring the information to meet user demands. In particular, in the near future, the team plans to work with research institutions to develop monsoon indices to better track the onset and demise of the monsoons as well as dry and wet spells in all monsoon regions. The team also plans to develop a seasonal and week-1 and week-2 forecast forums for all the regions. The challenges that the monsoon team faces include the limited predictability on both subseasonal and seasonal time scales, limited resources for research at CPC, and sometimes inconsistency in the precipitations data sets. The Global monsoon team will work to meet those challenges by reaching out to the research community and by engaging national meteorological services around the world to provide the data that is required to enhance the quality of the monsoon products.

Global Monsoon Team Members

Global Monsoon Team Lead:	Song Yang
Regional Monsoon Group Leads:	
Africa	Wassila Thiaw
Asia-Australia	Muthuvel Chelliah
North America	Wei Shi
South America	Viviane Silva

Other Global Monsoon Team Members: Yun Fan, Jon Gottschalck, Wayne Higgins, Vernon Kousky, Vadlamani Kumar, Kingtse Mo, Jae Schemm, Wanqiu Wang, Pingping Xie, Soo-Hyun Yoom, and Qin Zhang

Science and Technology Infusion Climate Bulletin
NOAA's National Weather Service
33rd NOAA Annual Climate Diagnostics and Prediction Workshop
Lincoln, NE, 20-24 October 2008

Atlantic Basin Seasonal Hurricane Prediction from 1 December

Philip Klotzbach
Department of Atmospheric Science, Colorado State University

1. Introduction

The Tropical Meteorology Project (TMP) at Colorado State University (CSU) has been issuing Atlantic basin seasonal hurricane forecasts in early June with an update in early August since 1984 (Gray 1984b). CSU's seasonal hurricane forecast scheme has shown significant real-time skill for the early June and early August predictions (Owens and Landsea 2003). Additional research in the late 1980s and early 1990s led to the development of an early December forecast (Gray et al. 1992) that utilized West African rainfall and the quasi-biennial oscillation (QBO) as predictors. These predictors, when used in combination, explained about 50% of the cross-validated variance for the following year's hurricane season, based on data from 1950-1990. However, these predictors did not show real-time forecast skill.

More recently, Klotzbach and Gray (2004) developed a new December statistical hindcast scheme utilizing National Centers for Environmental Prediction/National Center for Atmospheric Research (NCEP/NCAR) reanalysis data (Kistler et al. 2001). This newer prediction scheme utilized a total of six predictors and attempted to hindcast several forecast metrics including named storms, named storm days, major hurricanes and Net Tropical Cyclone (NTC) activity (Gray et al. 1994). Although this scheme also showed considerable amounts of hindcast skill, it did not show real-time forecast skill from 2003-2007. Real-time predictions of Net Tropical Cyclone activity issued in early December have shown little correlation ($r = 0.05$) with observations over the period from 1992-2007.

Additional revisions to the early December forecast scheme have recently been made. These revisions involve simplifying the statistical scheme and including more robust statistical tests for predictor significance, similar to what was done in Klotzbach (2007). More extensive discussion of the new December forecast scheme can be found in a recently published paper (Klotzbach 2008). The remainder of the paper is structured as follows. Section 2 discusses the data that is used in the study. Section 3 describes the methodology utilized to obtain the predictors. Section 4 demonstrates the hindcast skill available when implementing the forecast scheme. Section 5 discusses the physical relationships between predictors and Atlantic basin hurricane activity, while Section 6 examines the application of this prediction scheme to United States landfalling hurricanes. Section 7 concludes and provides some ideas for future work.

2. Data

Atlantic basin tropical cyclone statistics from 1950-2007 were calculated from the "best track" dataset generated by the National Hurricane Center (Jarvinen et al. 1984). From the "best track" dataset, an index of Net Tropical Cyclone activity (NTC) was created. NTC was introduced by Gray et al. (1994) and is defined to be the following six parameters normalized by their 1950-2000 average values: named storms, named storm days, hurricanes, hurricane days, major hurricanes and major hurricane days. NTC is the only metric predicted by this new forecast scheme, in an effort to develop a simpler scheme that utilizes fewer predictors than when multiple indices are forecast (i.e., named storms, hurricanes, major hurricane days, etc.). A small downward adjustment to the "best track" is applied prior to 1970 (Landsea et al. 1993). The National Centers for Environmental Prediction/National Center for Atmospheric Research (NCEP/NCAR) reanalysis (Kistler et al. 2001) was utilized as the source of large-scale atmosphere/ocean data.

3. Predictor Selection Methodology

Predictors were selected from the NCEP/NCAR reanalysis. First, a time series of Atlantic basin NTC was created for 1950-2007. Then, NCEP/NCAR reanalysis fields of sea level pressure, sea surface

Correspondence to: Philip Klotzbach, Department of Atmospheric Science, Colorado State University;
E-mail: philk@atmos.colostate.edu

temperature and 500 mb geopotential height were correlated against the NTC index from 1950-1989, leaving out the 1990-2007 period as an additional dataset to test hindcast skill. Correlations were investigated for both the combined October-November period and the individual month of November. Figure 1 displays a linear correlation map between October-November sea surface temperature and the following year's NTC over the period from 1950-1989. Note the large areas of positive correlation in the North Atlantic.

Areas selected as predictors correlated significantly at the 95% level ($r > |0.31|$) with NTC over the period from 1950-1989. Significance was determined by using a two-tailed Student's t-test and assuming that each hurricane season represents one degree of freedom. This assumption seems reasonable as the auto-correlation between one year's NTC and the following year's NTC is only 0.22. The areas selected had to be of fairly large spatial extent (at least 10° latitude by 15° longitude) in order to avoid selecting correlation "bulls-eyes" which sometimes exist in the NCEP/ NCAR reanalysis. In order to remain in the predictor pool, several additional criteria had to be met. First, the correlation between the predictor and NTC had to remain significant at the 95% level ($r > |0.47|$) over the period from 1990-2007. Second, the predictor had to show significant correlations with physical features during the following August-October period that are known to effect Atlantic basin hurricane activity, such as alterations in wind shear patterns, sea level pressure patterns, and sea surface temperature patterns (Gray 1984a, b, Knaff 1997, Goldenberg et al. 2001). Finally, when the predictors were added using stepwise regression, they had to add at least three percent additional variance explained for NTC over the three time periods of 1950-1989, 1990-2007 and 1950-2007.

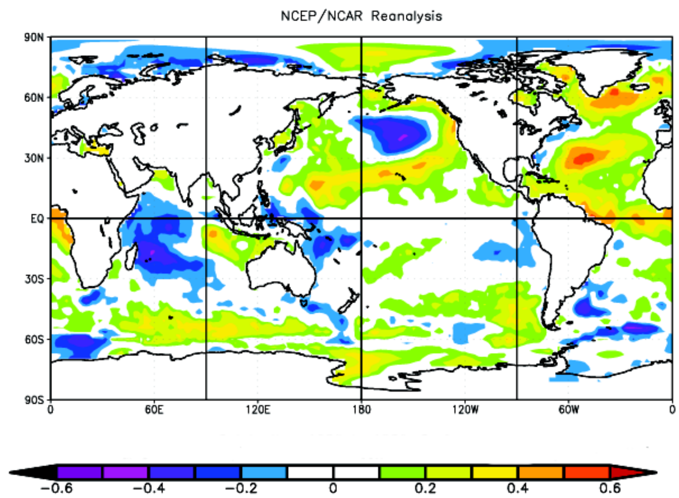

Fig. 1. Linear correlation between October-November sea surface temperature and the following year's Net Tropical Cyclone activity over the period from 1950-1989.

4. Results

Figure 2 displays the locations of the predictors on a map. Only three predictors were utilized in this forecast scheme. It is believed that by regressing against only one index (NTC) and keeping the predictor pool small, the scheme will likely show more skill than some of the earlier schemes utilized by the TMP that had much larger predictor pools. The dangers of over-fitting a statistical scheme that utilizes only three predictors should be considerably reduced.

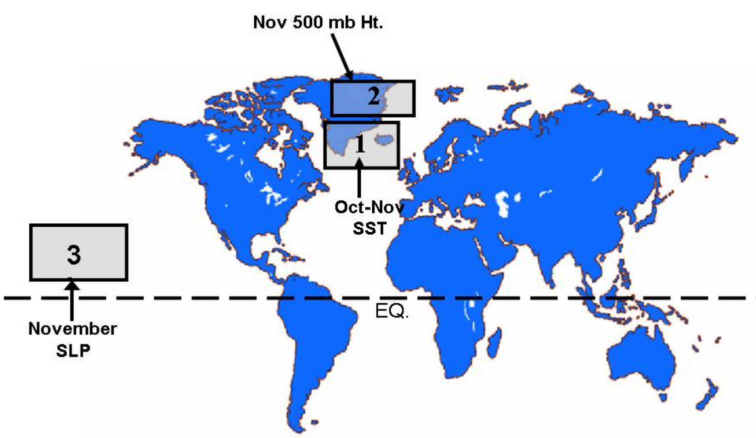

Fig. 2. Location of predictors utilized in the new early December statistical forecast scheme.

Table 1 displays the locations and individual correlations between each of the three predictors and NTC over the developmental period from 1950-1989, the test period of 1990-2007 and the full period of 1950-2007. As mentioned in the methodology section, all predictors are significant at the 95% level over all three time periods.

Table 2 displays the variance explained of these three predictors using stepwise regression over the period from 1950-1989 and applying those equations (developed from 1950-1989 using the stepwise

Predictor	Latitude-Longitude Region	1950-1989 Correlation	1990-2007 Correlation	1950-2007 Correlation
1) October-November SST in the North Atlantic (+)	(55-65°N, 60-10°W)	0.48	0.56	0.55
2) November 500 MB Geopotential Height in the far North Atlantic (+)	(67.5-85°N, 50°W-10°E)	0.52	0.48	0.51
3) November SLP in the Subtropical Northeast Pacific (+)	(7.5-22.5°N, 175-125°W)	0.33	0.53	0.36

Table 1. Listing of predictors selected for the early December forecast. The sign of the predictor associated with above-normal tropical cyclone seasons is in parentheses. The correlation of predictors with NTC over the following periods (1950-1989, 1990-2007 and 1950-2007) is also provided.

regression technique) to the 1990-2007 period. Also, the variance explained over the full period using equations developed over 1950-1989 is listed. North Atlantic SST is added to the scheme first, followed byfar North Atlantic 500 mb geopotential height and then subtropical Northeast Pacific sea level pressure. Note that the addition of each predictor adds considerable amounts of variance explained for each of the three periods examined. The hindcast scheme explains 40% of the variance over the dependent period from 1950-1989, while explaining 53% of the variance over the test period from 1990-2007. Over the full time period (1950-2007), the scheme explains 46% of the variance, using equations developed on 1950-1989.

If equations are developed over the full forecast period from 1950-2007, variance explained for NTC increases slightly to 47%. The average error using the hindcasts is 32 NTC units, compared with 44 NTC units using climatology. This reduction in average error is statistically significant at the 95% level using a two-tailed Student's t-test. The hindcasts are able to correctly predict an above- or below-average season (greater than or less than 100 NTC units) in 45 out of 58 years. It is remarkable that such a simple statistical scheme using only three predictors can explain such a large amount of variance in NTC seven months before the start of the hurricane season. It is likely the interaction between large-scale modes such as El Niño-Southern Oscillation (ENSO) (Rasmusson and Carpenter 1982), the Atlantic Multi-Decadal Oscillation (AMO) (Goldenberg et al. 2001) and the Pacific Decadal Oscillation (PDO) (Mantua et al. 1997) provide the long-period memory that gives the model its hindcast skill.

Period	Predictor 1	Predictors 1 and 2	Predictors 1, 2, and 3
1950-1989	0.23	0.32	0.40
1990-2007	0.31	0.45	0.53
1950-2007	0.30	0.38	0.46

Table 2. Stepwise regression technique documenting the increase in variance explained for NTC over the periods of 1950-1989, 1990-2007 and 1950-2007, respectively. Equations were developed over the 1950-1989 period. Predictor numbers are the same as listed in Table 1.

A new addition to this statistical forecast model when compared with earlier statistical forecast schemes used by the TMP is using a rank technique to adjust the statistical hindcasts. The ranking technique is generated by ranking all statistical hindcast values over the 1950-2007 period from 1 to 58. Then, actual observed NTC values for that ranking are assigned to a particular year. For example, 1953 ranked as the seventh largest hindcast value. The seventh largest observed value of NTC from 1950-2007 was 188, and therefore, 1953 was assigned a final rank hindcast NTC value of 188. It should be noted that several observed values of NTC were either below 40 or above 200. However, especially at this early lead time, the confidence in the statistical scheme is not high enough to assign values greater than 200 or lower than 40.

The average error using the rank hindcast technique is reduced to 28 NTC units (compared with 32 NTC units using the original statistical hindcasts), and the variance explained increases to 54 percent (compared with 47 percent using the original statistical hindcasts). Figure 3 displays the final rank hindcasts versus observations for seasonal NTC from 1950-2007.

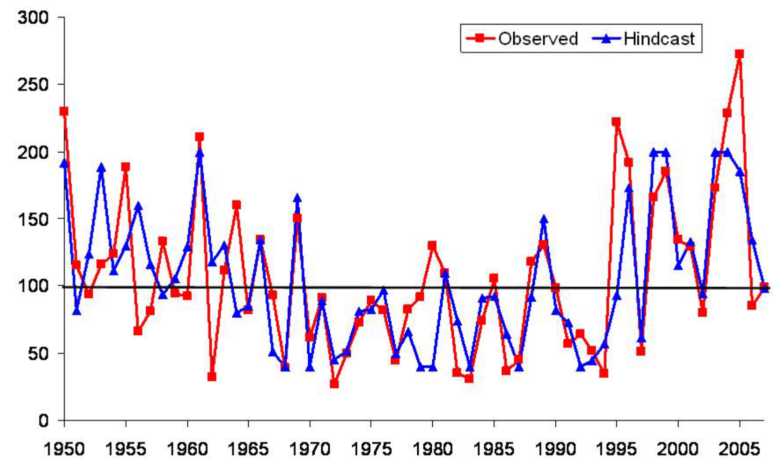

Fig. 3. Rank hindcast NTC compared with observed NTC over the period from 1950-2007. The rank hindcasts explain 54% of the variance in observed NTC.

One of the primary reasons why this forecast was developed was to provide a better real-time statistical model for seasonal NTC prediction in early December. Table 3 displays observed values of NTC from 1992-2007 along with actual real-time NTC forecast values and hindcast values from the new statistical scheme. One can clearly see the dramatic improvements that are made through implementation of the new hindcast scheme. Absolute forecast errors are reduced by approximately 55% when compared with

Year	Observed NTC	Real-Time NTC Prediction	New Model NTC Hindcast	Real-Time Error	New Model Hindcast Error	Error Using Climatology
1992	65	61	40	4	25	-35
1993	52	117	45	-65	7	-48
1994	35	110	57	-75	-22	-65
1995	222	140	93	82	129	122
1996	192	85	173	107	19	92
1997	52	110	62	-58	-10	-48
1998	169	90	200	79	-31	69
1999	182	160	200	22	-18	82
2000	130	125	115	5	15	30
2001	134	90	133	44	1	34
2002	82	140	94	-58	-12	-18
2003	174	140	200	34	-26	74
2004	229	125	200	104	29	129
2005	277	115	185	162	92	177
2006	85	195	134	-110	-49	-15
2007	99	140	98	-41	1	-1
Avg. Error				|66|	|30|	|65|

Table 3. Observed NTC, real-time NTC prediction, new statistical model NTC hindcast, real-time forecast error, new model hindcast error and error using climatology over the period that December forecasts have been issued (1992-2007). The new model-derived hindcast errors improve upon climatology or real-time forecast errors by approximately 55%.

either the real-time forecast or climatology. The new hindcast scheme's error is smaller than climatology in 14 out of 16 years and is smaller than the real-time forecast's error in 13 out of 16 years. The model was used in real-time prediction for the first time for the 2008 Atlantic basin hurricane season. The statistical model called for a somewhat above-average hurricane season of 127 NTC units. As of the end of October, seasonal NTC was observed to be 145 NTC units, which indicates a reasonably successful forecast.

5. Physical Relationships between Predictors and Atlantic Basin Hurricane Activity

One of the primary reasons why some of the TMP's earlier statistical forecast models have failed in real-time forecasting is likely due to a lack of rigorous statistical tests and inadequate understanding of the physical relationships between individual predictors and Atlantic hurricane activity. In the previous section, the more rigorous statistical tests that were conducted in order to verify the legitimacy of individual predictors were demonstrated. In this section, individual predictors and their likely physical relationships with Atlantic basin hurricane activity are discussed. Correlation maps between individual predictors and August-October sea surface temperature, sea level pressure, 200 mb zonal wind and 925 mb zonal wind are provided. These maps illustrate the fact that these predictors are likely physically tied to features that are known to effect Atlantic basin hurricane activity.

a. Predictor 1. October-November SST in the North Atlantic (55°-65°N, 60-10°W) (+)

Warm North Atlantic sea surface temperatures in the fall are indicative of an active phase of the Atlantic Multidecadal Oscillation (AMO) and a strong Atlantic thermohaline circulation (Goldenberg et al. 2001). There tends to be a fairly strong auto-correlation between North Atlantic SSTs in this region during the late fall and SSTs during the following August-October period as seen in Panel (a) of Figure 4. An active AMO is associated with anomalously low vertical wind shear, anomalously warm tropical Atlantic sea surface temperatures and anomalously low sea level pressures during August-October (Figure 4). These anomalously low values of vertical wind shear are generated by a weakening of the Tropical Upper Tropospheric Trough (TUTT) in the central Atlantic. When this occurs, upper-level westerlies and low-level easterlies are reduced, thereby reducing vertical wind shear.

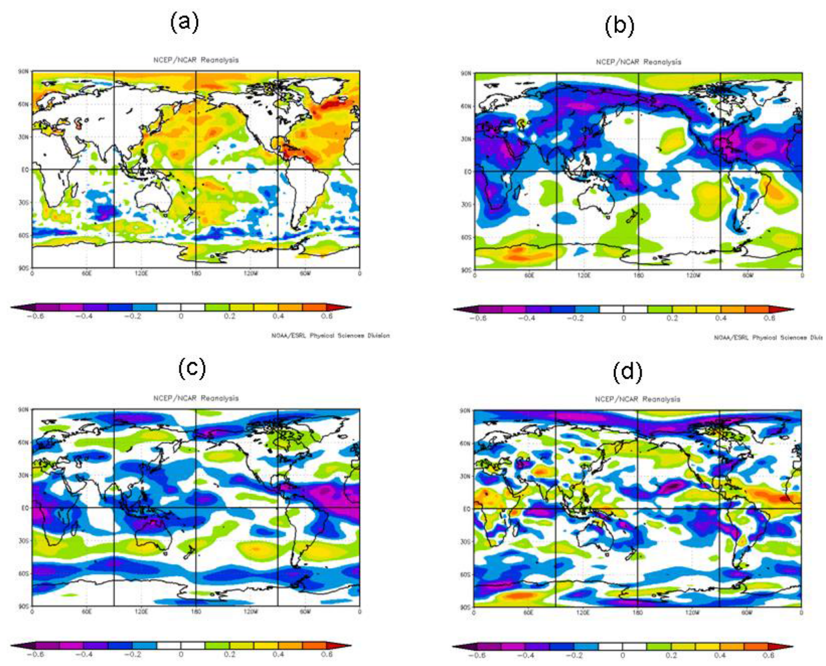

Fig. 4. Linear correlation between October-November SST in the North Atlantic (Predictor 1) and the following year's August-October sea surface temperature (panel a), August-October sea level pressure (panel b), August-October 200 mb zonal wind (panel c) and August-October 925 mb zonal wind (panel d).

b. Predictor 2. November 500 mb Geopotential Height in the far North Atlantic (+) (67.5-85°N, 50°W-10°E)

Predictor 2 correlates at -0.73 with November values of the Arctic Oscillation (AO) (Thompson and Wallace 1998) and at -0.55 with November values of the North Atlantic Oscillation (NAO) (Barnston and Livezey 1987). Negative AO and NAO values imply more blocking or ridging in the central Atlantic and an associated reduction in the strength of the westerlies. In addition, a negative NAO is associated with a weaker Azores High, resulting in weaker trade winds and positive SST anomalies in the tropical Atlantic (Marshall et al. 2001). These anomalies are clearly evident during the following August-October period (Figure 5). Other following summer-early fall features that are directly correlated with this predictor are low sea level pressure in the Caribbean and easterly anomalies at 200 mb, resulting in weaker vertical wind shear (Figure 5). Both of these are also hurricane-enhancing factors.

c. Predictor 3. November SLP in the Subtropical Northeast Pacific (+) (7.5-22.5°N, 175-125°W)

High pressure in the subtropical northeast Pacific tends to appear during the fall and winter prior to a La Niña event (Larkin and Harrison 2002). High pressure forces stronger trade winds in the East Pacific which encourages mixing and increases upwelling, helping to initiate La Niña conditions. Also, these stronger trades likely help keep cool conditions in the tropical Pacific into the upcoming hurricane season, by inhibiting the recharge and discharge of the warm pool during the winter and spring months. Figure 6 displays linear correlations between Predictor 3 and the following August-October's values of sea surface temperature, sea level pressure, 200 mb zonal wind and 925 mb zonal wind. Note the large area of negative correlations for SST in the tropical Pacific indicative of La Niña. Cool ENSO conditions are associated with reduced vertical wind shear across the tropical Atlantic and especially in the Caribbean (Gray 1984b, Klotzbach 2007).

6. Early December NTC Hindcasts and U.S. Landfalling Tropical Cyclones

The TMP has been issuing landfall probability forecasts since August 1998. The primary

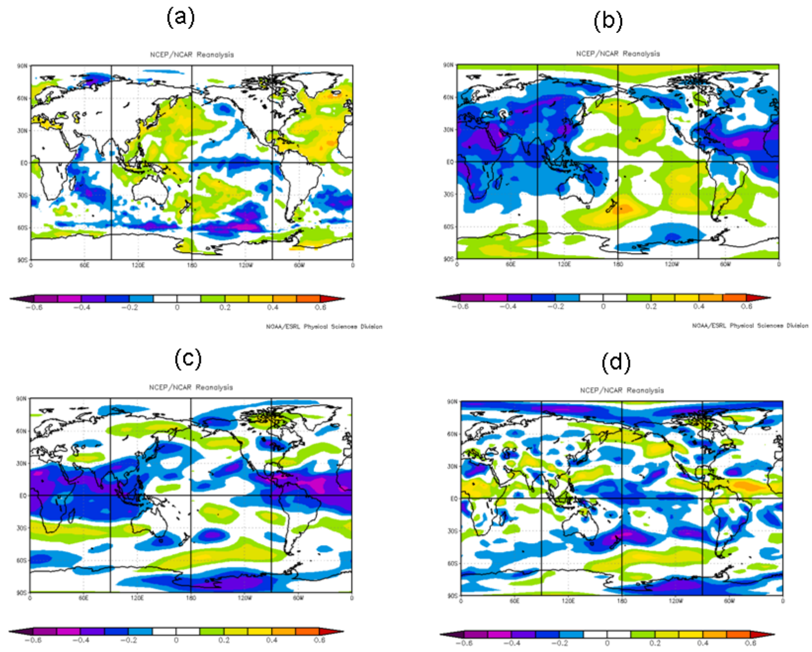

Fig. 5. Linear correlation between November 500 mb geopotential height in the far North Atlantic (Predictor 2) and the following year's August-October sea surface temperature (panel a), August-October sea level pressure (panel b), August-October 200 mb zonal wind (panel c) and August-October 925 mb zonal wind (panel d).

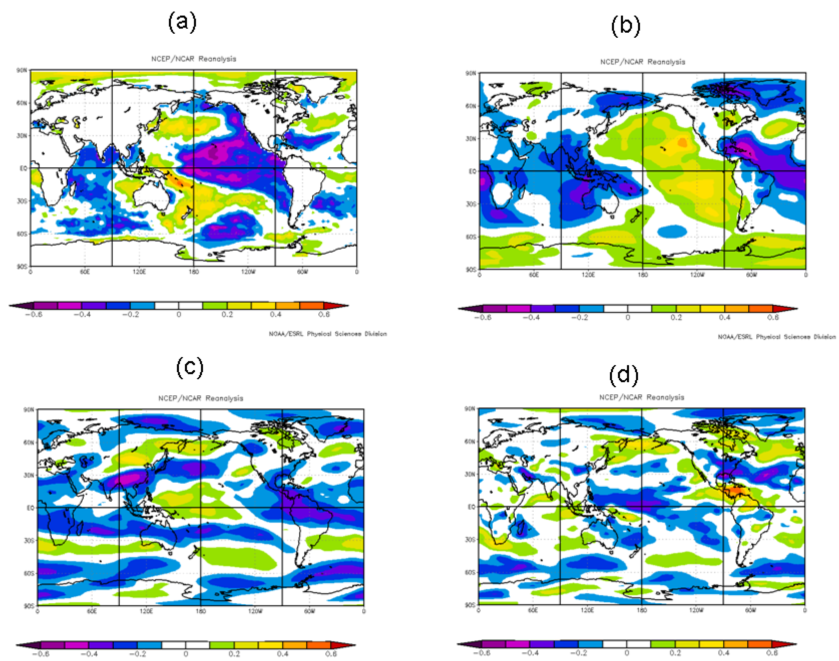

Fig. 6. Linear correlation between November SLP in the subtropical northeast Pacific (Predictor 3) and the following year's August-October sea surface temperature (panel a), August-October sea level pressure (panel b), August-October 200 mb zonal wind (panel c) and August-October 925 mb zonal wind (panel d).

justification for issuing these forecasts is that on a statistical basis, more active tropical cyclone seasons have more landfalling storms than do inactive tropical cyclone seasons. If seasonal forecasts are developed that have statistical skill at forecasting tropical cyclone seasons, there should also be skill in issuing landfall probability forecasts, as discussed in Klotzbach (2007). For this newly-developed December scheme, considerable differences exist between seasons with high NTC hindcasts compared with low NTC hindcasts. In keeping with discussions in Klotzbach and Gray (2004) and Klotzbach (2007), the strongest ratios are found for storms making landfall along the Florida Peninsula and East Coast. For example, the top 15/bottom 15 NTC landfall ratios are 36 to 17 for named storms, 19 to 8 for hurricanes and 7 to 2 for major hurricanes. Figure 7 displays the tracks of the major hurricanes making landfall in the top 15 and bottom 15 NTC hindcasts for the Florida Peninsula and East Coast.

7. Conclusions and Future Work

There exists significant hindcast skill in predicting the following year's Net Tropical Cyclone activity parameter by early December (seven months prior to the start of the hurricane season). A simple statistical scheme utilizing three predictors is able to explain over 50% of the variance in NTC over the period from 1950-2007. Predictors were selected based on their skill over the period from 1950-1989, while the 1990-2007 was set aside for additional testing of model skill. Physical relationships between individual predictors and the following year's hurricane season were discussed. NTC hindcasts were also shown to exhibit significant relationships with U.S. landfalling hurricanes, especially along the Florida Peninsula and East Coast.

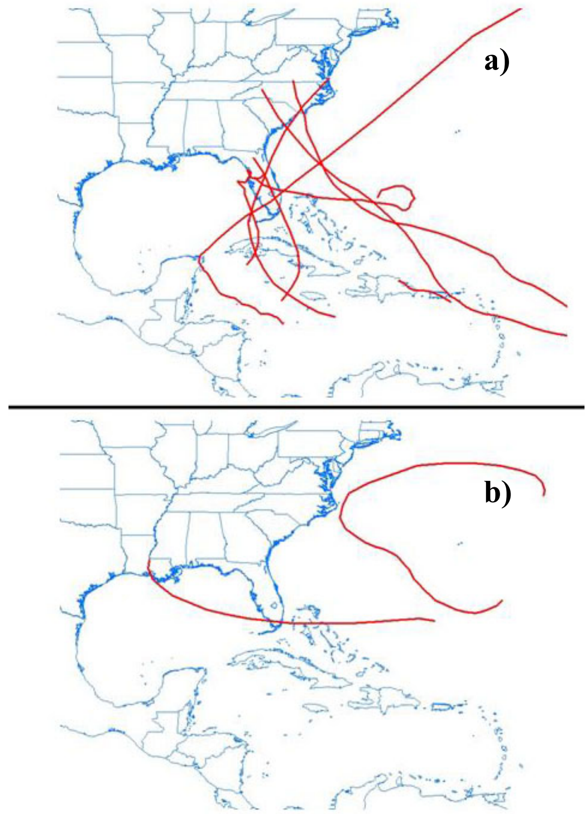

Fig. 7. Tracks of major hurricanes making Florida Peninsula and East Coast landfall for the top 15 NTC hindcasts (panel a) and bottom 15 NTC hindcasts (panel b). Seven major hurricanes made landfall in the top 15 NTC hindcasts compared with two major hurricanes in the bottom 15 NTC hindcasts.

References

Barnston, A. G., and R. E. Livezey, 1987: Classification, seasonality and persistence of low-frequency atmospheric circulation patterns. *Mon. Wea. Rev.*, **115**, 1083-1126.

Goldenberg, S. B., C. W. Landsea, A. M. Mestas-Nuñez, and W. M. Gray, 2001: The recent increase in Atlantic hurricane activity: Causes and implications. *Science,* **293,** 474-479.

Gray, W. M., 1984a: Atlantic seasonal hurricane frequency. Part I: El Niño and 30 mb quasi-biennial oscillation influences. *Mon. Wea. Rev.,* **112,** 1649-1668.

Gray, W. M., 1984b: Atlantic seasonal hurricane frequency. Part II: Forecasting its variability. *Mon. Wea. Rev.,* **112,** 1669-1683.

Gray, W. M., C. W. Landsea, P. W. Mielke Jr., and K. J. Berry, 1992: Predicting Atlantic seasonal hurricane activity 6-11 months in advance. *Wea. Forecasting,* **7,** 440-455.

Gray, W. M., C. W. Landsea, P. W. Mielke Jr., and K. J. Berry, 1994: Predicting Atlantic basin seasonal tropical cyclone activity by 1 June. *Wea. Forecasting,* **9,** 103-115.

Jarvinen, B. R., C. J. Neumann, and M. A. S. Davis, 1984: A tropical cyclone data tape for the North Atlantic basin, 1886-1983: Contents, limitations, and uses, 21 pp. *NOAA Tech. Memo.* NWS NHC 22, Miami, FL.

Kistler, R., and Co-Authors, 2001: The NCEP-NCAR 50-year reanalysis: Monthly means CD-ROM and documentation. *Bull. Amer. Meteor. Soc.,* **82,** 247-267.

Klotzbach, P. J., 2007: Revised prediction of seasonal Atlantic basin tropical cyclone activity from 1 August. *Wea. Forecasting,* **22,** 937-949.

Klotzbach, P. J., 2008: Refinements to Atlantic basin seasonal hurricane prediction from 1 December. *J. Geophys. Res.,* **113,** D17109, doi: 10.1029/2008JD010047.

Klotzbach, P. J., and W. M. Gray, 2004: Updated 6-11-month prediction of Atlantic basin seasonal hurricane activity. *Wea. Forecasting,* **19,** 917-934.

Knaff, J. A., 1997: Implications of summertime sea level pressure anomalies in the tropical Atlantic region. *J. Climate,* **10,** 789-804.

Landsea, C. W., 1993: A climatology of intense (or major) Atlantic hurricanes. *Mon. Wea. Rev.,* **121,** 1703-1713.

Larkin, N. K., and D. E. Harrison, 2002: ENSO warm (El Niño) and cold (La Niña) event life cycles: Ocean surface anomaly patterns, their symmetries, asymmetries and implications. *J. Climate,* **15,** 1118-1140.

Mantua, N. J., S. R. Hare, Y. Zhang, J. M. Wallace, and R. C. Francis, 1997: A Pacific decadal climate oscillation with impacts on salmon. *Bull. Amer. Meteor. Soc.*, **78,** 1069-1079.

Marshall, J., and Co-Authors, 2001: North Atlantic climate variability: Phenomena, impacts and mechanisms. *Int. J. Climatol.,* **21,** 1863-1898.

Rasmusson, E. M., and T. H. Carpenter, 1982: Variations in tropical sea surface temperature and surface wind fields associated with the Southern Oscillation/El Niño. *Mon. Wea. Rev.,* **110,** 354-384.

Owens, B. F., and C. W. Landsea, 2003: Assessing the skill of operational Atlantic seasonal tropical cyclone forecasts. *Wea. Forecasting,* **18,** 45-54.

Thompson, D. W. J., and J. M. Wallace, 1998: The Arctic Oscillation signature in the wintertime geopotential height and temperature fields. *Geophys. Res. Lett.,* **25,** 1297-1300.

Science and Technology Infusion Climate Bulletin
NOAA's National Weather Service
33rd NOAA Annual Climate Diagnostics and Prediction Workshop
Lincoln, NE, 20-24 October 2008

Towards a Global Drought Monitoring and Forecasting Capability

Lifeng Luo[1, 2], Justin Sheffield[1], Eric F. Wood[1]
[1]*Environmental Engineering and Water Resources,*
Department of Civil and Environmental Engineering, Princeton University
[2]*Program in Atmospheric and Oceanic Sciences, Princeton University*

1. Introduction

Droughts are as much a part of weather and climate extremes as floods, hurricanes and tornadoes, but are the most costly extremes among all natural disasters in the U.S. [Ross and Lott, 2003]. The estimated annual direct losses to the U.S economy due to droughts are about \$6–\$8 billion, with the drought of 1988 estimated to have damages over \$39 billion [Federal Emergency Management Agency, 1995]. Over other parts of the world, droughts are also among the most damaging of natural disasters in human, environmental and economic terms. The consequences of drought are perhaps nowhere more urgent than in Africa where IPCC projections of increase future drought frequency have perilous implications for the livelihood of residents who depend heavily upon ecosystem services. Unlike other natural disasters, droughts develop slowly over large areas and over an extended period of time, making it difficult to identify them until they have become severe and some damage has already occurred. Therefore, accurate quantitative assessment of drought conditions and the prediction of the on-set, duration and recovery of droughts in realtime are critical for drought planning and preparedness.

Studies over the last two decades have demonstrated the feasibility of seasonal climate predictions with dynamical climate models. The skill of seasonal predictions is believed to come from the slow varying components of the climate system, mainly tropical Pacific sea surface temperature, although more recently surface soil moisture has also shown certain contributions over transition zones between dry and wet climatic regions (Koster *et al.* 2000 and 2004). At present, seasonal climate predictions are made routinely at several weather and climate prediction centers and research institutes, including the European Centre for Medium-range Weather Forecasting (ECMWF), and in the U.S. the National Centers for Environmental Prediction (NCEP). The predictions have shown significant skill over the tropics, while in the mid-latitudes their skill is improving, with some models showing skill comparable to the skill from statistical models (Saha *et al.* 2006). There is the expectation that these seasonal dynamical climate forecasts can contribute to the development of seasonal hydrologic prediction capabilities.

However, challenges must be overcome in utilizing seasonal climate forecasts from dynamical climate models in a seasonal hydrologic prediction system. One significant challenge is to correct the biases in climate model predictions, especially those related to precipitation and temperature. Another challenge is to resolve the disparity in spatial scales between the ones resolved in climate models and those needed for hydrologic applications. For instance, the current operational NCEP global coupled ocean-atmosphere model, called the Climate Forecast System (CFS) (Saha *et al.* 2006), runs at T62L64 resolution (~1.875 degree in longitude). The climate models in the European Union (EU) DEMETER project (Palmer et al. 2004) provide hindcasts at a resolution of 2.5°×2.5°. However the hydrologic predictions need atmospheric forcing at a much finer resolution. As an example, the North America Land Data Assimilation System (NLDAS) (Mitchell *et al.* 2004), which provides real-time hydrologic simulations across the continental U.S., has adopted a spatial scale of 1/8th degree. Such disparities require a seasonal hydrologic forecast system to spatially downscale the information provided by the climate models to the finer hydrologic scale where the information can be properly used. The third challenge is to create realistic daily atmospheric forcing for hydrologic modeling from the monthly information provided by the climate models. Climate model forecasts are generally only available as a monthly forecast while the hydrologic models are run at daily or sub-daily

Correspondence to: Lifeng Luo, Environmental Engineering and Water Resources, Department of Civil and Environmental Engineering, Princeton University; E-mail: lluo@Princeton.EDU

time steps. To make skillful seasonal hydrologic predictions, a good strategy is needed to overcome these challenges.

This report summarizes the current research activity by the Princeton Land Surface Hydrology Group on developing the capability to monitor and forecast drought in near realtime for the US and globally. Part of the system is currently in transition to EMC/NCEP for operational testing. In the next two sections, we briefly describe the methodology for the Drought Monitoring and Prediction System (DMAPS), and present examples of its implementation for the US and its pilot extension to Africa, followed by a brief summary.

2. Methodology

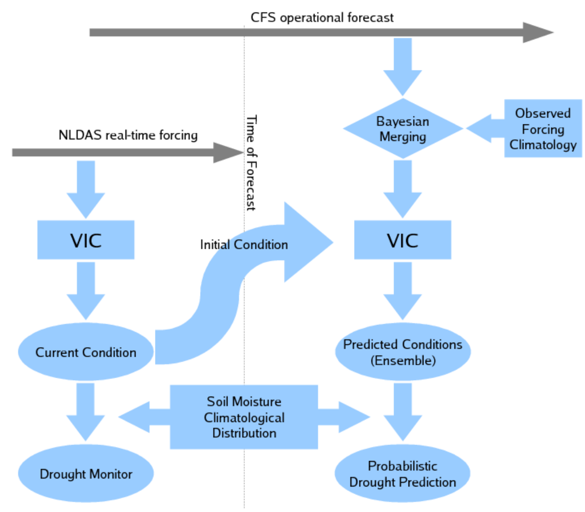

Fig. 1. Schematic diagram of the drought monitoring and prediction system (DMAPS)

Figure 1 provides a schematic diagram of our current approach for drought monitoring and prediction over the U.S. The central element of DMAPS is the Variable Infiltration Capacity (VIC) hydrological model [Liang *et al.*, 1996; Cherkauer *et al.*, 2003] that transforms meteorological information into hydrological information such as soil moisture and streamflow. VIC is one of several state-of-the-art macroscale hydrological models available, and it has been calibrated and evaluated in numerous studies at grid, basin and continental scales [Nijssen *et al.*, 1997; Cherkauer and Lettenmaier, 1999; Maurer *et al.*, 2002; Roads *et al.*, 2003; Nijssen *et al.*, 2001; Sheffield and Wood, 2007].

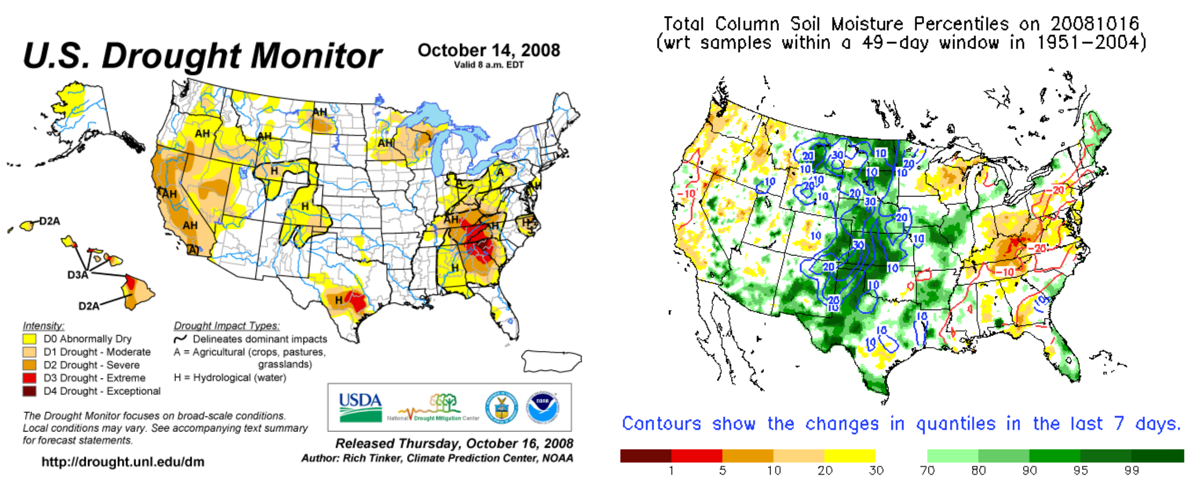

Fig. 2. Comparison of the Princeton drought monitor with CPC Drought Monitor in the week of October 14, 2008.

For drought monitoring, the approach is to use the VIC model with realtime atmospheric forcing provided by the North American Land Data Assimilation System (NLDAS) [Mitchell et al., 2004] to estimate the current total column soil moisture at each 1/8 degree grid across the continental U.S. A drought index value is computed for each grid, where the index is expressed as a percentile value of the current soil moisture with respect to its climatological probability distribution [Sheffield *et al.*, 2004a]. The climatological distribution at each grid was obtained by running the VIC model with an observational atmospheric forcing dataset [Maurer *et al.*, 2002; Cosgrove *et al.*, 2003] for the period of 1949–2004, then sampling daily soil moisture values from days that are within a 49-day sampling window centered on the current day of each year. This gives a reasonable representation of the modeled soil moisture climatology with over 2500 samples. Both the realtime NLDAS forcing and the historical forcing are observation based and their quality has been validated in several studies [Luo *et al.*, 2003; Maurer *et al.*, 2002]. The soil moisture values obtained from these simulations have been shown to accurately represent soil moisture dynamics [Robock *et al.*, 2003; Maurer *et al.*, 2002]. Because the soil moisture percentile-based drought index provides a quantitative measure as a spatially continuous field, it can be used in drought forecasting. As illustrated in Figure 2, the drought assessment from our index and those of the Climate Prediction Center's (CPC) Drought Monitor [Svoboda *et al.*, 2002] are comparable (see http://hydrology.princeton.edu/forecast/). The major differences between the two are that CPC's drought monitor is somewhat subjective, since human analysts blend five key indicators and numerous supplementary indicators together to form a drought intensity map, and that CPC's drought monitor includes hydrologic drought which is defined as a low snowpack, streamflow or reservoir levels.

The drought prediction component of DMAPS utilizes the seasonal hydrologic prediction system described in detail by Luo and Wood [2008]. As the drought monitoring component provides the best estimate of hydrologic initial conditions for the forecast through observation-based spinup, the prediction component needs to properly address the uncertainties associated with the atmospheric forcing, which is the major contributor to the total uncertainty in seasonal hydrologic forecast. Thus the accuracy of the atmospheric forcings is essential to the skill of the hydrologic predictions. Due to the nature of the forecast problem, atmospheric forcings cannot be accurately predicted; instead, their uncertainties need to be accurately quantified via an ensemble approach. Our goal is to create an ensemble of atmospheric forcings that reflects our best estimate of future conditions and their uncertainties. As illustrated in Figure 1, to achieve this, the system implements a Bayesian merging procedure [Luo *et al.,* 2007] to combine seasonal forecasts from dynamical climate models with observed climatology at the monthly level to obtain posterior distributions for monthly precipitation and temperature at each grid for each month of the forecast period. Figure 3 illustrates the use of the Bayesian merging technique to combine a SST forecast from one DEMETER climate model with observed climatology to achieve a better estimate of the posterior distribution. This process effectively removes biases in the climate model seasonal forecasts and statistically downscales the forecasts from climate model scales to the smaller scale that is more appropriate for hydrologic applications. When making seasonal hydrologic predictions at the beginning of each month, the system takes all the members from NCEP's CFS [Saha et al., 2006] seasonal forecast issued during the previous month and passes them through the Bayesian merging procedure to obtain the posterior distributions that are sampled to generate 20 atmospheric forcing ensembles for the hydrologic prediction. The 20 atmospheric forcing time series are based on 20 historical daily forcing time series from the dataset provided by Maurer *et al.* [2002] and adjusted at the daily level to match the monthly forecast values sampled from the posterior distribution. Half of the members are selected randomly from all available historical records and the other half are selected with a historical-analogue criterion. For the latter, all historical precipitation patterns are compared with the current predicted precipitation pattern (mean of the

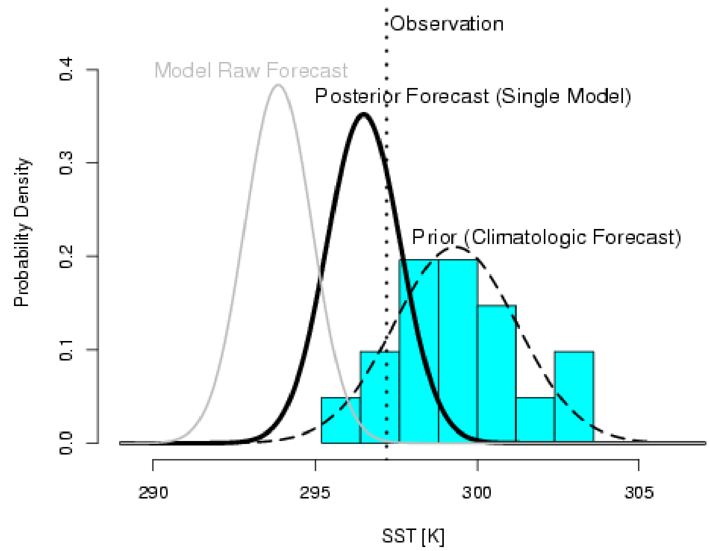

Fig. 3. Prior distribution (dashed black) and posterior distribution (solid black) for the forecast of monthly mean SST over selected grid (2.5 x 2.5 centered at 0 and 130W) of December 1998. The raw forecast (solid gray) distribution estimated from one EU DEMETER climate model is also plotted. The vertical dotted line indicates the actual observation for December 1998. The prior distribution is estimated from data spanning 1982 to 1999 except 1998. The histogram of the 19 months is also shown.

posterior distribution) and are sorted by their similarities to the current predicted pattern. The similarity is simply measured by the root mean square difference (RMSD) of the two, calculated for all grids in the region and all six–month periods. The likelihood of realization for each ensemble member is considered to be larger if its RMSD value is smaller. Therefore the 10 historical years with the smallest RMSD values are selected. Although simple and empirical, this selection criterion considers the similarity in spatial and temporal patterns in monthly precipitation anomalies. The small ensemble set formed by the seven members with largest likelihood of realization is noted as the ''most-likely ensemble set''. As shown in the next section, using the CFS seasonal climate forecasts, the hydrological prediction with the most-likely ensemble set has shown promising skill in predicting recent droughts over the West and Southeast of the U.S.

3. Drought monitoring and forecasting over the US

The drought forecast system was tested initially with retrospective forecasts of selected historical drought events in the US. The successful prediction of the onset, development, and recovery of droughts is very valuable for drought impact preparation and mitigation. The summer of 1988 was very dry over the central northern part of United States. The severe drought conditions lasted more than five months, causing significant damages to agriculture and the local economy [American Meteorological Society 1997]. Here, we use the summer of 1988 forecasts for the Ohio River basin as an example to illustrate the skill of our prediction system (Figure 4). Results are shown for three different approaches (ESP, CFS, and CFS+DEMETER). The Ensemble Streamflow Prediction (ESP) forecast is a proxy of the forecast approach used operationally at river forecast centers (RFCs). The CFS-based forecast utilizes the information from seasonal climate forecast from the NCEP CFS in the Bayesian merging procedure, and the CFS+DEMETER forecast is the same as the CFS-based forecast except that it also uses forecast information from 7 DEMETER models, thus forming a multi-model Bayesian merging. As shown in Figure 4, at the beginning of May 1988 much of the region was already in drought, so all three approaches predicted dry soil moisture anomalies, as indicated by the low percentile values of the ensemble mean. However, the development of the drought is predicted differently by the three different approaches, mainly as a result of the difference in precipitation forecasts. The drought as predicted by CFS+DEMETER persists much longer (to the end of the forecast period), whereas the drought almost recovers in June according to the ESP forecast.

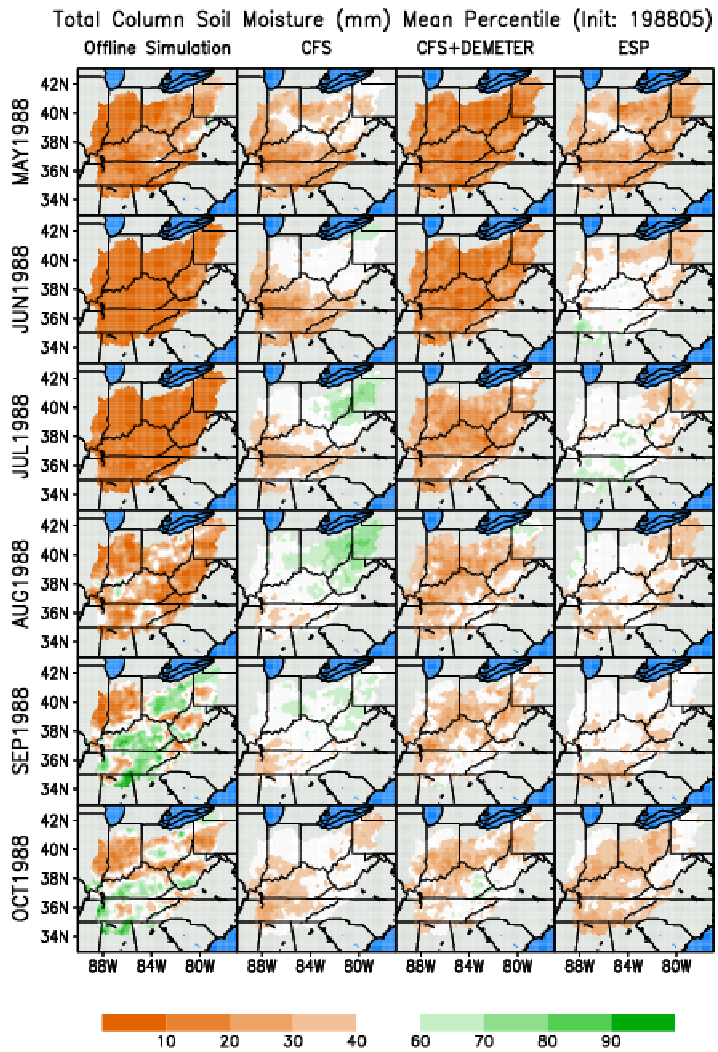

Fig. 4. Comparison of soil moisture forecasts (ensemble mean of monthly average soil moisture expressed as the percentile value within the climatological distribution) from (right three columns) three forecast approaches and observations. (left column) The retrospective offline simulation of VIC, driven by the Maurer et al. (2002) dataset that serves as a proxy for observations.

During early 2007, severe droughts developed over the west and southeast of the U.S. These events were captured by our monitoring system and well predicted by our prediction made from the initial conditions on January 1, 2007. Figure 5 compares the predicted soil moisture conditions from the most-likely ensemble set of the 200701 forecast with the ''observed'' soil moisture condition from our realtime drought monitoring. The prediction indicates a severe drought developing over California and the ensemble spread (expressed as the difference in percentile values of the lower and upper quartile of the ensemble distribution) is small suggesting a highly confident prediction over the region (see the contours of the inter-quartile range in the left hand portion of Figure 5). Over the Southeast, it is predicted that a relatively weaker drought condition develops in February and expands to the entire Southeast in March. However, the ensemble spread is large (>30), suggesting that less confidence should be given to the prediction. Compared with the soil moisture conditions from the drought monitoring, the prediction over the West gives a very good correspondence in terms of the area and severity of the drought with accuracy values (hit rate) of 0.93, 0.92 and 0.88 for predicting soil moisture below the 20th percentile over the region during the first three months, respectively. Over the Southeast, the prediction is satisfactory but slightly less skillful with accuracy values of 0.94, 0.54 and 0.44. It under-predicted the severity of the drought locally over Mississippi, Alabama and Tennessee, and over-predicted the severity for the East Coast. Since the ensemble spread is quite large over these regions, such forecast errors are not surprising.

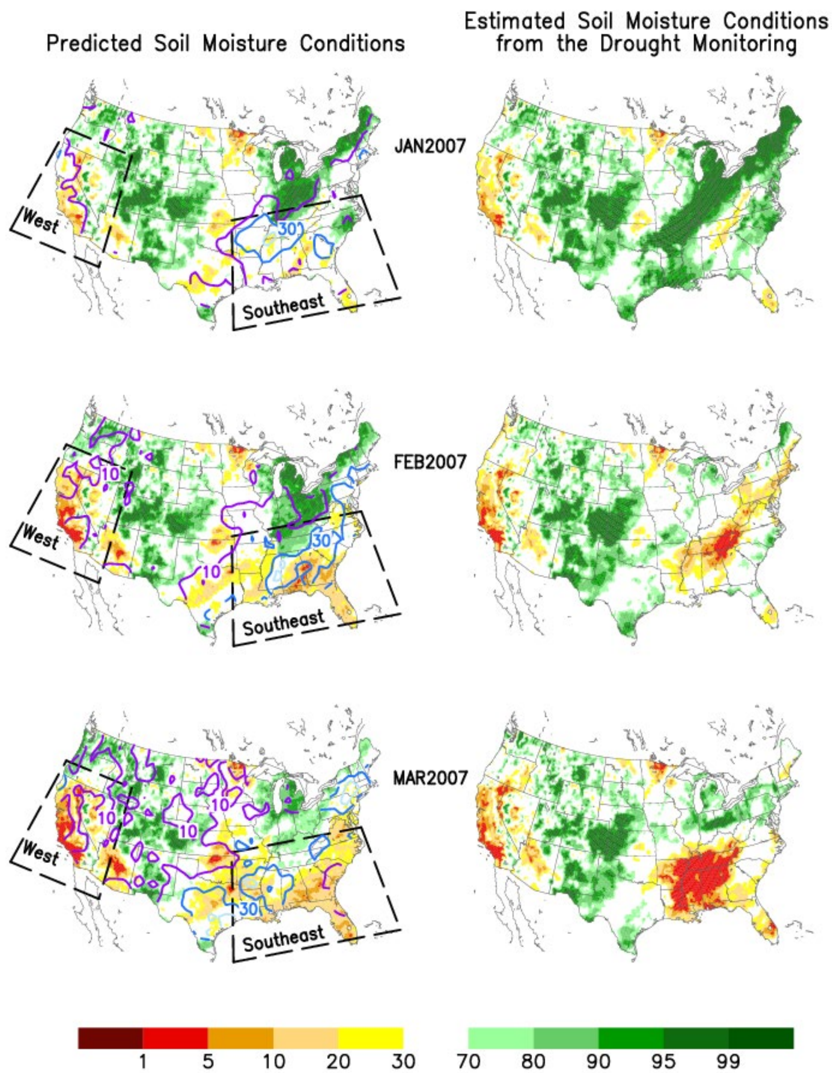

Fig. 5. Predicted soil moisture index for the first three months of the 200701 forecast that uses the initial condition on January 1, 2007, compared with the estimated soil moisture index from the realtime drought monitoring. Left column shows the mean of the most-likely ensemble set (shaded) and their spread (contour). See section 2 for the definition and basis of the index.

To further evaluate the skill of the predictions, Figure 6 shows the evolution of the droughts and their predictions over the West and the Southeast defined by the boxes in Figure 5. Within each region, the number of 1/8 degree grid cells where the monthly mean soil moisture value is below the 20th percentile threshold is counted for each month. The black solid lines in Figure 6 are from the realtime drought monitoring and represent the actual development of the droughts. For the predictions, grid cells that satisfy the same criteria are counted in each of the seven ensemble members and the counts are averaged to give the mean forecasts (solid green, blue and red lines). The spread of each ensemble forecast is indicated by the thin lines as one standard deviation from their mean. Evidently, the predictions are very skillful in capturing the evolution of the droughts over both regions, especially during the first two months of each forecast. Since predictability decreases with lead time, as illustrated by Luo and Wood [2006], we expect that forecast skill will also decrease with lead time, which is supported by the increase in ensemble spread and with the mean forecasts approaching climatology. Therefore, when interpreting the prediction, we tend to trust the predictions more at the shorter lead times.

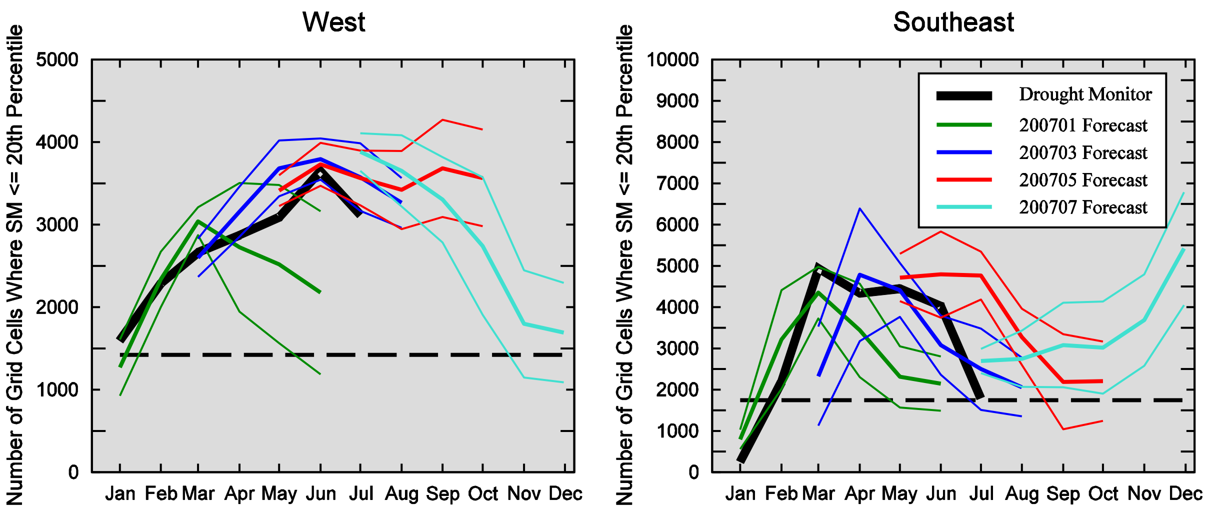

Fig. 6. Drought predictions with DMAPS over the West and the Southeast. Shown is the area (number of grid cells) where soil moisture index is below 20 (i.e., the 20th percentile of the climatological soil moisture distribution from the offline simulation). See text for a further discussion.

4. Towards a global drought monitoring and forecasting capability

These U.S. focused monitoring and prediction activities have provided the foundation for expansion to a global system. A first step towards this has been the development of an experimental system for Africa, the African Drought Monitor (ADM), developed jointly by Princeton University and the University of Washington, with support from UNESCO's International Hydrological Programme (IHP). This is now accessible at http://hydrology.princeton.edu/monitor. The ADM has the objective of providing near-real time (2-3 days latency) drought monitoring products based on VIC hydrologic output, and making these available for evaluation. Similar to the U.S. system (DMAPS), the ADM: i) provides near-real time fields of soil moisture and other hydrologic variables over Africa using observation-forced VIC simulations; ii) provides drought products that quantify the current state of drought in the context of the regional climatology; and iii) monitors where drought evolution and dissipation based on soil moisture thresholds.

The background climatology for drought assessment is based on long-term (1950-2000) global VIC land surface model simulations of terrestrial hydrology forced by the meteorological forcing dataset of Sheffield et al. [2006]. The bias corrected and downscaled forcings are applied at 1.0 degree latitude-longitude spatial resolution. The forcing data were constructed by combining a suite of global observation-based data sets with the NCEP/NCAR reanalysis [Kalnay *et al*, 1996]. Known biases in the reanalysis precipitation and near-surface meteorology are known to exert an erroneous effect on modeled land surface water and energy budgets [Maurer et al, 2001] and were corrected using observation-based precipitation, air temperature and downward solar radiation data. Corrections were also made to the rain day statistics of the reanalysis precipitation [Sheffield et al., 2004b], which have been found to exhibit a spurious wave-like pattern in high-latitude wintertime. Corrected reanalysis precipitation was disaggregated in space to 1.0 degree spatial resolution by statistical downscaling using relationships developed with the Global Precipitation Climatology Project (GPCP) daily product. Disaggregation in time from daily to 3-hourly was accomplished similarly, using the Tropical Rainfall Measuring Mission (TRMM) 3-hourly 3B42 data set. Other meteorological variables (downward short- and longwave, specific humidity, surface air pressure and wind speed) were downscaled in space with account for changes in elevation whilst maintaining inter-variable consistency. The hydrologic output and specifically the soil moisture from these retrospective simulations have been analyzed in terms of the occurrence and characteristics of drought [Sheffield and Wood, 2007] and their long-term trends and variability [Sheffield and Wood, 2008]. Figure 7 shows historic time series of the ADM Drought Index and area in drought for regions of Africa. Also shown are maps of monthly drought severity during these drought events.

For real-time monitoring, the availability of data provides real challenges, especially in data-sparse regions such as Africa. We therefore have to rely on data streams from various providers and locations, and thus use observations from several sources. At present, precipitation is taken from the Precipitation Estimation from Remotely Sensed Information using Artificial Neural Networks (PERSIANN) system. Surface air temperature and wind speed are gridded from Global Telecommunication System stations. Downward radiative fluxes and humidity are indexed to surface air temperature and its diurnal range. Backup meteorological data are taken from the NCEP Global Forecast System analysis fields when primary data are unavailable or fail quality control checks. Figure 8 shows current drought and hydrologic conditions at the time of writing from the ADM webpage. Inconsistencies between the 50-year model climatology and the near real-time data pose a major challenge. For instance, the PERSIANN satellite-based precipitation is generally higher than climatology which tends to bias the drought products. We are currently adding additional satellite-based real time precipitation streams (namely, the NCEP/CPC CMORPH product and NASA's TRMM TMPA-RT) that will give an indication of the uncertainty in the real time products. We are also working to extend our climatology period (currently to 2000) to provide a longer overlap period, and allow us to implement bias adjustment procedures.

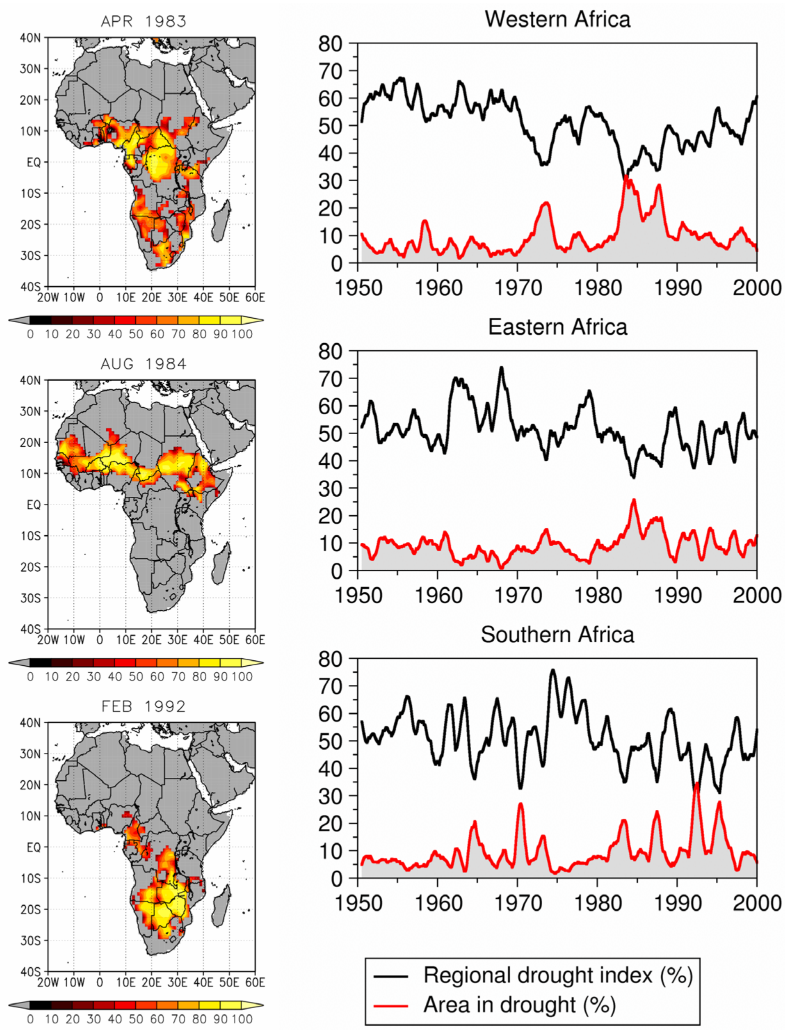

Fig. 7. Time series of ADM drought index and area in drought for three regions of Africa (right); left visuals show spatial distribution of drought severity (as percentiles of total column soil moisture relative to 1950-2000 climatology) for major 20th century drought events.

5. Summary

As shown in this study (including the results on our drought monitoring web site: http://hydrology.princeton.edu/forecast/ and http://hydrology.princeton.edu/monitor), as well as by Sheffield et al. [2004a] and Andreadis and Lettenmaier [2006], model-based drought monitoring systems provide a reasonably accurate and quantitative measure of land surface hydrological conditions, when forced with high quality meteorological data. This study also demonstrates the feasibility of doing drought prediction using seasonal forecasts from dynamic climate models. Although forecasts from dynamic climate models have limited skill over the mid-latitudes in precipitation and temperature predictions, the drought prediction for the recent U.S. drought and hindcasts over the Ohio River basin [Luo and Wood, 2008] indicate the possibility of boosting forecast skill by statistically bias correcting and downscaling climate model forecasts via the Bayesian merging procedure. For the 2007 US drought, DMAPS was able to predict the onset of the severe drought over the West with great confidence (small ensemble spread) several months in advance, and the spatial pattern and severity of the predicted drought correspond well to the subsequent realtime drought monitoring of actual (modeled) conditions. In the Southeast, the system also predicted dry conditions, but the location, area and severity of the drought are not as accurate and the confidence is lower, as indicated by the spread of the ensemble distribution. This suggests that the ensemble spread is also informative when interpreting ensemble predictions.

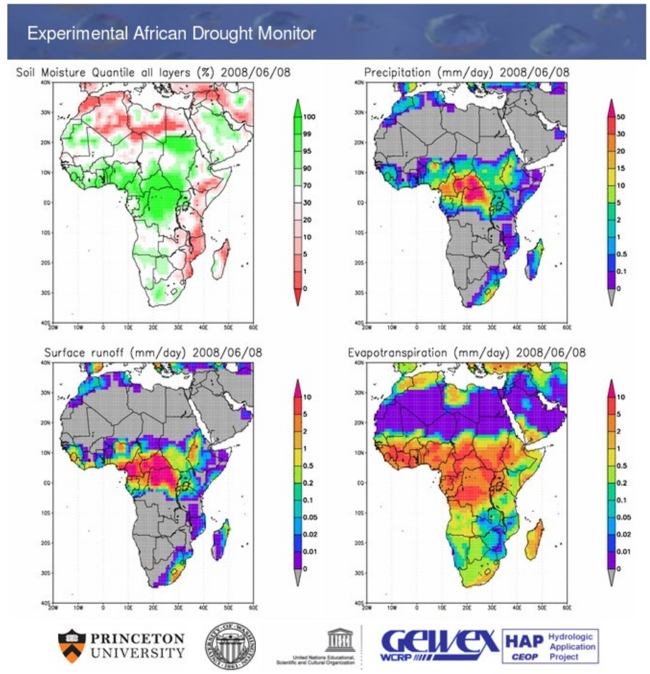

Fig. 8. Snapshot of the web interface to the drought monitor showing maps of current conditions (soil moisture percentiles relative to a 50-yr climatology) and other hydrologic fields such as daily precipitation, surface runoff and evapotranspiration.

Our current drought forecast system uses the ensemble seasonal forecast from CFS within the Bayesian merging procedure, but the system can potentially use forecasts from multiple models. As illustrated in this study and studies by Luo et al. [2007] and Luo and Wood [2008], a multi-model Bayesian merging produces more reliable and skillful forecasts as compared to forecasts from one single dynamic model. Our expected implementation of this procedure with seasonal forecasts from multiple seasonal climate models will further improve the accuracy of the drought recovery estimates and should help the development of the National Integrated Drought Information System (NIDIS).

Acknowledgments. This research was supported through NOAA's Climate Prediction Program for the Americas (CPPA) by Grant NA17RJ2612. This support is gratefully acknowledged.

References

American Meteorological Society (1997): Meteorological drought. *Bull. Am. Meteorol. Soc.*, **78,** 847-849.

Andreadis, K. M., and D. P. Lettenmaier (2006): Trends in 20th century drought over the continental United States. *Geophys. Res. Lett.,* **33**, L10403, doi:10.1029/2006GL025711.

Cherkauer, K. A., L. C. Bowling and D. P. Lettenmaier (2003): Variable Infiltration Capacity (VIC) cold land process model updates. *Global and Planetary Change*, **38(1-2)**, 151-159.

Cherkauer, K. A., and D. P. Lettenmaier (1999): Hydrologic effects of frozen soils in the upper Mississippi River basin. *J. Geophys. Res.*, **104**, 19, 599–19,610.

Cosgrove, Brian A. *et al.* (2003): Realtime and retrospective forcing in the North American Land Data Assimilation Systems (NLDAS) project. *J. Geophys. Res.,* **108** (D22), 8842, doi:10.1029/2002JD003118.

FEMA. (1995): National mitigation strategy; Partnerships for building safer communities. Mitigation Directorate, p. 2. Federal Emergency Management Agency, Washington, D.C.

Koster, R. D., M. J. Suarez and M. Heiser (2000): Variance and predictability of precipitation at seasonal-to-interannual timescales. *J. Hydrometeor*., **1**, 26-46.

Koster, R. D., M. J. Suarez, P. Liu, U. Jambor, A. Berg, M. Kistler, R. Reichle, M. Rodell and J. Famiglietti (2004): Realistic initialization of land surface states: impact on subseasonal forecast skill. *J. Hydrometeor.* **5**, 1049-1063. doi:10.1175/JHM-387.1.

Liang, X., E. F. Wood, and D. P. Lettenmaier (1996): Surface soil moisture parameterization of the VIC-2L model: Evaluation and modifications. *Global Planet. Change*, **13**, 195-206.

Luo, L., *et al.* (2003): Validation of the North American Land Data Assimilation System (NLDAS) retrospective forcing over the southern Great Plains. *J. Geophys. Res.*, **108**(D22), 8843, doi:10.1029/2002JD003246.

Luo, L., and E. F. Wood (2007): Monitoring and predicting the 2007 U.S. drought. *Geophys. Res. Lett.*, **34**, L22702, doi:10.1029/2007GL031673.

Luo, L., E. F. Wood, and M. Pan (2007): Bayesian merging of multiple climate model forecasts for seasonal hydrological predictions. *J. Geophys. Res.,* **112**, D10102, doi:10.1029/2006JD007655.

Luo L. and E. F. Wood (2008): Use of Bayesian mering techniques in a multimodel seasonal hydrologic ensemble prediction system for the Eastern United States. *J. Hydrometeorology*, **9**, 866-884.

Maurer, E.P., A.W. Wood, J.C. Adam, D.P. Lettenmaier, and B. Nijssen (2002): A long-term hydrologicly-based data set of land surface fluxes and states for the conterminous United States. *J. Climate.* **15**, 3237-3251.

Mitchell, Kenneth E. *et al.* (2004): The Multi-institution North American Land Data Assimilation System (NLDAS): Utilizing multiple GCIP products and partners in a continental distributed hydrological modeling system. *J. Geophys. Res.,* **109**, D07S90, doi: 10.1029/2003JD003823.

Nijssen, B., D. P. Lettenmaier, X. Liang, S. W. Wetzel, and E. F. Wood (1997): Streamflow simulation for continental-scale river basins. *Water Resour. Res*., **33**, 711-724.

Nijssen, B., R. Schnur, and D. P. Lettenmaier (2001): Global retrospective estimation of soil moisture using the Variable Infiltration Capacity land surface model, 1980-1993. *J. Climate,* **14**, 1790-1808.

Palmer, T. N. *et al.* (2004): Development of a European multimodel ensemble system for seasonal-to-interannual prediction (DEMETER). *Bull. Amer. Meteor. Soc*., **85**, 853-872.

Roads, J., *et al.* (2003): GCIP water and energy budget synthesis (WEBS). *J. Geophys. Res.*, **108**(D16), 8609, doi:10.1029/2002JD002583.

Robock, A., K. Y. Vinnikov, G. Srinivasan, J. K. Entin, S. E. Hollinger, N. A. Speranskaya, S. Liu, and A. Namkhai (2000): The Global Soil Moisture Data Bank. *Bull. Amer. Meteorol. Soc.*, **81**, 1281-1299.

Ross, T., and N. Lott (2003): A climatology of 1980–2003 extreme weather and climate events. Tech. Rep. 2003-01, NOAA/NESDIS, Natl. Clim. Data Cent., Asheville, N. C.

Saha, S., S. Nadiga, C. Thiaw, J. Wang, W. Wang, Q. Zhang, H. M. van den Dool, H.-L. Pan, S. Moorthi, D. Behringer, D. Stokes, M. Pena, S. Lord, G. White, W. Ebisuzaki, P. Peng, P. Xie (2006): The NCEP Climate Forecast System. *J. of Climate*, **19**, 3483-3517.

Sheffield, J., G. Goteti, F, Wen, E. F. Wood (2004a): A simulated soil moisture based drought analysis for the USA. *J. Geophys. Res.-Atmos*., **109** (D24): Art. No. D24108 Dec. 29 2004.

Sheffield, J., A. D. Ziegler, E. F. Wood, and Y. Chen, (2004b): Correction of the high-latitude rain day anomaly in the NCEP/NCAR reanalysis for land surface hydrological modeling. *J. Climate*, **17**, 3814-3828.

Sheffield, J., and E. F. Wood (2007): Characteristics of global and regional drought, 1950-2000: Analysis of soil moisture data from off-line simulation of the terrestrial hydrologic cycle. *J. Geophys. Res*., in press.

Svoboda, M., *et al.* (2002): The drought monitor. *Bull. Am. Meteorol. Soc*., **83**, 1181–1190.